

# Reconstruction of spatio-temporal signals of complex systems

C. Uhl, R. Friedrich, H. Haken

Institut für Theoretische Physik und Synergetik, Universität Stuttgart, Pfaffenwaldring 57/IV, D-70569 Stuttgart, Germany

Received: 11 February 1993 / Revised version: 27 April 1993

**Abstract.** We propose a novel method to analyze spatio-temporal signals emerging from synergetic systems. By this approach we are able to reconstruct the spatial modes, as well as their dynamic interaction close to instabilities. Our method is an extension of the principal component analysis to the case of nonlinear self-organizing systems. We demonstrate our method by an example of a codimension one instability, apply the algorithm to a simulated Bénard instability and present a generalization to bifurcations with several order parameters.

PACS: 02.60.+y; 47.25.Qv; 05.90+m

## 1. Introduction

Analyzing experimentally obtained spatio-temporal signals is an important tool in various fields of scientific research. The aim of such an analysis is to obtain a deeper insight into the cooperation of various components of a complex system. By such a phenomenological approach one hopes to draw conclusions from the experimentally accessible, macroscopic level to the microscopic level [1]. Fields of application include biological systems, like the analysis of EEG-data [2, 3, 4] and MEG-data [5], chemical reactions and fluid dynamics.

So far a great amount of work has been put into the study of the temporal evolution of a system, characterizing the dynamics by fractal dimensions and Lyapunov-exponents [6], as well as reconstructing the dynamics by introducing time-delay coordinates [7] or principal component analysis [8]. Yet the applicability, reliability and significance of these techniques is still under investigation [9–11].

Other examinations focus on the spatial features of a system by principal component analysis, obtaining the best convergent mode expansion with respect to the least-square error (compare Sect. 3.2). The temporal evolution of the system is entirely neglected however. It has been

stressed by one of us (H.H.) in [1], that the principal component analysis has to be extended when dealing with nonequilibrium systems.

Our approach in this paper is to simultaneously investigate temporal *and* spatial features of the signal by a least-square-fit method. In contrast to the work of L. Borland and one of us (H.H.) [12, 13], dealing with stochastic complex systems, we focus here on spatio-temporal signals emerging from deterministic complex systems near critical points of phase transitions. The spirit of the present approach is similar, however: In the vicinity of its instabilities the system can be treated by the theory of synergetics [14, 15], and order parameters and “enslaved” stable modes can be introduced. Therefore an analysis of the corresponding spatio-temporal signal has to focus on the identification of the order parameters and the enslaved modes, as well as a determination of the order parameter dynamics [16, 17]. In the following we shall show that this task can be accomplished by the formulation of a suitable extremum principle.

The paper is organized as follows: in Sect. 2 we briefly demonstrate how synergetics can be applied to the systems under consideration. Before presenting the more general approach in Sect. 5, we illustrate the method in Sect. 3 by a simple example, dealing with a codimension one instability, the pitchfork-bifurcation, and we apply the algorithm in Sect. 4 to a realistic situation concerning a problem of fluid-dynamics, the Bénard instability.

## 2. System considered

The starting-point of our analysis is a spatio-temporal signal  $\tilde{\mathbf{q}}(t)$ , where the vector-components of  $\tilde{\mathbf{q}}$  represent experimentally accessible quantities. As already mentioned, we will focus our attention on self-organizing complex systems, where a qualitative change of the macroscopic behavior occurs. In the vicinity of these phase-transitions the theory of synergetics applies [14, 15]. The state vector  $\tilde{\mathbf{q}}(t)$  of the system, which obeys a nonlinear

evolution equation of the form

$$\dot{\tilde{q}}(t) = N[\tilde{q}(t)], \quad (1)$$

turns out to be a superposition of unstable modes,  $\tilde{u}_i$ , and stable modes  $\tilde{s}_i$ :

$$\tilde{q}(t) = \sum_i \xi_{u_i}(t) \tilde{u}_i + \sum_i \xi_{s_i}(t) \tilde{s}_i. \quad (2)$$

This ansatz is exact and includes the case of spatial complexity, since any spatio-temporal signal can be represented by a sum over products of time-dependent amplitudes and spatial modes.

As a consequence of selforganization, i.e. in the vicinity of phase transition points, the amplitudes of the stable modes  $\xi_{s_i}(t)$  are enslaved by the “order parameters”  $\xi_{u_i}(t)$ , the amplitudes of the unstable modes: there exists a relationship of the form

$$\xi_{s_i}(t) = \xi_{s_i}[\xi_{u_i}(t)] \quad (3)$$

and the order parameters obey a closed set of evolution equations:

$$\dot{\xi}_{u_i}(t) = p_i[\xi_{u_i}(t)]. \quad (4)$$

It is the aim of our spatio-temporal analysis to find both the spatial modes  $\tilde{u}_i$ ,  $\tilde{s}_i$  as well as their mode-interaction, i.e. the dynamics of the amplitudes  $\xi_{u_i}(t)$ ,  $\xi_{s_i}(t)$ .

### 3. A simple example

#### 3.1. Simulated spatio-temporal signal

We assume a spatio-temporal signal  $\tilde{q}(t)$  of a system near a pitchfork-bifurcation with two occurring spatial modes, the stable mode  $\tilde{s}$  and the unstable mode  $\tilde{u}$ :

$$\tilde{q}(t) = \xi_u(t) \tilde{u} + \xi_s(t) \tilde{s}. \quad (5)$$

In this example we assume the following equation for the enslaved amplitudes:

$$\xi_s(t) = k \xi_u^2(t). \quad (6)$$

Since we shall study a system in the vicinity of a pitchfork-bifurcation, we deal with the following normal form, the order parameter equation,

$$\dot{\xi} = \varepsilon \xi + \gamma \xi^3, \quad (7)$$

omitting the subscript  $u$ .

We can introduce a potential  $W$ ,

$$W = -\frac{1}{2} \varepsilon \xi^2 - \frac{1}{4} \gamma \xi^4, \quad (8)$$

such that  $\dot{\xi} = -\frac{\partial W}{\partial \xi}$  holds, and therefore the order parameter equation represents an overdamped motion of a particle in the potential  $W$ . Figure 1 shows the potential  $W(\xi)$ , with the two balls describing both initial and end point of our example (chosen parameters of the normal

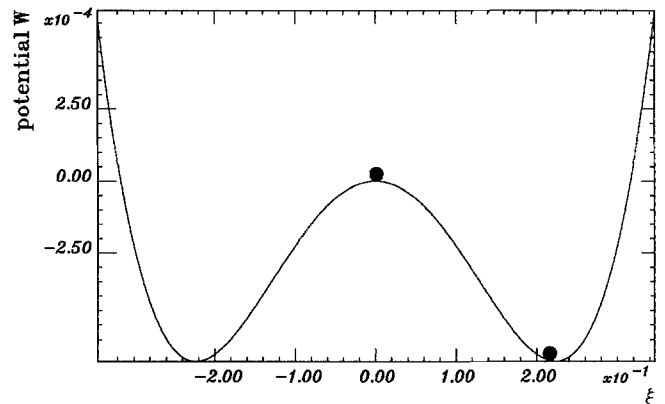


Fig. 1. Potential  $W$  depending on order parameter  $\xi$ . The two balls represent initial and end point of the overdamped motion describing the order parameter equation

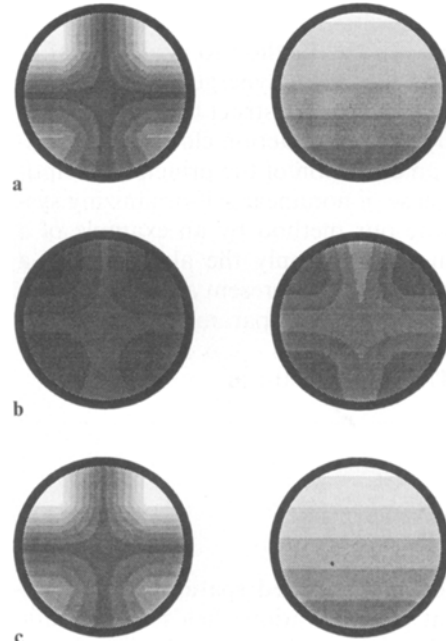


Fig. 2. a Simulated spatial modes  $\tilde{u}$  and  $\tilde{s}$ , b the resulting two vectors of PCA, and c modes, obtained by our introduced method

form:  $\varepsilon = 0.05$ ,  $\gamma = -1$ ;  $k = 1$ ; temporal resolution : 10 000 points).

In Fig. 2a we illustrate the chosen spatial modes  $\tilde{u}$  and  $\tilde{s}$ . The complete spatio-temporal signal  $\tilde{q}(t)$  is obtained from evaluating (5), (6) and (7).

The inverse problem, which we have to solve, is to extract from this signal the spatial modes  $\tilde{u}$ ,  $\tilde{s}$  and the constants  $k$ ,  $\varepsilon$ ,  $\gamma$ , describing the temporal evolution.

#### 3.2. Step 1. Projection into the relevant subspace

Since the signal  $\tilde{q}(t)$  consists of a (time-dependent) superposition of only two modes, the trajectory of  $\tilde{q}(t)$  is embedded in a two-dimensional phase space. It is useful to project the signal into this subspace, since it already contains the entire information of the system. One method

to obtain this relevant subspace is given by the principal component analysis (PCA, also known as Karhunen-Loëve decomposition and principal value decomposition). This method is based on a least-square-fit, seeking orthonormal modes  $\mathbf{w}_i$ , such that the error-function  $R_a$ ,

$$R_a = \left\langle \left( \tilde{\mathbf{q}}(t) - \sum_{i=1}^a (\tilde{\mathbf{q}}(t) \cdot \mathbf{w}_i) \mathbf{w}_i \right)^2 \right\rangle, \quad (9)$$

is minimal for every  $a \leq n$ . Thereby the notation  $\langle \rangle$  denotes the time-average. Variation of  $R_a$  with respect to  $\mathbf{w}_i$  yields an eigenvalue problem,

$$\tilde{\Gamma}_2 \mathbf{w}_i = \lambda_i \mathbf{w}_i, \quad (10)$$

with the correlation matrix  $\tilde{\Gamma}_2 = \langle \tilde{\mathbf{q}}(t) \otimes \tilde{\mathbf{q}}(t) \rangle$ .

The eigenvalues  $\lambda_i$  characterize the significance of the eigenvector  $\mathbf{w}_i$ , in such a way that the error function  $R_a$  becomes

$$R_a = \langle \tilde{\mathbf{q}} \cdot \tilde{\mathbf{q}} \rangle - \sum_{i=1}^a \lambda_i. \quad (11)$$

Applying this eigenvalue problem to our example yields two non-vanishing eigenvalues, which proves the occurrence of only two spatial modes and therefore the embedding of the trajectory  $\tilde{\mathbf{q}}(t)$  in a two-dimensional subspace. Figure 2b shows the two occurring eigenvectors  $\mathbf{w}_1$  and  $\mathbf{w}_2$  of PCA corresponding to these eigenvalues.

We now can project the signal  $\tilde{\mathbf{q}}(t)$  into the plane, spanned by the orthogonal and normalized eigenvectors of PCA  $\mathbf{w}_1$  and  $\mathbf{w}_2$  by the following projection:

$$\tilde{\mathbf{x}} \rightarrow \mathbf{x} = \begin{pmatrix} x_1 \\ x_2 \end{pmatrix}, \quad (12)$$

with

$$x_1 = \tilde{\mathbf{x}} \cdot \mathbf{w}_1, \quad x_2 = \tilde{\mathbf{x}} \cdot \mathbf{w}_2. \quad (13)$$

Therefore we now have to deal with a two-dimensional spatio-temporal signal,

$$\mathbf{q}(t) = \xi_u(t) \mathbf{u} + \xi_s(t) \mathbf{s}, \quad (14)$$

with enslaved amplitudes and order parameter equation given by (6) and (7).

### 3.3. Step 2. Specification of a least-square-fit potential $V$

After introducing a biorthogonal system with the adjoint modes  $\mathbf{u}^+$  and  $\mathbf{s}^+$ , fulfilling the relations

$$\begin{aligned} \mathbf{u}^+ \cdot \mathbf{u} &= 1, & \mathbf{s}^+ \cdot \mathbf{u} &= 0, \\ \mathbf{u}^+ \cdot \mathbf{s} &= 0, & \mathbf{s}^+ \cdot \mathbf{s} &= 1, \end{aligned} \quad (15)$$

the amplitudes  $\xi_u(t)$  and  $\xi_s(t)$  are given by

$$\xi_u(t) = \mathbf{u}^+ \cdot \mathbf{q}(t), \quad \xi_s(t) = \mathbf{s}^+ \cdot \mathbf{q}(t). \quad (16)$$

The adjoint modes have to be introduced since the modes  $\mathbf{u}$ ,  $\mathbf{s}$  need not be orthogonal.

A least-square-fit potential  $V$ , of which the global minimum represents both spatial modes (through (15)) as

well as the parameters of the temporal evolution of the system, is given by

$$\begin{aligned} V(\mathbf{s}^+, k, \varepsilon, \gamma, \mathbf{u}^+) &= \frac{\langle (\mathbf{q}\mathbf{s}^+ - k(\mathbf{q}\mathbf{u}^+)^2)^2 \rangle}{\langle (\mathbf{q}\mathbf{s}^+)^2 \rangle} \\ &\quad + \frac{\langle (\dot{\mathbf{q}}\mathbf{u}^+ - \varepsilon \mathbf{q}\mathbf{u}^+ - \gamma(\mathbf{q}\mathbf{u}^+)^3)^2 \rangle}{\langle (\dot{\mathbf{q}}\mathbf{u}^+)^2 \rangle}. \end{aligned} \quad (17)$$

Thereby both terms of the potential  $V(\mathbf{s}^+, k, \varepsilon, \gamma, \mathbf{u}^+)$  represent the relative variance for a certain set of parameters  $(\mathbf{s}^+, k, \varepsilon, \gamma, \mathbf{u}^+)$ .

The adjoint modes  $\mathbf{u}^+$  and  $\mathbf{s}^+$  cannot be determined uniquely yet, since the norm of the modes  $\mathbf{u}$  and  $\mathbf{s}$  can be scaled arbitrarily by factors  $c_u, c_s$ . (Whereas the corresponding amplitudes then are scaled by  $c_u^{-1}, c_s^{-1}$ , and the coefficients  $k, \gamma$  of (6), (7) by  $c_u^2/c_s, c_u^2$ .)

To avoid this, we have to require constraints to be fulfilled by the adjoint modes  $\mathbf{u}^+$ ,  $\mathbf{s}^+$ , which in this example are chosen to be

$$\langle (\mathbf{q}\mathbf{s}^+)^2 \rangle = \langle (\dot{\mathbf{q}}\mathbf{u}^+)^2 \rangle = 1, \quad (18)$$

which yields a quite simple potential  $V$ ,

$$\begin{aligned} V &= \langle (\mathbf{q}\mathbf{s}^+ - k(\mathbf{q}\mathbf{u}^+)^2)^2 \rangle + \lambda_s (\langle \mathbf{q}\mathbf{s}^+ \rangle^2 - 1) \\ &\quad + \langle (\dot{\mathbf{q}}\mathbf{u}^+ - \varepsilon \mathbf{q}\mathbf{u}^+ - \gamma(\mathbf{q}\mathbf{u}^+)^3)^2 \rangle \\ &\quad + \lambda_u (\langle (\dot{\mathbf{q}}\mathbf{u}^+)^2 \rangle - 1), \end{aligned} \quad (19)$$

with  $\lambda_s$  and  $\lambda_u$  representing Lagrange-parameters of the constraints of (18).

A local minimum of the potential  $V$  is given by the solutions of the non-linear system of equations,

$$\frac{\partial V}{\partial \mathbf{s}^+} = \frac{\partial V}{\partial k} = \frac{\partial V}{\partial \varepsilon} = \frac{\partial V}{\partial \gamma} = \frac{\partial V}{\partial \mathbf{u}^+} = 0, \quad (20)$$

whereby the values of the parameters  $\lambda_s, \lambda_u$  are obtained by evaluating the required constraints.

To obtain the minimum, one can solve the non-linear system by the method of gradient dynamics, i.e. finding the stationary solution of the following expressions:

$$\dot{\mathbf{s}}^+ = -\frac{\partial V}{\partial \mathbf{s}^+}, \quad (21)$$

$$\dot{k} = -\frac{\partial V}{\partial k}, \quad (22)$$

$$\dot{\varepsilon} = -\frac{\partial V}{\partial \varepsilon}, \quad (23)$$

$$\dot{\gamma} = -\frac{\partial V}{\partial \gamma}, \quad (24)$$

$$\dot{\mathbf{u}}^+ = -\frac{\partial V}{\partial \mathbf{u}^+}. \quad (25)$$

But, due to the specific form of the chosen least-square-fit potential  $V$ , the stationary solutions of (21–24) can be given analytically as a function of  $\mathbf{u}^+$  and the potential  $V(\mathbf{s}^+, k, \varepsilon, \gamma, \mathbf{u}^+)$  can be simplified to a low-dimensional

non-linear potential  $V(\mathbf{s}^+(\mathbf{u}^+), \varepsilon(\mathbf{u}^+), \gamma(\mathbf{u}^+), \mathbf{u}^+)$ , of which the minimum represents all wanted parameters. This reduction of free parameters will be presented in the next section.

Since we cannot solve (25) analytically and hence cannot eliminate the Lagrange-parameter  $\lambda_s$ , it is more convenient to deal with a potential of the form

$$\begin{aligned} V = & \langle (\mathbf{q}\mathbf{s}^+ - k(\mathbf{q}\mathbf{u}^+)^2)^2 \rangle + \lambda_s \langle (\mathbf{q}\mathbf{s}^+)^2 \rangle - 1 \\ & + \langle (\dot{\mathbf{q}}\mathbf{u}^+ - \varepsilon\mathbf{q}\mathbf{u}^+ - \gamma(\mathbf{q}\mathbf{u}^+)^3)^2 \rangle, \end{aligned} \quad (26)$$

with the adjoint mode  $\mathbf{u}^+$  fulfilling the constraint  $\langle (\dot{\mathbf{q}}\mathbf{u}^+)^2 \rangle = 1$ .

### 3.4. Step 3. Elimination of parameters

**3.4.1. Derivation of  $\mathbf{s}^+ = \mathbf{s}^+(\mathbf{u}^+)$ .** The local minimum of  $V(\mathbf{s}^+, k, \varepsilon, \gamma, \mathbf{u}^+)$  with respect to  $\mathbf{s}^+$  is given by

$$\langle (\mathbf{q}\mathbf{s}^+ - k(\mathbf{q}\mathbf{u}^+)^2) \mathbf{q} \rangle + \lambda_s \langle (\mathbf{q}\mathbf{s}^+) \mathbf{q} \rangle = 0, \quad (27)$$

which can be written, by making use of the summation of indices occurring twice, as

$$(1 + \lambda_s)(\Gamma_2)_{ij}s_j^+ = k(\Gamma_3)_{ijk}u_j^+u_k^+. \quad (28)$$

$\Gamma_2$  and  $\Gamma_3$  represent symmetric correlation tensors, which are defined by

$$(\Gamma_2)_{ij} = \langle q_i q_j \rangle, \quad (\Gamma_3)_{ijk} = \langle q_i q_j q_k \rangle. \quad (29)$$

Since  $\Gamma_2$  is invertible, i.e.  $\det \Gamma_2 \neq 0$ , because of the projection of  $\tilde{\mathbf{q}}(t)$  into the relevant subspace (cf. Sect. 3.2), we obtain

$$s_i^+ = \frac{k}{1 + \lambda_s} (\Gamma_2^{-1})_{ii} (\Gamma_3)_{ijk} u_j^+ u_k^+, \quad (30)$$

or, after defining e.g.,  $(\Gamma_3)_{ijk} u_j^+ u_k^+ = (\Gamma_3 : \mathbf{u}^+ : \mathbf{u}^+)_i = (\Gamma_3 (\mathbf{u}^+)^2)_i$ , in an index-free notation,

$$\mathbf{s}^+ = \frac{k}{1 + \lambda_s} \Gamma_2^{-1} \Gamma_3 (\mathbf{u}^+)^2. \quad (31)$$

The still unknown factor  $\frac{k}{1 + \lambda_s}$  can be calculated by evaluating the constraint  $\langle (\mathbf{q}\mathbf{s}^+)^2 \rangle = (\Gamma_2)_{ij}s_i^+s_j^+ = 1$ :

$$\begin{aligned} \frac{k}{1 + \lambda_s} \\ = & [(\Gamma_3)_{ijk} (\Gamma_2^{-1})_{kl} (\Gamma_3)_{lmn} u_i^+ u_j^+ u_m^+ u_n^+]^{-1/2}. \end{aligned} \quad (32)$$

In the index-free notation the adjoint mode is therefore given by

$$\mathbf{s}^+ = [\Gamma_3 \Gamma_2^{-1} \Gamma_3 (\mathbf{u}^+)^4]^{-1/2} \cdot \Gamma_2^{-1} \Gamma_3 (\mathbf{u}^+)^2. \quad (33)$$

**3.4.2. Derivation of  $k = k(\mathbf{u}^+)$ .** Since variation with respect to  $k$  yields

$$\langle (\mathbf{q}\mathbf{s}^+ - k(\mathbf{q}\mathbf{u}^+)^2) (\mathbf{q}\mathbf{u}^+)^2 \rangle = 0, \quad (34)$$

$k$  is given by

$$k = \frac{(\Gamma_3)_{ijk} s_i^+ u_j^+ u_k^+}{(\Gamma_4)_{ijkl} u_i^+ u_j^+ u_k^+ u_l^+}, \quad (35)$$

after introducing a correlation tensor  $\Gamma_4$ ,

$$(\Gamma_4)_{ijkl} = \langle q_i q_j q_k q_l \rangle. \quad (36)$$

Inserting (33) into (35),  $k$  can be written as

$$k = \frac{[(\Gamma_3)_{ijk} (\Gamma_2^{-1})_{kl} (\Gamma_3)_{lmn} u_i^+ u_j^+ u_m^+ u_n^+]^{1/2}}{(\Gamma_4)_{ijkl} u_i^+ u_j^+ u_k^+ u_l^+}, \quad (37)$$

or in the index-free notation,

$$k = \frac{[\Gamma_3 \Gamma_2^{-1} \Gamma_3 (\mathbf{u}^+)^4]^{1/2}}{\Gamma_4 (\mathbf{u}^+)^4}. \quad (38)$$

**3.4.3. Derivation of  $\varepsilon = \varepsilon(\mathbf{u}^+)$ ,  $\gamma = \gamma(\mathbf{u}^+)$ .** Variation with respect to  $\varepsilon$  and  $\gamma$  yields

$$\langle (\dot{\mathbf{q}}\mathbf{u}^+ - \varepsilon\mathbf{q}\mathbf{u}^+ - \gamma(\mathbf{q}\mathbf{u}^+)^3) \mathbf{q}\mathbf{u}^+ \rangle = 0 \quad (39)$$

$$\langle (\dot{\mathbf{q}}\mathbf{u}^+ - \varepsilon\mathbf{q}\mathbf{u}^+ - \gamma(\mathbf{q}\mathbf{u}^+)^3) (\mathbf{q}\mathbf{u}^+)^3 \rangle = 0. \quad (40)$$

Introducing correlation tensors  $\Lambda_2$ ,  $\Lambda_4$  and  $\Gamma_6$ ,

$$(\Lambda_2)_{ij} = \langle q_i \dot{q}_j \rangle, \quad (\Lambda_4)_{ijkl} = \langle q_i q_j q_k \dot{q}_l \rangle, \quad (41)$$

$$(\Gamma_6)_{ijklmn} = \langle q_i q_j q_k q_l q_m q_n \rangle,$$

the linear set of equations (39), (40) can be written as

$$\begin{pmatrix} (\Gamma_2)_{ij} u_i^+ u_j^+ & (\Gamma_4)_{ijkl} u_i^+ u_j^+ u_k^+ u_l^+ \\ (\Gamma_4)_{ijkl} u_i^+ u_j^+ u_k^+ u_l^+ & (\Gamma_6)_{ijklmn} u_i^+ u_j^+ u_k^+ u_l^+ u_m^+ u_n^+ \end{pmatrix} \times \begin{pmatrix} \varepsilon \\ \gamma \end{pmatrix} = \begin{pmatrix} (\Lambda_2)_{ij} u_i^+ u_j^+ \\ (\Lambda_4)_{ijkl} u_i^+ u_j^+ u_k^+ u_l^+ \end{pmatrix}, \quad (42)$$

or in an index-free notation,

$$\underbrace{\begin{pmatrix} \Gamma_2 (\mathbf{u}^+)^2 & \Gamma_4 (\mathbf{u}^+)^4 \\ \Gamma_4 (\mathbf{u}^+)^4 & \Gamma_6 (\mathbf{u}^+)^6 \end{pmatrix}}_A \begin{pmatrix} \varepsilon \\ \gamma \end{pmatrix} = \begin{pmatrix} \Lambda_2 (\mathbf{u}^+)^2 \\ \Lambda_4 (\mathbf{u}^+)^4 \end{pmatrix}. \quad (43)$$

The determinant of the occurring matrix  $A$  is given by

$$\det A = \Gamma_6 (\mathbf{u}^+)^6 \Gamma_2 (\mathbf{u}^+)^2 - (\Gamma_4 (\mathbf{u}^+)^4)^2$$

$$= \langle \xi_u^6 \rangle \langle \xi_u^2 \rangle - \langle \xi_u^4 \rangle^2, \quad (44)$$

which in general does not vanish for non-stationary signals. The matrix  $A$  is therefore invertible and we obtain

$$\begin{pmatrix} \varepsilon \\ \gamma \end{pmatrix} = \frac{1}{\det A} \begin{pmatrix} \Gamma_6 (\mathbf{u}^+)^6 & -\Gamma_4 (\mathbf{u}^+)^4 \\ -\Gamma_4 (\mathbf{u}^+)^4 & \Gamma_2 (\mathbf{u}^+)^2 \end{pmatrix} \times \begin{pmatrix} \Lambda_2 (\mathbf{u}^+)^2 \\ \Lambda_4 (\mathbf{u}^+)^4 \end{pmatrix}. \quad (45)$$

**3.4.4. One-dimensional potential.** Equations (33), (38) and (45) represent stationary solutions of the differential (21–24). Inserting these equations in the potential

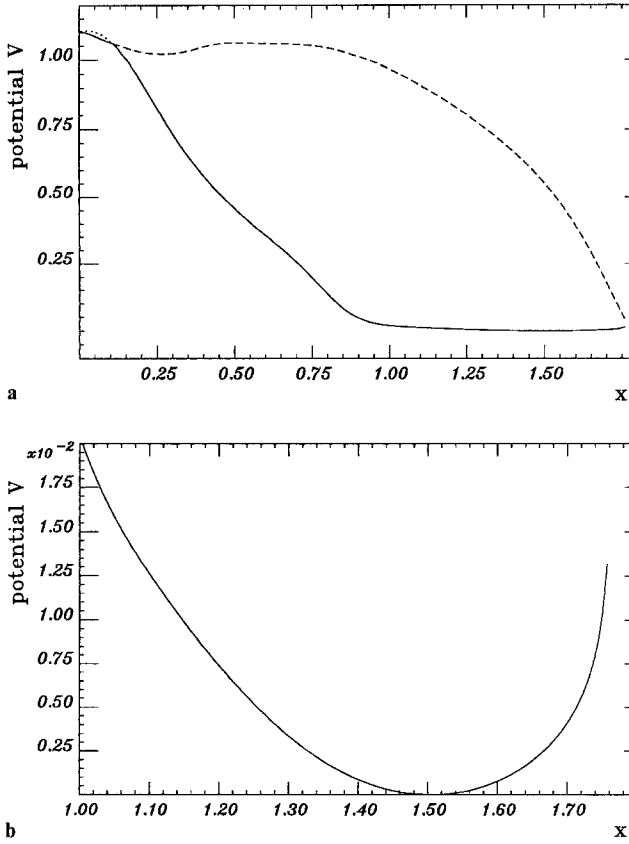


**Fig. 3.** **a** Least-square-fit potential  $V$  (solid line),  $V_-$  (dotted line) and  $V_+$  (dashed line), depending on the first component  $x$  of the adjoint vector  $\mathbf{u}^+$ . **b** Enlargement of **a** in the vicinity of the minimum

$V(\mathbf{s}^+, k, \varepsilon, \gamma, \mathbf{u}^+)$  (17) results in a potential  $V(\mathbf{u}^+) = V(\mathbf{s}^+(\mathbf{u}^+), k(\mathbf{u}^+), \varepsilon(\mathbf{u}^+), \gamma(\mathbf{u}^+), \mathbf{u}^+)$ :

$$V(\mathbf{u}^+) = 2 - \frac{\Gamma_3 \Gamma_2^{-1} \Gamma'_3}{\Gamma'_4} + \frac{\Gamma'_6 \Lambda'_2{}^2 - 2 \Gamma'_4 \Lambda'_4 \Lambda'_2 + \Gamma'_2 \Lambda'_4{}^2}{\Gamma'_4 - \Gamma'_6 \Gamma'_2}. \quad (46)$$

We thereby introduced abbreviations, like  $\Gamma'_4 := \langle (\mathbf{u}^+)^4 \rangle = \langle (\mathbf{q}\mathbf{u}^+)^4 \rangle$ .

Since  $\mathbf{u}^+$  has to fulfil the constraint  $\langle (\dot{\mathbf{q}}\mathbf{u}^+)^2 \rangle = 1$ , we can express the second component of the two-dimensional vector  $\mathbf{u}^+$  as a function of the first one:

$$\begin{aligned} \mathbf{u}^+ &= \begin{pmatrix} x \\ y_{\pm} \end{pmatrix}, \\ y_{\pm} &= \frac{1}{\langle \dot{q}_2^2 \rangle} (-\langle \dot{q}_1 \dot{q}_2 \rangle x \pm [\langle \dot{q}_1 \dot{q}_2 \rangle^2 \\ &\quad - \langle \dot{q}_1^2 \rangle \langle \dot{q}_2^2 \rangle] x^2 + \langle \dot{q}_2^2 \rangle]^{1/2}). \end{aligned} \quad (47)$$

Inserting this in the least-square-fit potential  $V(\mathbf{u}^+)$ , we obtain two one-dimensional potentials  $V_{\pm}(x)$ , which are shown in Fig. 3a. The dashed and the dotted line represent  $V_+(x)$  and  $V_-(x)$ , whereas the solid line shows the potential  $V(x)$ , which represents the minimum of

$(V_+(x), V_-(x))$  for every possible  $x$  value. In Fig. 3b we present an enlargement of Fig. 3a in the vicinity of the occurring minimum. For our spatio-temporal signal there is a minimum at  $x_0 \approx 1.5$  with a corresponding value for the potential  $V(x_0) = 0$ , which shows that the global minimum represents the right choice of parameters  $(\mathbf{s}^+, k, \varepsilon, \gamma, \mathbf{u}^+)$ .

### 3.5. Step 4. Global minimum of $V(x)$

In this example the global minimum at  $x = x_0$  can be easily found, just by plotting the one-dimensional potential  $V(x)$  (cf. Fig. 3).

Figure 2c shows the modes  $\tilde{\mathbf{u}}$  and  $\tilde{\mathbf{s}}$ , calculated by using (47), (33), (15), (12) for  $x = x_0$ . By comparing Fig. 2c with Fig. 2a, one can see that we obtained the exact modes of which the initial spatio-temporal signal  $\tilde{\mathbf{q}}(t)$  is composed. The parameters responsible for the dynamic evolution of the system, i.e. the parameters  $k, \varepsilon$  and  $\gamma$  of the order parameter equation, are as well calculated from  $x_0$  (by (47), (45), (38)), and they show again perfect agreement with the original parameters.

Figure 4 shows the resulting amplitudes (through (47), (31), (16)) corresponding to the numerically calculated spatial modes  $\tilde{\mathbf{u}}$  and  $\tilde{\mathbf{s}}$  (solid lines) in comparison to the amplitudes of the PCA modes (dashed lines). The original amplitudes of (5) are symbolized by small boxes, which demonstrates as well perfect correspondence to the amplitudes obtained by our method.

Summarizing this example, we have shown that we obtain “better” results with our novel method in comparison to the PCA expansion, “better” in the sense of obtaining modes, for which the dynamic interaction is completely understood. This dynamics corresponds to the mode interaction occurring in the vicinity of the instability point. This depends on the fact that our method aims at a determination of the quantities such as order

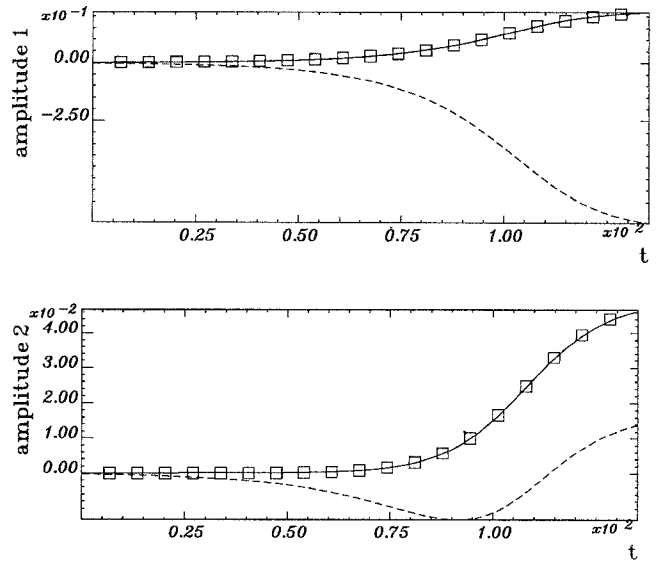


**Fig. 4.** Amplitudes of obtained vectors versus time  $t$ . The dashed line represents the method of PCA, the solid one our novel method. The boxes describe the original amplitudes

parameters and enslaved modes, i.e. quantities underlying the process of pattern formation.

In the next section we will apply the method just presented to a realistic situation of fluid-dynamics.

#### 4. Bénard instability

This well-known problem of fluid-dynamics consists of an infinitely extended horizontal fluid layer which is heated from below so that a temperature gradient is maintained. Depending on this gradient, which can be expressed by the Rayleigh number  $R$ , the fluid remains either quiescent and heat is transported by conduction (for a Rayleigh number  $R$  smaller than a critical value  $R_c$ ,  $R < R_c$ ) or the fluid starts to convect forming regular rolls ( $R > R_c$ ).

We have simulated these processes by a numerical integration of the two-dimensional Navier-Stokes-equation with periodic boundary conditions for different values of the Rayleigh number  $R = R_c \cdot (1 + \varepsilon)$ .

Figure 5 shows for three different values of  $\varepsilon$  the time series of the temperature field of a vertical intersection

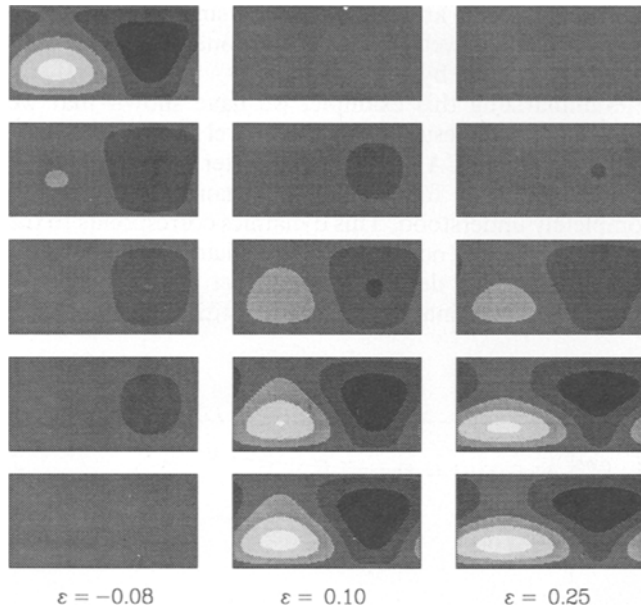


**Fig. 5.** Time-series of the temperature field for different values of  $\varepsilon$  (initial condition corresponds to the top)

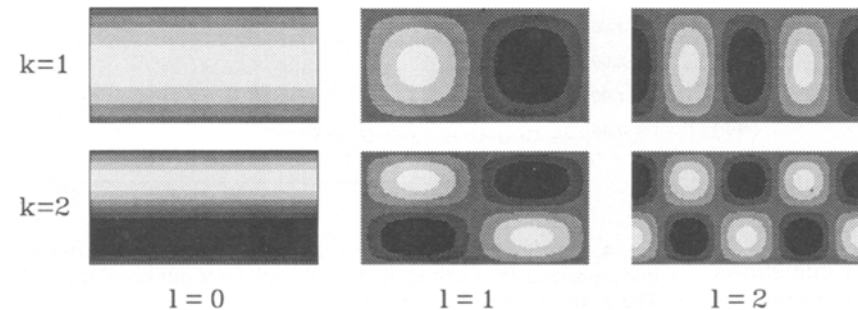


**Fig. 6.** Spatial modes of the form  $\sin(k\pi z) \cdot \exp(ilk_c x)$ , in which the temperature field can be decomposed

perpendicular to the occurring rolls. In the subcritical case ( $\varepsilon < 0$ ) we have chosen a roll as a initial condition, which is then dying out in the evolution of time. Whereas in the supercritical case ( $\varepsilon > 0$ ) a homogeneous state as initial condition is developing to the described rolls as convection patterns.

By theoretical analysis of the system it can be shown that in the vicinity of the instability point, i.e.  $R \approx R_c$ , the system can be described by one order parameter and several enslaved modes, of which two contribute most to the signal. The corresponding mode of the order parameter is given by

$$u(x, z) = \sin(\pi z) \cdot e^{ik_c x}, \quad (48)$$

which is shown in Fig. 6 ( $k = 1, l = 1$ ). The most dominant enslaved modes are given by

$$s_1(x, z) = \sin(2\pi z), \quad (49)$$

$$s_2(x, z) = \sin(2\pi z) \cdot e^{i2k_c x}, \quad (50)$$

which are presented in Fig. 6 by  $k = 2, l = 0$  and  $k = 2, l = 2$ . In the vicinity of the instability the dynamics of the order parameter obey a pitchfork-type of bifurcation and the amplitudes of the two dominant enslaved modes are given by  $\xi_s = k \xi_u^2$ . We therefore can treat the obtained spatio-temporal signals with the method presented in Sect. 3.

Figure 7 shows (for the three different  $\varepsilon$  values) the first two PCA modes and the normalized modes  $u$  and  $s$  obtained by our algorithm. In the first two cases ( $\varepsilon = -0.08$  and  $\varepsilon = 0.1$ ) the obtained modes  $u$  and  $s$  correspond quite well to the expected ones, in particular the difference to the PCA modes is obvious. For  $\varepsilon = 0.25$  the reconstruction of  $u$  still yields “better” results than the PCA modes but does correspond to the exact order parameter of the system. This is due to higher nonlinearities in the order parameter equation, which for higher  $\varepsilon$  values gain more and more influence and which are neglected in our ansatz of the least-square-fit potential  $V$  (26). Another reason for this occurring discrepancy lies in the projection of the spatio-temporal signal into the subspace spanned by the first two PCA modes. Since for higher values of  $\varepsilon$  more enslaved modes contribute to the spatio-temporal signal, the assumption of a two-dimensional subspace embedding the signal gradually loses validity, which also can be seen from the increasing number of non-neglectable eigenvalues of the PCA-expansion.

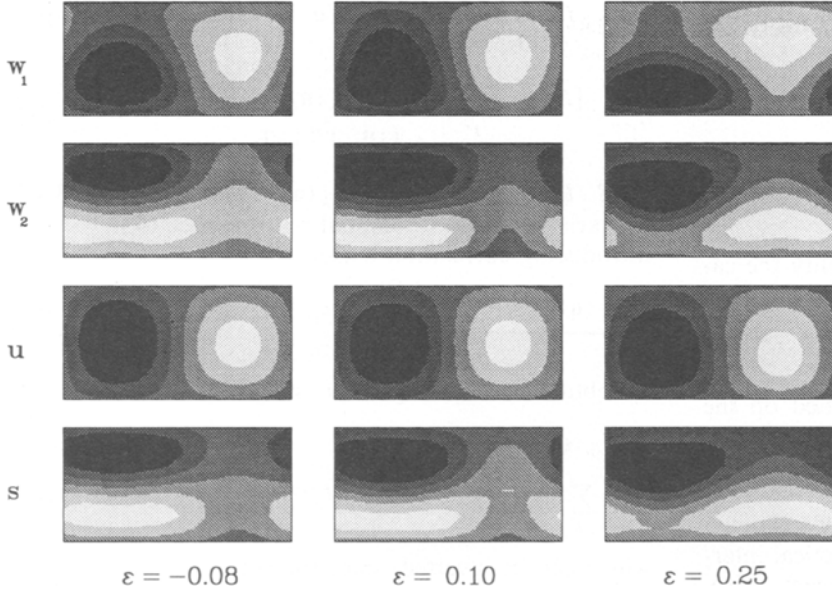


**Fig. 7.** PCA modes  $w_1$ ,  $w_2$  and modes  $u$ ,  $s$  obtained by our algorithm for different values of  $\epsilon$

After this second example we will generalize our least-square-fit method to more complex spatio-temporal signals.

## 5. Generalization

### 5.1. Spatio-temporal signal $\tilde{\mathbf{q}}(t)$

We now assume a spatio-temporal signal  $\tilde{\mathbf{q}}(t)$ , which obeys the superposition of unstable modes  $\tilde{\mathbf{u}}_i$  and stable modes  $\tilde{\mathbf{s}}_i$ , as given by (2), with corresponding enslaved amplitudes (3) and order parameter (4). Our task remains the same, namely the identification of order parameters, enslaved modes and a determination of the underlying dynamics.

### 5.2. Step 1. Relevant subspace

If the vector  $\tilde{\mathbf{q}}$  consists of  $n$  components,  $\tilde{\mathbf{q}}(t)$  represents a trajectory in an  $n$ -dimensional space  $\mathbf{R}^n$ . But there exists a subspace  $\mathbf{R}^m \subseteq \mathbf{R}^n$ , which is spanned by the modes  $\tilde{\mathbf{u}}_i$  and  $\tilde{\mathbf{s}}_i$ , in which the trajectory of  $\tilde{\mathbf{q}}(t)$  is embedded. To find this relevant subspace, i.e. to determine the number of occurring spatial modes, one can use PCA, as already shown for the example.

For a completely deterministic system the relevant subspace is spanned by the eigenvectors  $\mathbf{w}_i$  with non-vanishing eigenvalues  $\lambda_i$ .

Applying the projection to the spatio-temporal signal  $\tilde{\mathbf{q}}(t)$ , in analogy to the example, we obtain

$$\mathbf{q}(t) = \sum_i \xi_{u_i}(t) \mathbf{u}_i + \sum_i \xi_{s_i}(t) \mathbf{s}_i, \quad (51)$$

with the vector-components belonging now to the basis vectors  $\mathbf{w}_i$ , the eigenvectors of PCA.

### 5.3. Step 2. Least-square-fit potential $V$

We will derive the nonlinear potential, assuming the occurrence of two order parameters  $\mathbf{u}_1$  and  $\mathbf{u}_2$ . We restrict ourselves to two order parameters for the clearness of presentation. A generalization to more than two order parameters can be easily carried out.

Assuming a polynomial form of the enslaved amplitudes,

$$\xi_{s_i} = \sum_{j+k=2}^{m_i} b_{ijk} (\xi_{u_1})^j (\xi_{u_2})^k (j, k \geq 0), \quad (52)$$

we can write the signal  $\mathbf{q}(t)$  as a power series of the occurring order parameters  $\xi_{u_1}$  and  $\xi_{u_2}$ :

$$\mathbf{q}(t) = \sum_i \xi_{u_i} \mathbf{u}_i + \sum_{j+k=2}^m \xi_{u_1}^j \xi_{u_2}^k \cdot \left( \sum_i b_{ijk} \mathbf{s}_i \right). \quad (53)$$

We now can introduce a new set of modes  $\mathbf{v}_{jk}$ ,

$$\mathbf{v}_{jk} = \sum_i b_{ijk} \mathbf{s}_i, \quad (54)$$

which represent “combined stable modes” belonging to the amplitude  $\xi_{u_1}^j \xi_{u_2}^k$ .

We assume a polynomial form of the nonlinearities of the order parameter equations of the form

$$\dot{\xi}_{u_1} = a_{110} \xi_{u_1} + a_{101} \xi_{u_2} + \sum_{j+k=2}^{n_1} a_{1jk} (\xi_{u_1})^j (\xi_{u_2})^k, \quad (55)$$

$$\begin{aligned} \dot{\xi}_{u_2} = a_{201} \xi_{u_2} + a_{210} \xi_{u_1} \\ + \sum_{j+k=2}^{n_2} a_{2jk} (\xi_{u_1})^j (\xi_{u_2})^k (j, k \geq 0). \end{aligned} \quad (56)$$

We are free to fix the coefficients  $a_{110}$ ,  $a_{101}$ ,  $a_{210}$ ,  $a_{201}$  of the linear terms in the following way depending on the nature of the instability. In the case that the linear matrix

has two real eigenvalues we can assume the linear matrix to be diagonal:

$$a_{101} = a_{210} = 0. \quad (57)$$

For a Hopf bifurcation we can choose

$$a_{110} = a_{201}, \quad a_{101} = -a_{210}, \quad (58)$$

and in the case of a codimension two instability the canonical choice leads to

$$a_{110} = 0, \quad a_{101} = 1. \quad (59)$$

This choice of the linear terms can be justified on the basis of a linear transformation of the modes  $\mathbf{u}_1, \mathbf{u}_2$ . We point out that in certain cases it is possible to use symmetry arguments to restrict the structure of the order parameter equation by reducing the number of unknown coefficients of the nonlinearity. This is of practical interest for the treatment of the variational problem. Also, one might think of applying the usual normal form procedure to our algorithm.

After introducing a biorthogonal system with adjoint vectors  $\mathbf{v}_{ij}^+, \mathbf{v}_{ij}^-$ , we define, in analogy to the previous example, the following least-square-fit potential  $V$ ,

$$\begin{aligned} V(\mathbf{v}_{ij}^+, k_{ij}, a_{ijk}, \mathbf{u}_i^+) \\ = \sum_{i,j} \langle (\mathbf{q}\mathbf{v}_{ij}^+ - k_{ij}(\mathbf{q}\mathbf{u}_1^+)^i(\mathbf{q}\mathbf{u}_2^+)^j)^2 \rangle \\ + (\lambda_{ij} \langle (\mathbf{q}\mathbf{v}_{ij}^+)^2 \rangle - 1) \\ + \sum_i \left\langle \left( \mathbf{q}\mathbf{u}_i^+ - \sum_{j,k} a_{ijk}(\mathbf{q}\mathbf{u}_1^+)^j(\mathbf{q}\mathbf{u}_2^+)^k \right)^2 \right\rangle, \end{aligned} \quad (60)$$

with the sums

$$\sum_{i,j} = \sum_{i+j=2}^m, \quad \sum_{j,k} = \sum_{j+k=1}^{n_i}, \quad (61)$$

and the constraints,

$$\langle (\mathbf{q}\mathbf{v}_{ij}^+)^2 \rangle = \langle (\mathbf{q}\mathbf{u}_i^+)^2 \rangle = 1. \quad (62)$$

The right choice of  $\mathbf{u}_i^+, \mathbf{v}_{ij}^+, k_{ij}, a_{ijk}$  is given by the minimum of the potential  $V$  with respect to these quantities, which again could be found by gradient dynamics. Yet, analogous to the previous example, we can eliminate parameters by deriving functions  $\mathbf{v}_{ij}^+ = \mathbf{v}_{ij}^+(\mathbf{u}_k^+)$ ,  $k_{ij} = k_{ij}(\mathbf{u}_k^+)$  and  $a_{ijk} = a_{ijk}(\mathbf{u}_l^+)$  at the minimum of the potential. This will be outlined in the next section.

#### 5.4. Step 3. Elimination of parameters

**5.4.1. Derivation of  $\mathbf{v}_{ij}^+ = \mathbf{v}_{ij}^+(\mathbf{u}_k^+)$ .** Variation of the potential  $V$  (60) with respect to  $\mathbf{v}_{mn}^+$ , eliminating the Lagrange-parameter  $\lambda_{mn}$ , and carrying out calculations analogous to those in Sect. 3.4.1, yields

$$\begin{aligned} \mathbf{v}_{mn}^+ &= [\Gamma_{m+n+1} \Gamma_2^{-1} \Gamma_{m+n+1} (:u_1^+)^{2m} (:u_2^+)^{2n}]^{-1/2} \\ &\cdot \Gamma_2^{-1} \Gamma_{m+n+1} (:u_1^+)^m (:u_2^+)^n. \end{aligned} \quad (63)$$

**5.4.2. Derivation of  $k_{ij} = k_{ij}(\mathbf{u}_k^+)$ .** Variations with respect to  $k_{mn}$  yields,

$$k_{mn} = \frac{[\Gamma_{m+n+1} \Gamma_2^{-1} \Gamma_{m+n+1} (:u_1^+)^{2m} (:u_2^+)^{2n}]^{1/2}}{\Gamma_{2m+2n} (:u_1^+)^{2m} (:u_2^+)^{2n}}. \quad (64)$$

**5.4.3. Derivation of  $a_{ijk} = a_{ijk}(\mathbf{u}_j^+)$ .** Similar to Sect. 3.4.3, by variation of the potential with respect to  $a_{lmn}$ , after introducing correlation-tensors  $A_i$ ,

$$A_i = \underbrace{\langle \mathbf{q} \otimes \mathbf{q} \otimes \cdots \otimes \mathbf{q} \otimes \dot{\mathbf{q}} \rangle}_i, \quad (65)$$

we obtain an inhomogeneous set of equations

$$\begin{aligned} A_{m+n} : \mathbf{u}_l^+ &(:u_1^+)^m (:u_2^+)^n \\ &= \sum_{j,k} a_{ijk} \Gamma_{j+k+m+n} (:u_1^+)^{j+m} (:u_2^+)^{k+n}, \end{aligned} \quad (66)$$

which can be inverted, since the corresponding determinant does not vanish (cf. Sect. 3.4.3):

$$a_{ijk} = a_{ijk} [\mathbf{u}_1^+, \mathbf{u}_2^+]. \quad (67)$$

**5.4.4. Resulting potential.** Inserting (63), (64) and (67) into the potential  $V$  (60) results in a nonlinear low-dimensional potential  $V(\mathbf{u}_1^+, \mathbf{u}_2^+)$ ,

$$\begin{aligned} V(\mathbf{u}_1^+, \mathbf{u}_2^+) \\ = \sum_{i,j} \left( \langle (\mathbf{q}\mathbf{v}_{ij}^+ [\mathbf{u}_1^+, \mathbf{u}_2^+]) \right. \\ \left. - k_{ij} [\mathbf{u}_1^+, \mathbf{u}_2^+] (\mathbf{q}\mathbf{u}_1^+)^i (\mathbf{q}\mathbf{u}_2^+)^j \rangle \right) \\ + \sum_i \left\langle \left( \mathbf{q}\mathbf{u}_i^+ - \sum_{j,k} a_{ijk} [\mathbf{u}_1^+, \mathbf{u}_2^+] (\mathbf{q}\mathbf{u}_1^+)^j (\mathbf{q}\mathbf{u}_2^+)^k \right)^2 \right\rangle. \end{aligned} \quad (68)$$

#### 5.5. Step 4. Global minimum of $V(\mathbf{u}_1^+, \mathbf{u}_2^+)$

In analogy to the example of Sect. 3, we still have to fulfil the constraints concerning the adjoint modes  $\mathbf{u}_1^+, \mathbf{u}_2^+$ , and we thereby eliminate two further degrees of freedom.

The final remaining task is now to search for the global minimum of the low-dimensional nonlinear potential, which represents the adjoint modes  $\mathbf{u}_1^+$  and  $\mathbf{u}_2^+$  and hence gives us, through (63), (64) and (67), all wanted parameters.

In the case that additional local minima arise, more sophisticated methods, like simulated annealing or Monte Carlo methods (see e.g. [18]), have to be considered to find the global minimum of the potential.

## 6. Summary and outlook

We have derived a method which allows for an identification of order parameters and enslaved modes as well as a determination of the order parameter dynamics for non-equilibrium systems close to instabilities.

Our method especially applies to systems governed by deterministic dynamics. We expect that it is well suited for instabilities leading to chaotic temporal behavior due to mode interaction. The advantage of our method compared with the well-known principal component analysis is the fact that the spatial modes and the temporal dynamics of the reconstruction of the spatio-temporal signal are determined simultaneously from an extremum principle.

We would like to mention that the robustness of our method concerning noise and finite precision of measurements is due to the application of a least-square-fit potential. Indeed this is used to reduce the effect of additive noise by averaging over time. In addition the potential function can also be derived from a path integral formulation, in which noise is taken into account [19]. By this approach it can be derived that the form of the potential function does not depend on noise strengths, at least as only additive noise is present.

In our future work we plan to apply this algorithm to instabilities of codimension two and three on simulated, as well as experimentally obtained, spatio-temporal signals.

We would like to thank D. Reimann for helpful discussions.

## References

1. Haken, H.: *Information and selforganization*. Berlin, Heidelberg, New York: Springer 1988
2. Friedrich, R., Fuchs, A., Haken, H.: Spatio-temporal EEG patterns. In: *Synergetics of rhythms in biological systems*. Haken, H., Köpchen, H.P. (eds.). Berlin, Heidelberg, New York: Springer 1992
3. Friedrich, R., Uhl, C.: Synergetic analysis of human electroencephalograms: Petit-mal epilepsy. In: *Evolution of dynamical structures in complex systems*. Friedrich, R., Wunderlin, A. (eds.). Berlin, Heidelberg, New York: Springer 1992
4. Gallez, D., Babloyantz, A.: *Biol. Cybern.* **64**, 381 (1991)
5. Kelso, J.A.S.: Coordination dynamics of human brain and behavior. In: *Evolution of dynamical structures in complex systems*. Friedrich, R., Wunderlin, A. (eds.). Berlin, Heidelberg, New York: Springer 1992
6. Grassberger, P., Procaccia, I.: *Physica* **D9**, 189 (1983)
7. Takens, F.: Detecting strange attractors in fluid turbulence. In: *Dynamical systems and turbulence*. Lecture Notes in Mathematics. Vol. 898. Rand, D., Young, L.S. (eds.). Berlin, Heidelberg, New York: Springer 1981
8. Broomhead, D.S., King, G.P.: *Physica* **D20**, 217 (1987)
9. Layne, S.P., Mayer-Kress, G., Holzfuss, J.: Problems associated with dimensional analysis of electroencephalogram data. In: *Dimensions and entropies in chaotic systems*. Springer Series in Synergetics, Vol. 32. Mayer-Kress, G. (ed.). Berlin, Heidelberg, New York: Springer 1986
10. Paluš, M., Dvořák, I.: *Physica* **D55**, 221 (1992)
11. Eckmann, J.P., Ruelle, D.: *Physica* **D56**, 185 (1992)
12. Borland, L., Haken, H.: *Z. Phys.* **B88**, 95 (1992)
13. Borland, L., Haken, H.: *Ann. Phys.* **1**, 452 (1992)
14. Haken, H.: *Synergetics. An Introduction*. Springer Series in Synergetics. Vol. 1. Berlin, Heidelberg, New York: Springer 1983
15. Haken, H.: *Advanced synergetics*. Springer Series in Synergetics. Berlin, Heidelberg, New York: Springer 1987
16. Haken, H.: *Z. Phys.* **B61**, 329 (1985)
17. Haken, H.: *Z. Phys.* **B62**, 255 (1986)
18. Szu, H., Hartley, R.: *Phys. Lett.* **A122**, 157 (1987)
19. Friedrich, R., Uhl, C., Haken, H.: (in preparation)

## Analysis of spatiotemporal signals of complex systems

C. Uhl, R. Friedrich, and H. Haken

*Institut für Theoretische Physik und Synergetik, Universität Stuttgart, Pfaffenwaldring 57/IV, 70550 Stuttgart, Germany*

(Received 27 June 1994; revised manuscript received 27 December 1994)

We present a method of analyzing spatiotemporal signals emerging from nonequilibrium self-organizing systems that are close to instability. The algorithm aims at an identification of spatial modes and corresponding order-parameter equations. We discuss and demonstrate the method by examples of simulated codimension I and II instabilities, including a numerically integrated partial differential equation leading to "blinking states."

PACS number(s): 05.90.+m, 02.60.-x

### I. INTRODUCTION

In various fields of science the analysis of spatiotemporal patterns emerging from complex systems is an important element of research. The aim is to obtain a microscopic description of the system in terms of spatial patterns and their dynamics. Fields of application can vary from hydrodynamics (e.g., [1]), chemical reactions, and meteorology (e.g., [2]) to biological systems, such as the analysis of EEG [3,4] and MEG data [5,6]. One hopes to draw conclusions from the experimentally obtained macroscopic patterns to the microscopic level and to obtain a deeper insight into the cooperation of various components of a nonequilibrium system [7].

Up to now there seem to exist three different ways for analyzing spatiotemporal signals. The first one, which has been extensively studied in the past, focuses on the temporal evolution of the signal. Here, the dynamics is characterized in terms of metric properties of the underlying attractors like Lyapunov exponents and fractal dimensions [8]. On the other hand, great efforts have been made in reconstructing the dynamics by introducing time-delay coordinates [9] or principal component analysis (with respect to the temporal evolution) [10]. Furthermore, attempts have been made to fit sets of ordinary differential equations to the experimentally obtained time series [11,12]. Yet there are still open questions concerning the applicability, reliability, and significance of these techniques [13–15].

A second approach concentrates on the spatial features of a signal, with the aim of finding a mode expansion converging best with respect to the least-square deviation, by applying principal component analysis (compare Sec. III B and e.g., [1,16]). In case where the evolution equation of the system under consideration is known, as e.g., for hydrodynamic problems, it is possible to obtain finite dimensional Galerkin approximations to the dynamics by projecting the evolution equations onto the modes obtained by the principal component analysis.

A third approach has been discussed by us in a previous paper [17]. Here, we restrict our attention to the class of complex systems that are close to nonequilibrium phase transitions where the behavior changes qualitative-

ly. These systems are studied in the field of synergetics [18,19], and it is well known that the spatiotemporal signal of such systems can then be described by a finite number of order parameters, which are amplitudes of spatial modes, and stable modes, whose amplitudes are determined by the other parameters. The dynamical evolution of the system is entirely governed by the dynamics of the order parameters which obey a finite dimensional set of ordinary differential equations. The natural way to analyze spatiotemporal signals of such systems, therefore, consists in identifying the order parameters of the system and determining the dynamical system governing their evolution.

A presentation of our method as well as its applications to instabilities with low codimension is the topic of the present paper. It is organized as follows. In Sec. II we briefly sketch the mathematical representation of the state vector of complex systems close to instabilities in terms of order parameters, unstable and stable modes. Then we present an outline of the general procedure of our algorithm. In Sec. IV we treat various types of codimension-I and -II bifurcations. Finally, we analyze spatiotemporal patterns, the so-called blinking states, which have been calculated from a partial differential equation modeling the oscillatory instability towards traveling waves of a spatially homogeneous state in large but finite quasi-one-dimensional systems.

### II. SYSTEMS CONSIDERED

Spatiotemporal patterns may emerge in self-organizing complex systems exhibiting qualitative changes of its macroscopic behavior near instabilities [18,19]. The mathematical structures underlying these processes of spontaneous pattern formation are well understood. In the following we shall summarize the main characteristics.

The state vector  $\tilde{\mathbf{q}}(t)$ , which describes the pattern forming system, is assumed to obey a nonlinear evolution equation,

$$\dot{\tilde{\mathbf{q}}} = \mathbf{N}(\{\epsilon\}, \tilde{\mathbf{q}}), \quad (1)$$

with  $\{\epsilon\}$  being a set of control parameters. Close to instability the state vector  $\tilde{\mathbf{q}}$  can be represented as a superposition of unstable ( $\tilde{\mathbf{u}}$ ) and stable modes ( $\tilde{\mathbf{s}}$ ) according to

$$\tilde{\mathbf{q}}(t) = \sum_u \xi_u(t) \tilde{\mathbf{u}} + \sum_s \xi_s(t) \tilde{\mathbf{s}}, \quad (2)$$

where  $\tilde{\mathbf{u}}$  and  $\tilde{\mathbf{s}}$  may be space-dependent vector functions. It is a well-established fact that close to instability the dynamics of the amplitudes of the stable modes  $\xi_s(t)$  is determined entirely by the amplitudes  $\xi_u(t)$  of the unstable modes after transient behavior has died away: the amplitudes of the stable modes  $\xi_s(t)$  are "enslaved" by the order parameters  $\xi_u(t)$  of the system. In mathematical terms, the amplitudes  $\xi_s(t)$  move on a center manifold obeying an equation of the form

$$\begin{aligned} \dot{\xi}_s(t) &= f_s[\{\xi_u(t)\}] \\ &= \sum_{u,u'} k_{uu'}^{(2)} \xi_u \xi_{u'} + \sum_{u,u',u''} k_{uu'u''}^{(3)} \xi_u \xi_{u'} \xi_{u''} + \dots . \end{aligned} \quad (3)$$

As a result the temporal evolution of the order parameters is determined by a closed set of nonlinear order parameter equations,

$$\begin{aligned} \dot{\xi}_u &= f_u[\{\epsilon\}, \{\xi_u\}] \\ &= a_u^{(0)} + a_u^{(1)} \xi_u + \sum_{u',u''} a_{uu'u''}^{(2)} \xi_{u'} \xi_{u''} \\ &\quad + \sum_{u',u'',u'''} a_{uu'u''u'''}^{(3)} \xi_{u'} \xi_{u''} \xi_{u'''} + \dots . \end{aligned} \quad (4)$$

Thus a pattern forming system allows for two levels of description. The microscopic level is determined by the basic evolution law (1). The macroscopic description is based on the representation (2) as well as on the order parameter equation (4). This forms the theoretical scheme of the description of the state vector of a pattern forming system close to instability.

It is immediately evident that a macroscopic analysis of spatiotemporal patterns of this class of systems should aim at a determination of order parameters and enslaved modes. To achieve this, one has to simultaneously determine the spatial modes  $\tilde{\mathbf{u}}, \tilde{\mathbf{s}}$  as well as their dynamical evolution, i.e., the coefficients of Eqs. (3) and (4). This will be described in the next section.

To conclude this section we remind the reader that the above outlined framework of the description of a pattern forming system is valid for systems close to instabilities, but recent results on the existence of inertial manifolds shows that it may also hold for more general situations. Our method of analysis also applies to these cases.

### III. PROCEDURE

#### A. The number of order parameters and their dynamics

In order to apply our procedure to spatiotemporal signals one first has to specify the number of order parameters. Presently, we are not able to indicate a way to extract this number from the signals. In the present paper, we assume that the character of the instability is known so that the number of order parameters is fixed. The

dynamical system of the order parameters can then be established in the following way. Since the system is close to an instability, nonlinearities are weak and may be approximated by polynomial expressions. Furthermore, symmetry considerations as well as normal form arguments may help to restrict the number of polynomial terms. In general, one has to start making guesses about the number of order parameters that has then to be confirmed self-consistently.

#### B. Projection into the relevant subspace

Our starting point is a given trajectory  $\tilde{\mathbf{q}}(t)$  in an  $n$ -dimensional space  $\Gamma_n$ . The vector components  $\tilde{q}_i(t)$  can either represent the spatial dependence of a spatiotemporal signal  $\tilde{q}(\mathbf{x}_i, t)$  with discretized space elements  $\mathbf{x}_i$ , or other experimentally accessible quantities. Since the trajectory  $\tilde{\mathbf{q}}(t)$  may move in a subspace  $\Gamma_m \subseteq \Gamma_n$ , it will be sufficient to analyze the signal in  $\Gamma_m$ , i.e., to project  $\tilde{\mathbf{q}}(t) \in \Gamma_n$  into  $\Gamma_m$  calling the resulting trajectory  $\mathbf{q}(t)$ .

One way of detecting the relevant subspace  $\Gamma_m$  is given by the principal component analysis (PCA, also known as Karhunen-Loëve decomposition, see e.g., [1,16]). To accomplish this one has to solve the eigenvalue problem,

$$C \mathbf{v}_j = \lambda_j \mathbf{v}_j , \quad (5)$$

of the correlation matrix  $C$

$$C_{ij} = \langle \tilde{q}_i \tilde{q}_j \rangle := \frac{1}{T} \int_{t_0}^{t_0+T} \tilde{q}_i(t) \tilde{q}_j(t) dt . \quad (6)$$

The eigenvectors  $\mathbf{v}_j$  with nonneglectable eigenvalues  $\lambda_j$  span the subspace  $\Gamma_m$ . This restriction may simultaneously lead to a noise reduction of our signal.

Note that PCA is only a first and often dispensable step of our analysis which in particular aims at determining the adequate vectors in the subspace  $\Gamma_m$ . As it will turn out the resulting spatial modes in general differ strongly from the original PCA modes.

#### C. Parameter identification

The determination of the spatial modes and the coefficients of Eqs. (3) and (4) is achieved by means of an extremum principle. To this end we introduce a set of biorthogonal modes  $\mathbf{s}^\dagger, \mathbf{u}^\dagger, \mathbf{s}$ , and  $\mathbf{u}$ , which obey a relation of the form

$$\begin{aligned} \mathbf{u}^\dagger \cdot \mathbf{u}' &= \delta_{u,u'}, \quad \mathbf{s}^\dagger \cdot \mathbf{u} = 0 , \\ \mathbf{u}^\dagger \cdot \mathbf{s} &= 0 , \quad \mathbf{s}^\dagger \cdot \mathbf{s}' = \delta_{s,s'} . \end{aligned} \quad (7)$$

The amplitudes  $\xi_s(t)$  and  $\xi_u(t)$  are, therefore, given by

$$\xi_s(t) = \mathbf{q}(t) \cdot \mathbf{s}^\dagger, \quad \xi_u(t) = \mathbf{q}(t) \cdot \mathbf{u}^\dagger . \quad (8)$$

Now we introduce the potential  $V$  as the mean square deviation of Eqs. (3) and (4),

$$V = \sum_s \frac{\langle (\xi_s - f_s[\{\xi_u\}])^2 \rangle}{\langle \xi_s^2 \rangle} + \sum_u \frac{\langle (\dot{\xi}_u - f_u[\{\xi_u\}])^2 \rangle}{\langle \dot{\xi}_u^2 \rangle} , \quad (9)$$

The denominators guarantee an equally weighted contribution of every term of the sum to the potential. Inserting Eqs. (3), (4), and (7) into Eq. (9) one obtains a potential  $V$ ,

$$V = V[\{\mathbf{u}^\dagger\}, \{\mathbf{s}^\dagger\}, \{k_{su}^{(2)}\}, \dots, \{a_u^{(0)}\}, \{a_u^{(1)}\}, \{a_{uu}^{(2)}\}, \dots] + (\text{constraints}), \quad (10)$$

depending on the biorthogonal modes  $\mathbf{u}^\dagger, \mathbf{s}^\dagger$  and the coefficients of the center manifold  $\{k\}$  and the order parameter equation  $\{a\}$ . The minimum of this potential yields our desired description of the spatiotemporal signal in terms of order parameters, enslaved modes and the corresponding spatial patterns.

In general the potential (10) is rather high dimensional and a straightforward search for the minimum is practically very difficult. However, the following observation allows a reduction of the unknown variables. The coefficients of the dynamics,  $\{k\}, \{a\}$ , as well as the spatial modes  $\mathbf{s}^\dagger$  occur only up to the power of 2 in the potential  $V$ , and therefore, the minimum of  $V$  with respect to these parameters can be obtained analytically as a function of the modes  $\mathbf{u}^\dagger$  (for mathematical details we refer the reader to the Appendix). Inserting these minimal values into our potential yields a nonlinear function depending solely on the unstable modes

$$V = V[\{\mathbf{u}^\dagger\}]. \quad (11)$$

The minimum of this function, which can be found by gradient dynamics, represents the best choice of parameters for the assumed type of instability.

In the following we present the four generic cases of codimension-1 instabilities, a codimension-2 instability with reflection symmetry, and the application of the algorithm to a simulated spatiotemporal signal of a problem of fluid dynamics, simulated by integrating a partial differential equation.

#### IV. EXAMPLES

##### A. Steady-state bifurcations

In these cases there exists only one order parameter  $\xi_u$  with three typical types of bifurcations, the saddle-node bifurcation with normal form

$$\dot{\xi}_u = \epsilon \pm \xi_u^2, \quad (12)$$

the transcritical bifurcation with normal form

$$\dot{\xi}_u = \epsilon \xi_u \pm \xi_u^3. \quad (14)$$

As an example we assume one stable mode  $\mathbf{s}$  with its amplitude  $\xi_s(t)$ ,

$$\xi_s(t) = k \xi_u^2(t), \quad (15)$$

neglecting as a first approximation terms of higher order than  $\xi_u^2$ .

The least-square-fit potential, taking all three bifurcations into account, is given by

$$V(\{a_i\}, k, \mathbf{s}^\dagger, \mathbf{u}^\dagger) = \frac{\langle (\xi_s - k \xi_u^2)^2 \rangle}{\langle \xi_u^2 \rangle} + \frac{\langle (\dot{\xi}_u - a_0 - a_1 \xi_u - a_2 \xi_u^2 - a_3 \xi_u^3)^2 \rangle}{\langle \dot{\xi}_u^2 \rangle},$$

with

$$\xi_s = \mathbf{q}(t) \cdot \mathbf{s}^\dagger, \quad \xi_u = \mathbf{q}(t) \cdot \mathbf{u}^\dagger, \quad (16)$$

with  $\mathbf{q}(t)$  being the spatiotemporal signal  $\tilde{\mathbf{q}}(t)$  projected into the relevant subspace.

As constraints we define  $\langle \xi_s \rangle = c_s$ , which we include in the potential by a Lagrange parameter and  $\langle \xi_u^2 \rangle = c_u$ , which is considered explicitly as a constraint concerning  $\mathbf{u}^\dagger$ .

Variation with respect to  $k$  and  $\mathbf{s}^\dagger$  after elimination of the Lagrange parameter yields

$$k = k(\mathbf{u}^\dagger) = \sqrt{c_s} \frac{[\Gamma_3 \Gamma_2^{-1} \Gamma_3(:\mathbf{u}^\dagger)^4]^{1/2}}{\Gamma_4(:\mathbf{u}^\dagger)^4}, \quad (17)$$

$$\mathbf{s}^\dagger = \mathbf{s}^\dagger(\mathbf{u}^\dagger) = \sqrt{c_s} \frac{\Gamma_2^{-1} \Gamma_3(:\mathbf{u}^\dagger)^2}{[\Gamma_3 \Gamma_2^{-1} \Gamma_3(:\mathbf{u}^\dagger)^4]^{1/2}}.$$

We thereby introduced symmetric correlation tensors  $\Gamma_2$ ,  $\Gamma_3$ , and  $\Gamma_4$ ,

$$(\Gamma_2)_{ij} = \langle q_i q_j \rangle, \quad (\Gamma_3)_{ijk} = \langle q_i q_j q_k \rangle, \quad (18)$$

$$(\Gamma_4)_{ijkl} = \langle q_i q_j q_k q_l \rangle,$$

and abbreviations such as

$$\Gamma_4(:\mathbf{u}^\dagger)^4 = \sum_{ijkl} (\Gamma_4)_{ijkl} u_i^\dagger u_j^\dagger u_k^\dagger u_l^\dagger,$$

$$\Gamma_3 \Gamma_2^{-1} \Gamma_3(:\mathbf{u}^\dagger)^4 = \sum_{ijklmn} (\Gamma_3)_{ijk} (\Gamma_2^{-1})_{kl} (\Gamma_3)_{lmn} u_i^\dagger u_j^\dagger u_m^\dagger u_n^\dagger.$$

The inverse  $\Gamma_2^{-1}$  of the correlation matrix  $\Gamma_2$  exists, since  $\mathbf{q}(t)$  is the trajectory of  $\tilde{\mathbf{q}}(t)$  projected into the relevant subspace.

By variation with respect to the coefficients  $\{a_i\}$  we obtain

$$\begin{bmatrix} a_0 \\ a_1 \\ a_2 \\ a_3 \end{bmatrix} = \begin{bmatrix} 1 & \langle \xi_u \rangle & \langle \xi_u^2 \rangle & \langle \xi_u^3 \rangle \\ \langle \xi_u \rangle & \langle \xi_u^2 \rangle & \langle \xi_u^3 \rangle & \langle \xi_u^4 \rangle \\ \langle \xi_u^2 \rangle & \langle \xi_u^3 \rangle & \langle \xi_u^4 \rangle & \langle \xi_u^5 \rangle \\ \langle \xi_u^3 \rangle & \langle \xi_u^4 \rangle & \langle \xi_u^5 \rangle & \langle \xi_u^6 \rangle \end{bmatrix}^{-1} \begin{bmatrix} \langle \dot{\xi}_u \rangle \\ \langle \dot{\xi}_u \xi_u \rangle \\ \langle \dot{\xi}_u \xi_u^2 \rangle \\ \langle \dot{\xi}_u \xi_u^3 \rangle \end{bmatrix}, \quad (19)$$

which again can be written as a function of  $\mathbf{u}^\dagger$ , whereby correlation tensors  $\Gamma_i$  up to the sixth order and correlation tensors  $\Lambda_i$ ,

$$\begin{aligned} (\Lambda_1)_i &= \langle \dot{q}_i \rangle, \quad (\Lambda_2)_{ij} = \langle \dot{q}_i q_j \rangle, \\ (\Lambda_3)_{ijk} &= \langle \dot{q}_i q_j q_k \rangle, \dots \end{aligned} \quad (20)$$

occur.

By inserting Eqs. (17) and (19) into the potential  $V$  [Eq. (16)] we obtain a nonlinear potential  $V(\mathbf{u}^\dagger)$  depending only on  $\mathbf{u}^\dagger$

$$\begin{aligned} V(\mathbf{u}^\dagger) &= V_s(\mathbf{u}^\dagger) + V_u(\mathbf{u}^\dagger), \\ V_s(\mathbf{u}^\dagger) &= 1 - \frac{\Gamma_3 \Gamma_2^{-1} \Gamma_3(\mathbf{u}^\dagger)^4}{\Gamma_4(\mathbf{u}^\dagger)^4}, \\ V_u(\mathbf{u}^\dagger) &= 1 - \frac{1}{\Delta_2(\mathbf{u}^\dagger)^2} M^{-1}[\mathbf{u}^\dagger](\mathbf{y}[\mathbf{u}^\dagger])^2, \end{aligned} \quad (21)$$

with

$$\begin{aligned} (\Delta_2)_{ij} &= \langle \dot{q}_i \dot{q}_j \rangle \\ \mathbf{y}[\mathbf{u}^\dagger] &= (\Lambda_1(\mathbf{u}^\dagger), \Lambda_2(\mathbf{u}^\dagger)^2, \Lambda_3(\mathbf{u}^\dagger)^3, \Lambda_4(\mathbf{u}^\dagger)^4)^T \end{aligned}$$

$$M[\mathbf{u}^\dagger] = \begin{bmatrix} 1 & \Gamma_1(\mathbf{u}^\dagger) & \Gamma_2(\mathbf{u}^\dagger)^2 & \Gamma_3(\mathbf{u}^\dagger)^3 \\ \Gamma_1(\mathbf{u}^\dagger) & \Gamma_2(\mathbf{u}^\dagger)^2 & \Gamma_3(\mathbf{u}^\dagger)^3 & \Gamma_4(\mathbf{u}^\dagger)^4 \\ \Gamma_2(\mathbf{u}^\dagger)^2 & \Gamma_3(\mathbf{u}^\dagger)^3 & \Gamma_4(\mathbf{u}^\dagger)^4 & \Gamma_5(\mathbf{u}^\dagger)^5 \\ \Gamma_3(\mathbf{u}^\dagger)^3 & \Gamma_4(\mathbf{u}^\dagger)^4 & \Gamma_5(\mathbf{u}^\dagger)^5 & \Gamma_6(\mathbf{u}^\dagger)^6 \end{bmatrix}. \quad (22)$$

If the signal  $\bar{\mathbf{q}}(t)$  consists of two modes  $\bar{\mathbf{u}}$  and  $\bar{\mathbf{s}}$  the subspace is two dimensional.  $\mathbf{u}^\dagger$  can then be written as a vector with two components,

$$\mathbf{u}^\dagger = \begin{bmatrix} x_1 \\ x_2 \end{bmatrix}, \quad (23)$$

which has to fulfill the constraint

$$\begin{aligned} \langle \xi_u^2 \rangle &= \langle [\mathbf{q}(t)\mathbf{u}^\dagger]^2 \rangle \\ &= \langle q_1^2 \rangle x_1^2 + 2\langle q_1 q_2 \rangle x_1 x_2 + \langle q_2^2 \rangle x_2^2 = c_u. \end{aligned} \quad (24)$$

If the signal  $\bar{\mathbf{q}}(t)$  was projected using PCA,  $\langle q_i q_j \rangle$  is given by

$$\langle q_i q_j \rangle = \lambda_i \delta_{ij}, \quad (25)$$

with  $\lambda_i$  being the eigenvalues of Eq. (5). Equation (24) then describes the normal form of an ellipse in the plane. We can introduce polar coordinates and obtain

$$\begin{aligned} \mathbf{u}^\dagger &= \begin{bmatrix} r_1 \cos \phi \\ r_2 \sin \phi \end{bmatrix}, \quad r_1 = [c_u / \lambda_1]^{1/2}, \\ r_2 &= [c_u / \lambda_2]^{1/2}. \end{aligned} \quad (26)$$

The potential  $V$  [Eq. (21)] now depends only on one parameter, the angle  $\phi$

$$V(\phi) = V_s(\phi) + V_u(\phi), \quad (27)$$

with a translational symmetry  $V(\phi) = V(\phi + \pi)$ , due to the still possible scaling of  $\mathbf{u}^\dagger$  with  $-1$ .

Figure 1 shows the potential  $V(\phi)$  calculated from simulated spatiotemporal signals  $\bar{\mathbf{q}}(t) = \xi_u(t)\bar{\mathbf{u}} + \xi_s(t)\bar{\mathbf{s}}$ . The amplitudes  $\xi_u(t)$  and  $\xi_s(t)$  were obtained by numeri-

cal integration of ordinary differential equations showing the three different types of normal forms [Eqs. (12), (13), and (14)] and a center manifold like Eq. (15). As spatial modes  $\bar{\mathbf{u}}, \bar{\mathbf{s}}$  we chose the modes shown in Fig. 2(a). The dashed line of Fig. 1 represents  $V_u(\phi)$ , the dotted  $V_s(\phi)$  and the solid line the sum of them,  $V = V_u + V_s$ . In all three cases we obtain a distinct minimum of the potential  $V$  representing the right choice of parameters. The term  $V_s(\phi)$  helps to avoid additional local minima, occurring in  $V_u(\phi)$ . They are due to the fact, that—besides  $\xi_u$ —a certain linear combination of  $\xi_u$  and  $\xi_s$ ,  $\xi = \alpha \xi_u + \beta \xi_s$ , fulfills in a good approximation a differential equation of the form

$$\dot{\xi} = a_0 + a_1 \xi + a_2 \xi^2 + a_3 \xi^3. \quad (28)$$

For example, in Fig. 1(c) we plotted the potential  $V = V_u + V_s$  of the Haken-Zwanzig model,

$$\begin{aligned} \dot{\xi}_s &= -\xi_s + k \xi_s^2, \\ \dot{\xi}_u &= \epsilon \xi_u + \gamma \xi_u \xi_s. \end{aligned} \quad (29)$$

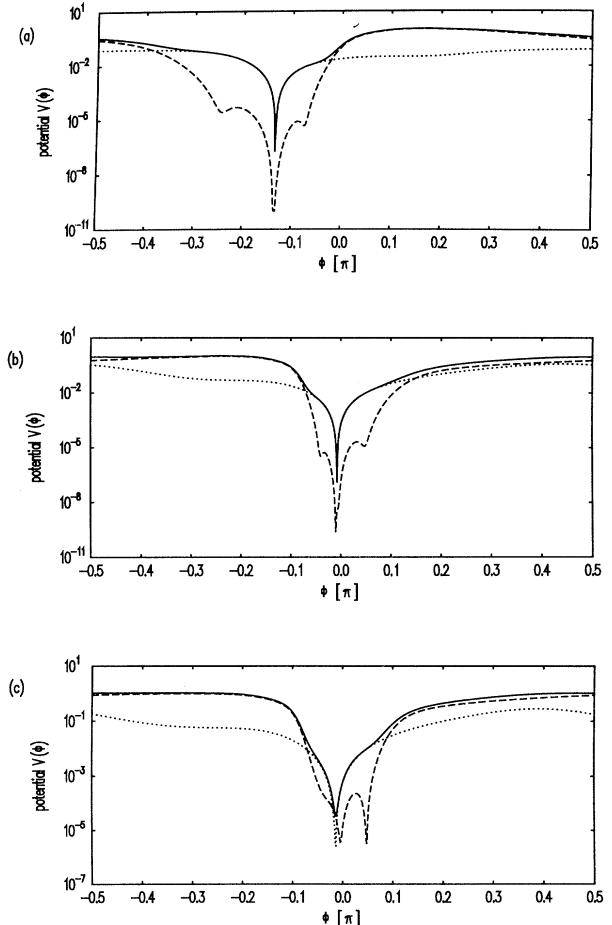


FIG. 1. Potential  $V(\phi)$  (solid line),  $V_u(\phi)$  (dashed line), and  $V_s(\phi)$  (dotted line) for different simulated types of bifurcations: (a) saddle-node bifurcation, (b) transcritical bifurcation, and (c) pitchfork bifurcation.

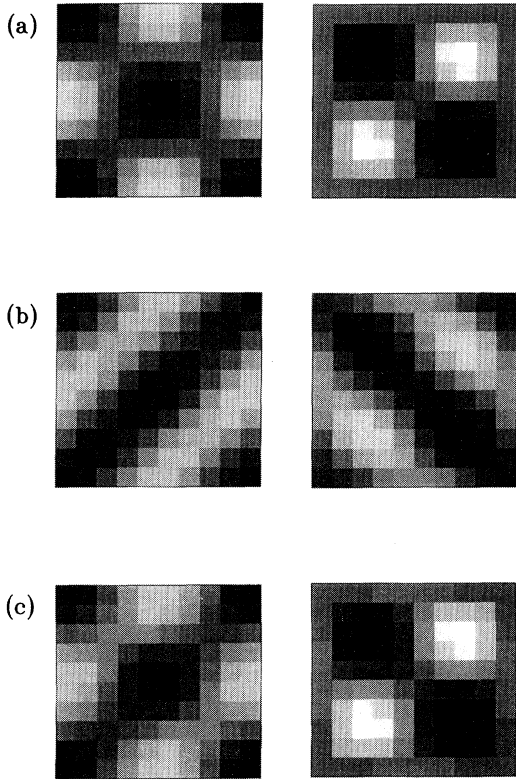


FIG. 2. (a) Simulated spatial modes  $\bar{u}$  and  $\bar{s}$ , (b) the resulting two vectors of PCA, and (c) modes, obtained by our method.

There occur two deep minima of  $V_u$  (dashed line): one, coinciding with the minimum of  $V_s$  and, therefore, the searched one representing  $\beta=0$ , and an additional local minimum of  $V_u$  representing  $\alpha=0$ , since for  $\alpha=0$ ,  $\dot{\xi} \approx \beta 2k \xi_u \dot{\xi}_u = \beta(2\epsilon\xi + 2\gamma\xi^2)$  fulfills the differential equation (28) as well.

Figure 2(b) shows the two modes obtained by PCA, calculated from the simulated spatiotemporal signal of the Haken-Zwanzig model. The modes  $\bar{u}$  and  $\bar{s}$  obtained by our algorithm are presented in Fig. 2(c). They are in quite good correspondence with the modes of the simulated data [Fig. 2(a)]. That there is no perfect agreement is due to the ansatz of  $V_s$  and  $V_u$ . The Haken-Zwanzig model [Eq. (29)] yields a center manifold,

$$\xi_s = k(1-2\epsilon)\xi_u^2 + O(\xi_u^4), \quad (30)$$

and a order parameter equation,

$$\dot{\xi}_u = \epsilon\xi_u + \gamma k(1-2\epsilon)\xi_u^3 + O(\xi_u^5). \quad (31)$$

In our ansatz of  $V_s$  and  $V_u$ , we neglected the higher order terms  $O(\cdot)$  as a first approximation, which is the first reason for not obtaining the exact modes. A second reason is given by the general ansatz of  $V_u$ : We do not assume a pitchfork bifurcation in advance, but minimize a more general ansatz. The minimum of this ansatz does not lead to an exact pitchfork bifurcation and, therefore, the exact modes are not obtained. However, the oc-

currence of the pitchfork bifurcation is detected very well and demonstrated by Fig. 3. There we show the dependence of the coefficients  $a_i(\phi)$  again from the simulated data of the Haken-Zwanzig model. The dotted line indicates the minimum of the potential  $V(\phi)$ , the dashed line corresponds to  $a_i=0$  and the little cross marks the value of  $a_i(\phi)$  given by the coefficients of the integrated ordinary differential equation. The coefficients corresponding to the minimum are in good agreement with the model, especially the type of bifurcation is detected clearly:  $a_0=a_2=0$  corresponds to the pitchfork bifurcation.

This example shows that our presented algorithm is able to classify the spatiotemporal signal into the right type of bifurcation and it yields a good choice of parame-

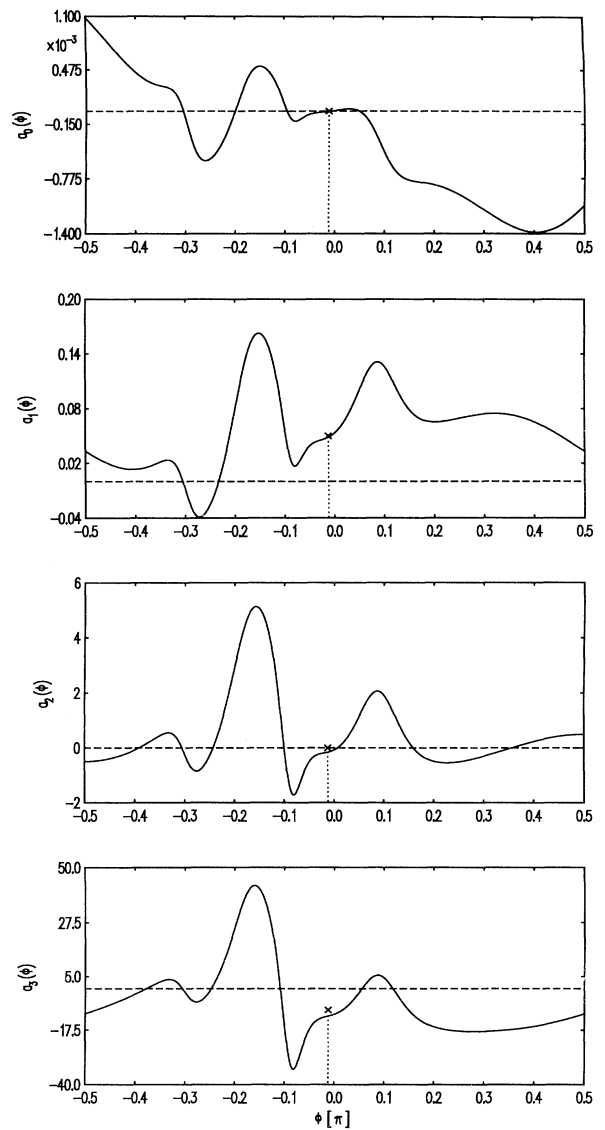


FIG. 3. Coefficients  $a_i(\phi)$  of a simulated Haken-Zwanzig model. The dashed line represents  $a_i=0$ , the dotted line the minimum of the potential in Fig. 1(c). The little cross marks the coefficients of the simulation.

ters corresponding to the temporal evolution and the spatial modes of the signal. After detection of the type of bifurcation one can define a new least-square-fit potential  $V_u$  minimizing the deviation of the given normal form only, like described in [17], which then leads to the best choice of parameters corresponding to this specific normal form.

### B. Hopf bifurcation

In the fourth case of a codimension-I instability, the Hopf bifurcation, there exist two order parameters obeying the normal form

$$\frac{d}{dt} \begin{bmatrix} \xi_1 \\ \xi_2 \end{bmatrix} = \begin{bmatrix} \epsilon & -\omega \\ \omega & \epsilon \end{bmatrix} \begin{bmatrix} \xi_1 \\ \xi_2 \end{bmatrix} + (\xi_1^2 + \xi_2^2) \begin{bmatrix} a & -b \\ b & a \end{bmatrix} \begin{bmatrix} \xi_1 \\ \xi_2 \end{bmatrix}. \quad (32)$$

The transformation into a complex differential equation, introducing a complex variable,  $c(t) = \xi_1(t) + i\xi_2(t) = r(t)\exp[i\phi(t)]$ , yields

$$\dot{c} = \alpha c + \beta |c|^2 c, \quad (33)$$

with

$$\alpha = \epsilon + i\omega, \quad \beta = a + ib. \quad (34)$$

The corresponding least-square-fit potential  $V_c$  then reads,

$$V_c = \frac{\langle |\dot{c} - \alpha c - \beta |c|^2 c|^2 \rangle}{\langle |\dot{c}|^2 \rangle}. \quad (35)$$

Again as an example, we assume one stable mode  $s$ , with an approximated center manifold,

$$\xi_s(t) = k|c(t)|^2. \quad (36)$$

The least-square-fit potential  $V$  for this scenario, rewritten in polar coordinates, is then given by

$$\begin{aligned} V &= V_s + V_r + V_\phi, \\ V_s &= \frac{\langle (\xi_s - kr^2)^2 \rangle}{\langle \xi_s^2 \rangle}, \\ V_r &= \frac{\langle (\dot{r} - \epsilon r - ar^3)^2 \rangle}{\langle \dot{r}^2 \rangle + \langle r^2 \dot{\phi}^2 \rangle}, \\ V_\phi &= \frac{\langle (r\dot{\phi} - \omega r - br^3)^2 \rangle}{\langle \dot{r}^2 \rangle + \langle r^2 \dot{\phi}^2 \rangle}. \end{aligned} \quad (37)$$

As constraints to fix scaling and rotation of  $\mathbf{u}_1^\dagger, \mathbf{u}_2^\dagger$ , we require  $\langle r^2 \rangle = c_r$ , and  $\xi_1(t_0) = 0$ , and as a constraint concerning  $s^\dagger$  we choose  $\langle \xi_s^2 \rangle = c_s$ , which again is taken care of by a Lagrange parameter.

By variation with respect to  $s^\dagger$ ,  $k$ ,  $\epsilon$ ,  $\omega$ ,  $a$ , and  $b$  we obtain these parameters as a function of  $\mathbf{u}_1^\dagger, \mathbf{u}_2^\dagger$ . Inserting them into Eq. (37) yields a nonlinear potential  $V$  depending on  $\mathbf{u}_1^\dagger, \mathbf{u}_2^\dagger$  only

$$\begin{aligned} V(\mathbf{u}_1^\dagger, \mathbf{u}_2^\dagger) &= V_s(\mathbf{u}_1^\dagger, \mathbf{u}_2^\dagger) + V_r(\mathbf{u}_1^\dagger, \mathbf{u}_2^\dagger) + V_\phi(\mathbf{u}_1^\dagger, \mathbf{u}_2^\dagger), \\ V_s(\mathbf{u}_1^\dagger, \mathbf{u}_2^\dagger) &= 1 - \frac{\Gamma_3 \Gamma_2^{-1} \Gamma_3((:\mathbf{u}_1^\dagger)^2 + (:mathbf{u}_2^\dagger)^2)^2}{\Gamma_4((:\mathbf{u}_1^\dagger)^2 + (:mathbf{u}_2^\dagger)^2)^2}, \end{aligned} \quad (38)$$

$$\begin{aligned} V_r(\mathbf{u}_1^\dagger, \mathbf{u}_2^\dagger) + V_\phi(\mathbf{u}_1^\dagger, \mathbf{u}_2^\dagger) &= 1 - \frac{1}{\langle \dot{r}^2 + r^2 \dot{\phi}^2 \rangle} \\ &\times M_H^{-1}((:\mathbf{y}_1)^2 + (:mathbf{y}_2)^2), \end{aligned}$$

with

$$M_H = \begin{bmatrix} \langle r^2 \rangle & \langle r^4 \rangle \\ \langle r^4 \rangle & \langle r^6 \rangle \end{bmatrix}, \quad \mathbf{y}_1 = \begin{bmatrix} \langle r\dot{r} \rangle \\ \langle r^3\dot{r} \rangle \end{bmatrix}, \quad \mathbf{y}_2 = \begin{bmatrix} \langle r^2\dot{\phi} \rangle \\ \langle r^4\dot{\phi} \rangle \end{bmatrix}. \quad (39)$$

The occurring correlations  $\langle \cdot \rangle$  can all be written in terms of  $\xi_1$  and  $\xi_2$ ,

$$\begin{aligned} \langle r^2 \rangle &= \langle \xi_1^2 + \xi_2^2 \rangle, \\ \langle r^4 \rangle &= \langle (\xi_1^2 + \xi_2^2)^2 \rangle, \\ \langle r^6 \rangle &= \langle (\xi_1^2 + \xi_2^2)^3 \rangle, \\ \langle r\dot{r} \rangle &= \langle \xi_1 \dot{\xi}_1 + \xi_2 \dot{\xi}_2 \rangle, \\ \langle r^3\dot{r} \rangle &= \langle (\xi_1^2 + \xi_2^2)(\xi_1 \dot{\xi}_1 + \xi_2 \dot{\xi}_2) \rangle, \\ \langle r^2\dot{\phi} \rangle &= \langle \xi_1 \dot{\xi}_2 - \dot{\xi}_1 \xi_2 \rangle, \\ \langle r^4\dot{\phi} \rangle &= \langle (\xi_1^2 + \xi_2^2)(\xi_1 \dot{\xi}_2 - \dot{\xi}_1 \xi_2) \rangle, \end{aligned} \quad (40)$$

which all can be expressed in terms of correlation tensors and spatial modes  $\mathbf{u}_1^\dagger$  and  $\mathbf{u}_2^\dagger$ .

We now still have to consider the constraints  $\xi_1(t_0) = 0$  and  $\langle r^2 \rangle = c_r$ , which yield a further reduction of parameters: If the signal  $\tilde{\mathbf{q}}(t)$  consists of three modes  $\tilde{\mathbf{u}}_1$ ,  $\tilde{\mathbf{u}}_2$ , and  $\tilde{\mathbf{s}}$  the subspace is three dimensional.  $\mathbf{u}_i^\dagger$  can then be expressed as vectors with three components. Taking the two constraints concerning  $\mathbf{u}_i$  into account one ends up with four independent variables, which again can be transformed by generalized polar coordinates leading to four angles  $\phi_1, \dots, \phi_4$  as independent variables. The resulting potential is, therefore, four dimensional,

$$V = V(\phi_1, \phi_2, \phi_3, \phi_4). \quad (41)$$

To verify our calculations we have simulated a spatiotemporal signal by numerical integration of a system of differential equations showing the normal form like Eq. (32) and a center manifold like Eq. (36). We obtained the minimum of the four-dimensional potential by gradient dynamics, the resulting parameters agreed perfectly with the parameters of the simulation.

To visualize the potential we have as well simulated a spatiotemporal signal with the unstable modes  $\tilde{\mathbf{u}}_1$  and  $\tilde{\mathbf{u}}_2$  only:  $\tilde{\mathbf{q}}(t) = \xi_1(t)\tilde{\mathbf{u}}_1 + \xi_2(t)\tilde{\mathbf{u}}_2$ . The phase portrait of the amplitudes of the simulated example is shown in Fig. 4(a). The trajectory starts near the fix point  $\xi_1 = \xi_2 = 0$  and moves into the limit cycle. The subspace of the trajectory  $\tilde{\mathbf{q}}(t)$  is then two dimensional, the modes  $\mathbf{u}_1^\dagger, \mathbf{u}_2^\dagger$  can be expressed as two-dimensional vectors

$$\mathbf{u}_1^\dagger = \begin{pmatrix} x_1 \\ y_1 \end{pmatrix}, \quad \mathbf{u}_2^\dagger = \begin{pmatrix} x_2 \\ y_2 \end{pmatrix}. \quad (42)$$

To fulfill the first constraint,  $\xi_1(t_0)=0$ , we obtain

$$x_1 = \gamma y_1, \quad \gamma = -\frac{q_2(t_0)}{q_1(t_0)}. \quad (43)$$

After introducing polar coordinates and considering Eq. (43), the second constraint  $\langle r^2 \rangle = c_r$ , yields

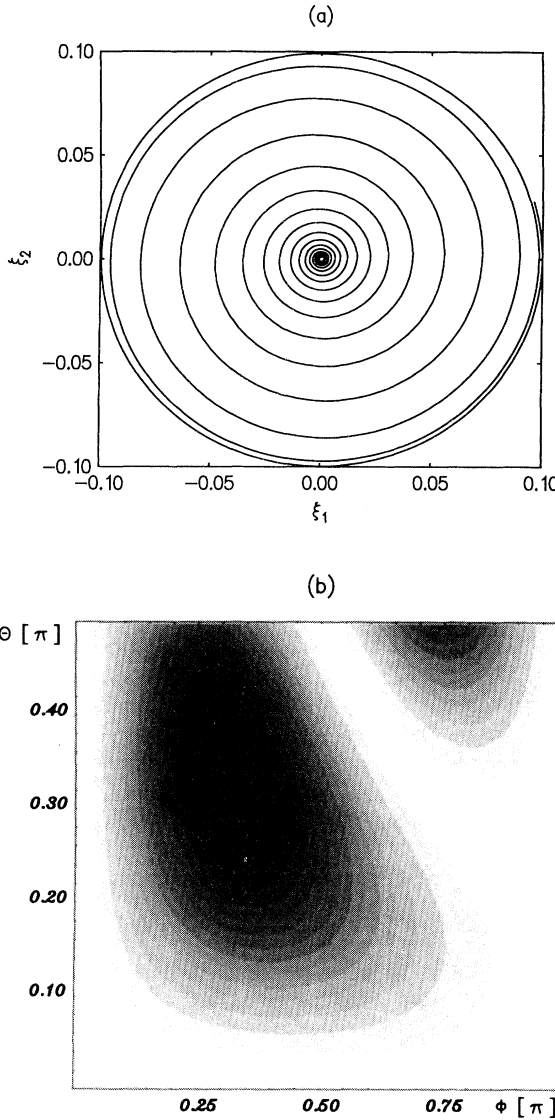


FIG. 4. (a) Phase portrait of the amplitudes  $\xi_1(t)$  and  $\xi_2(t)$  of a simulated super-critical Hopf bifurcation [Eq. (32),  $\epsilon=0.05$ ,  $\omega=1$ ,  $a=-5$ , and  $b=75$ ]. (b) Two-dimensional least-square-fit potential  $V_u(\phi, \theta)$  corresponding to the simulated Hopf bifurcation. The values of the potential  $V(\phi, \theta)$  are given by different grey values: Black represents the minimum of the potential, white the maximum. The potential shows one distinct minimum and the expected symmetry  $V(\phi-\pi/2, \theta=\pi/2) = V(\phi+\pi/2, \theta=\pi/2)$ .

$$x_2 = \left[ \frac{c_r}{\lambda_1} \right]^{1/2} \cos\phi \sin\theta, \quad (44)$$

$$y_1 = \left[ \frac{c_r}{\gamma^2 \lambda_1 + \lambda_2} \right]^{1/2} \sin\phi \sin\theta, \quad (44)$$

$$y_2 = \left[ \frac{c_r}{\lambda_2} \right]^{1/2} \cos\theta,$$

with the eigenvalues  $\lambda_i$  of PCA. Thus the resulting potential is two dimensional depending only on two angles  $\phi, \theta$ . It shows the following reflection and translational symmetries:

$$V(\pi+\phi, \theta) = V(\pi-\phi, \theta),$$

$$V\left[\frac{\pi}{2} + \phi, \frac{\pi}{2} + \theta\right] = V\left[\frac{\pi}{2} - \phi, \frac{\pi}{2} - \theta\right], \quad (45)$$

$$V(\phi, \theta) = V(\phi, \theta + \pi),$$

due to the still possible scaling of  $\mathbf{u}_1^\dagger, \mathbf{u}_2^\dagger$  or both with  $-1$ . Therefore, it is sufficient to search a minimum in the interval  $0 \leq \phi \leq \pi$  and  $0 \leq \theta \leq \pi/2$ . Figure 4(b) shows the potential  $V(\phi, \theta)$  of a simulated example showing a smooth function with no occurrence of any additional minima. The minimum represents, in perfect correspondence with the simulation, the coefficients of the dynamic evolution and the spatial modes.

### C. A codimension-II instability

In the case of a codimension-II instability with reflection symmetry the normal form of the two occurring order parameters  $\xi_1, \xi_2$  reads

$$\begin{aligned} \dot{\xi}_1 &= \xi_2 \\ \dot{\xi}_2 &= \mu_1 \xi_1 + \mu_2 \xi_2 + c \xi_1^3 - \xi_1^2 \xi_2, \quad c = \pm 1. \end{aligned} \quad (46)$$

The least-square-fit potential  $V_u$  concerning the order parameters is then given by,

$$\begin{aligned} V_u &= V_1 + V_2, \\ V_1 &= \frac{\langle (\dot{\xi}_1 - \tau \xi_2)^2 \rangle}{\langle \xi_1^2 \rangle}, \\ V_2 &= \frac{\langle (\dot{\xi}_2 - a \xi_1 - b \xi_2 - c \xi_1^3 - d \xi_1^2 \xi_2)^2 \rangle}{\langle \xi_2^2 \rangle}, \end{aligned} \quad (47)$$

with two constraints fixing scaling,

$$\langle \xi_1^2 \rangle = c_1, \quad \langle \xi_2^2 \rangle = c_2. \quad (48)$$

The stable modes can be dealt with either by adding to  $V_u$  a potential  $V_s$ , in complete analogy to the previous cases, or by detecting them in a second step: In the first step one minimizes only  $V_u$  (with respect to  $\mathbf{u}_i^\dagger$ ) and then one checks which of possible center manifolds occur by comparing the value of the minimum of  $V_s$  with respect to  $\mathbf{s}^\dagger$  and fixed  $\mathbf{u}_i^\dagger$ .

Minimizing  $V_u$  with respect to the coefficients of the

temporal evolution and inserting them back into  $V_u$ , results in

$$\begin{aligned} V_1(\mathbf{u}_1^\dagger, \mathbf{u}_2^\dagger) &= 1 - \frac{\langle \dot{\xi}_1 \xi_2 \rangle^2}{\langle \dot{\xi}_1^2 \rangle \langle \dot{\xi}_2^2 \rangle}, \\ V_2(\mathbf{u}_1^\dagger, \mathbf{u}_2^\dagger) &= 1 - \frac{1}{\langle \dot{\xi}_2^2 \rangle} M^{-1} [\mathbf{u}_1^\dagger, \mathbf{u}_2^\dagger] \cdot \mathbf{y}[\mathbf{u}_1^\dagger, \mathbf{u}_2^\dagger]^2, \end{aligned} \quad (49)$$

with

$$\mathbf{y}[\mathbf{u}_1^\dagger, \mathbf{u}_2^\dagger] = (\langle \dot{\xi}_2 \xi_1 \rangle, \langle \dot{\xi}_2 \xi_2 \rangle, \langle \dot{\xi}_2 \xi_1^3 \rangle, \langle \dot{\xi}_2 \xi_1^2 \xi_2 \rangle)^T \quad (50)$$

and

$$M[\mathbf{u}_1^\dagger, \mathbf{u}_2^\dagger] = \begin{pmatrix} \langle \dot{\xi}_1^2 \rangle & \langle \dot{\xi}_1 \xi_2 \rangle & \langle \xi_1^4 \rangle & \langle \xi_1^3 \xi_2 \rangle \\ \langle \dot{\xi}_1 \xi_2 \rangle & \langle \dot{\xi}_2^2 \rangle & \langle \xi_1^3 \xi_2 \rangle & \langle \xi_1^2 \xi_2^2 \rangle \\ \langle \xi_1^4 \rangle & \langle \xi_1^3 \xi_2 \rangle & \langle \xi_1^6 \rangle & \langle \xi_1^5 \xi_2 \rangle \\ \langle \xi_1^3 \xi_2 \rangle & \langle \xi_1^2 \xi_2^2 \rangle & \langle \xi_1^5 \xi_2 \rangle & \langle \xi_1^4 \xi_2^2 \rangle \end{pmatrix}. \quad (51)$$

Again, all occurring expressions can be written in terms of correlation tensors  $\Gamma_i, \Lambda_i, \Delta_i$  and spatial modes  $\mathbf{u}_1^\dagger, \mathbf{u}_2^\dagger$ . Searching the minimum of  $V_u$  with respect to  $\mathbf{u}_1^\dagger$  and  $\mathbf{u}_2^\dagger$ , one has to ensure that  $\mathbf{u}_1^\dagger$  and  $\mathbf{u}_2^\dagger$  are linearly independent, if not the matrix  $M$  cannot be inverted.

For the purpose of visualization of the potential  $V_u(\mathbf{u}_1^\dagger, \mathbf{u}_2^\dagger)$ , we simulated a spatiotemporal signal  $\tilde{\mathbf{q}}(t) = \xi_1(t)\tilde{\mathbf{u}}_1 + \xi_2(t)\tilde{\mathbf{u}}_2$ , by integrating Eq. (46) and assuming two spatial modes  $\tilde{\mathbf{u}}_1, \tilde{\mathbf{u}}_2$ . Figure 5(a) shows the trajectory in phase space of an example in which there exist two unstable foci and a saddle point, the trajectory moving into a limit cycle.

Because of the two-dimensional subspace the two spatial modes  $\mathbf{u}_1^\dagger, \mathbf{u}_2^\dagger$  are two dimensional and can be written in polar coordinates fulfilling the constraints,  $\langle \dot{\xi}_1^2 \rangle = c_1$ ,  $\langle \dot{\xi}_2^2 \rangle = c_2$

$$\mathbf{u}_1^\dagger = \sqrt{c_1} \begin{pmatrix} \lambda_1^{-1/2} \cos \phi \\ \lambda_2^{-1/2} \sin \phi \end{pmatrix}, \quad \mathbf{u}_2^\dagger = \sqrt{c_2} \begin{pmatrix} \lambda_1^{-1/2} \cos \theta \\ \lambda_2^{-1/2} \sin \theta \end{pmatrix}. \quad (52)$$

Therefore, the potential  $V_u$  depends only on two free parameters  $\phi, \theta$ , again with translational symmetry

$$V_u(\phi, \theta) = V_u(\phi + \pi, \theta) = V_u(\phi, \theta + \pi). \quad (53)$$

Figure 5(b) shows the potential  $V_u(\phi, \theta)$  of the simulated example, a smooth function with one distinct local minimum representing, in perfect agreement with the simulation, all parameters of the temporal evolution and spatial modes.

#### D. Blinking states

In this example we would like to demonstrate the application of our algorithm to a spatiotemporal signal obtained by numerical integration of a partial differential equation, the so-called ‘‘blinking state.’’ It has been experimentally observed in convection of binary mixtures [20] and can be modeled [21] by a generalized Ginzburg-Landau equation for a complex order parameter field  $\Psi(x, t)$

$$\begin{aligned} \dot{\Psi}(x, t) &= [\epsilon + i\omega_c - i\alpha(1 + \partial_x^2) - (1 + \partial_x^2)^2 \\ &\quad - |\Psi(x, t)|^2] \Psi(x, t). \end{aligned} \quad (54)$$

Figure 6(a) shows the real part of the spatiotemporal signal,  $\text{Re}(\Psi(x, t))$ , obtained by numerical integration of (54) considering boundary conditions,

$$\Psi(x_0, t) = \partial_x \Psi(x_0, t) = 0, \quad x_0 = 0, \Gamma, \quad (55)$$

and parameter values  $\epsilon = 0.1$ ,  $\alpha = 0.4$ ,  $\omega_c = 3\alpha$ , and  $\Gamma = 31$  (with a spatial discretization of 50 points). A theoretical analysis [21] of the model yields two linear unstable modes,  $u_1(x)$  and  $u_2(x)$ , with different parity, which

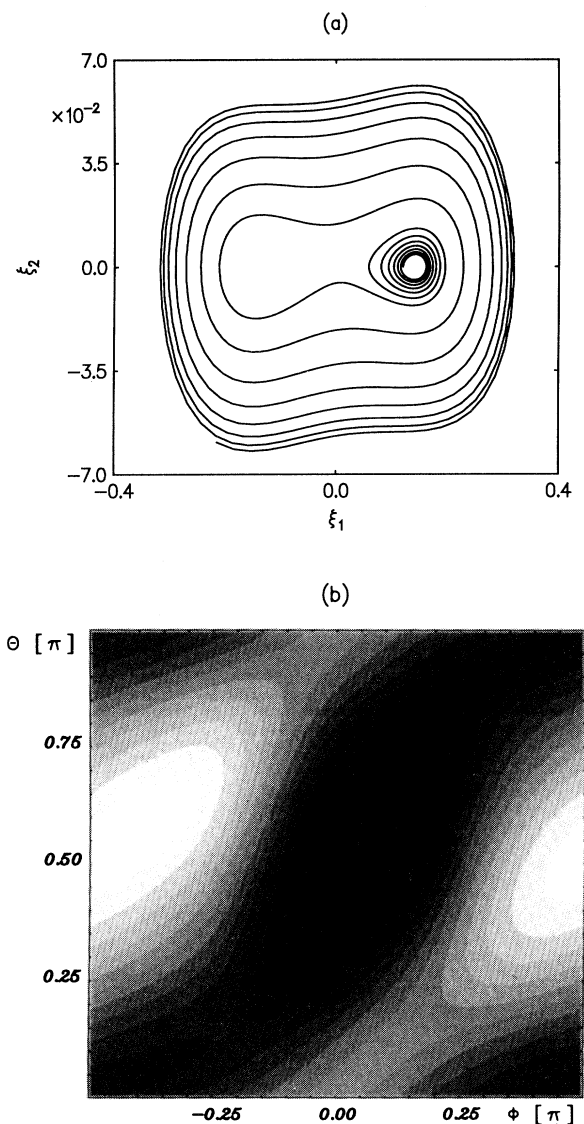


FIG. 5. (a) Phase portrait of the amplitudes  $\xi_1(t)$  and  $\xi_2(t)$  of a simulated codimension-two bifurcation [Eq. (46),  $\mu_1 = 0.02$ ,  $\mu_2 = 0.03$ ,  $c = -1$ ]. (b) Least-square-fit potential  $V_u(\phi, \theta)$  corresponding to the simulated codimension-two bifurcation with the same color coding as in Fig. 4(b). There occurs again one distinct minimum and the expected symmetry of a torus.

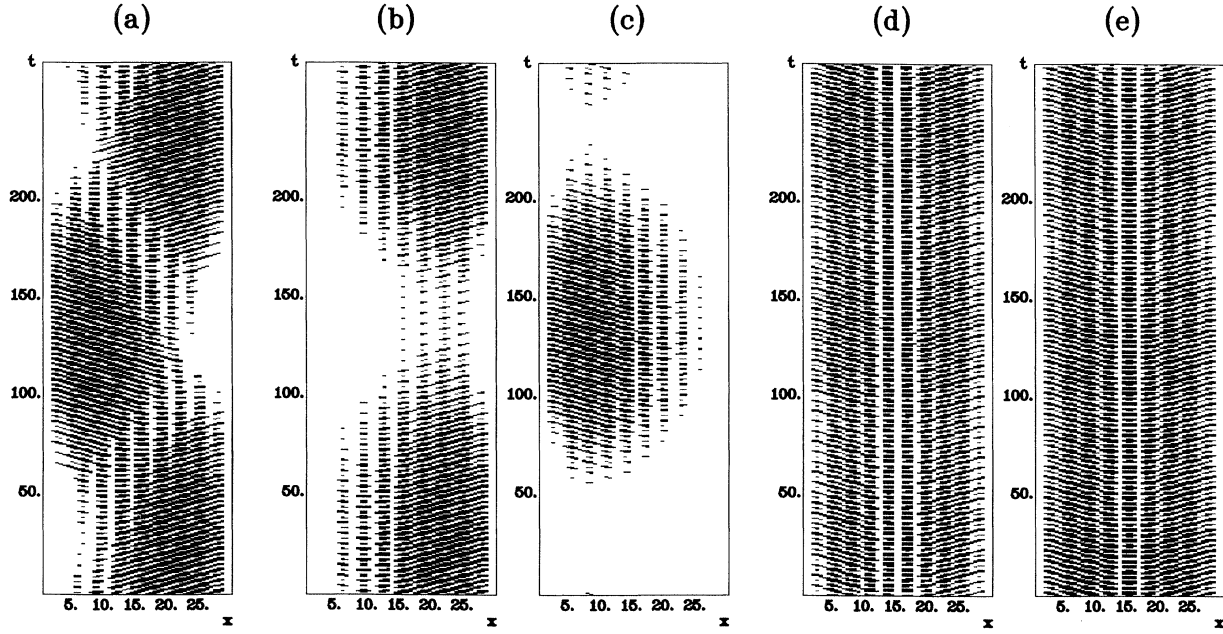


FIG. 6. (a)  $\text{Re}[\Psi(x,t)]$ , obtained by integration of Eq. (54), (b)  $\text{Re}(\eta_1(t)v_1(x))$ , (c)  $\text{Re}(\eta_2(t)v_2(x))$ , both obtained by PCA of the signal  $\Psi(x,t)$ , (d)  $\text{Re}(\xi_1(t)u_1(x))$ , and (e)  $\text{Re}(\xi_2(t)u_2(x))$ , both obtained by the presented method.

govern the dynamics of the system,

$$\Psi(x,t) = \xi_1(t)u_1(x) + \xi_2(t)u_2(x) + O(\xi_u^3). \quad (56)$$

The dynamics of the amplitudes of the unstable modes can be expressed in terms of ordinary differential equations,

$$\begin{aligned} \dot{\xi}_1(t) &= [\lambda_1 - a_{11}|\xi_1(t)|^2 - a_{12}|\xi_2(t)|^2]\xi_1(t) \\ &\quad - b_1\xi_2^2(t)\xi_1^*(t) + O(\xi_u^5), \\ \dot{\xi}_2(t) &= [\lambda_2 - a_{21}|\xi_1(t)|^2 - a_{22}|\xi_2(t)|^2]\xi_2(t) \\ &\quad - b_2\xi_1^2(t)\xi_2^*(t) + O(\xi_u^5), \end{aligned} \quad (57)$$

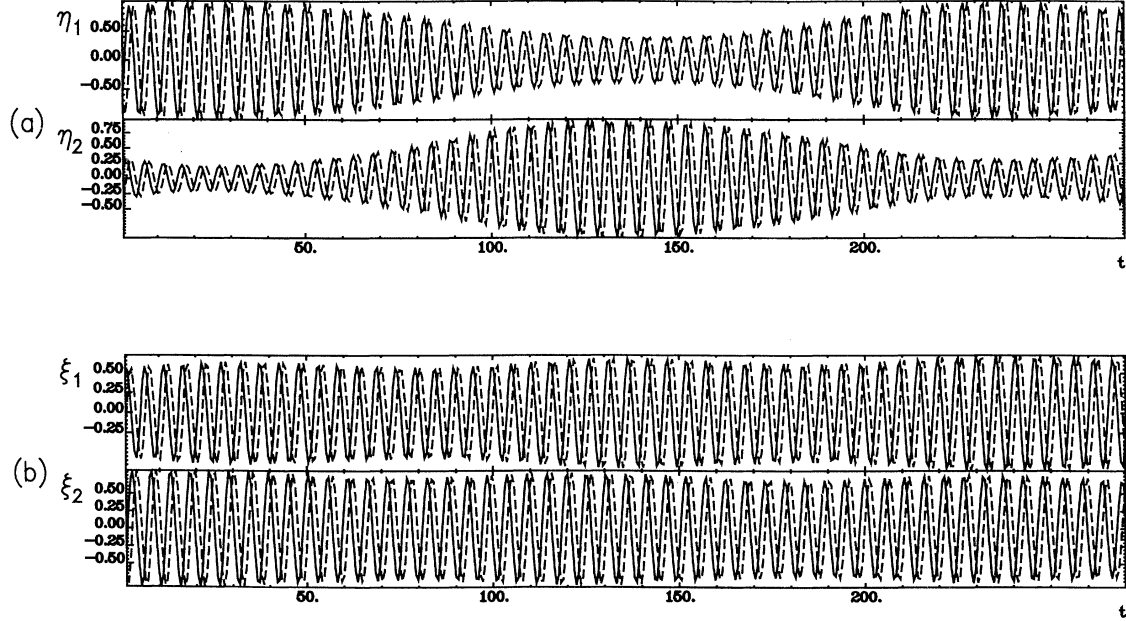


FIG. 7. (a)  $\eta_1(t)$  and  $\eta_2(t)$ , both corresponding to the PCA modes of the signal  $\Psi(x,t)$ , (b)  $\xi_1(t)$  and  $\xi_2(t)$ , both corresponding to the modes obtained by the presented method (solid line corresponds to the real part, dashed line to the imaginary part).

which correspond in the case of the blinking state to a quasiperiodic mode interaction.

Analyzing the simulated spatiotemporal signal  $\Psi(x, t)$  with PCA yields two dominant complex modes,  $v_1(x), v_2(x)$ . The corresponding complex amplitudes,  $\eta_1(t), \eta_2(t)$  are shown in Fig. 7(a). The contribution of the PCA modes to the signal is shown in Figs. 6(b) and 6(c). There is no symmetry of the modes recognizable, and the PCA modes do not correspond to the theoretical modes, and therefore, do not lead to the simple order parameter equations [Eqs. (57)].

Application of the presented algorithm, by introducing a least-square-fit potential considering the order parameter equations (57), one obtains complex spatial modes corresponding to the unstable modes,  $u_1(x), u_2(x)$ . Figure 7(b) shows the corresponding amplitudes,  $\xi_1(t)$  and  $\xi_2(t)$ , and Figs. 6(d) and 6(e) presents the contribution of these modes to the signal. Clearly the symmetry of the modes can be recognized and the effect of the different time-depending phases of the amplitudes then leads to the spatiotemporal signal [Fig. 6(a)].

Summarizing this example, we would like to clarify similarities and differences between PCA and our presented method. Both, PCA and the presented method, yield the same spatiotemporal signal, but there are two big differences between these two approaches: First, symmetries of the modes can be lost by PCA, like this example clearly demonstrates. And second, an advantage of our presented method concerns the reconstruction of the signal by integrating ordinary differential equations. The number of coefficients that have to be calculated numerically from the signal, are much smaller with our algorithm than in the case of PCA. Both points are due to the fact that we minimize a least-square-error function of assumed order parameter equations, leading to a simultaneous search of dynamically and spatially relevant parameters, whereas PCA represents the search of a best converging mode expansion, without considering symmetries, underlying normal forms or the underlying dynamics.

## V. CONCLUSIONS

We have derived a method for the determination of order parameters and corresponding center manifolds in spatiotemporal signals. It should be a helpful tool to analyze experimental data emerging from nonlinear self-organizing systems near instabilities. The occurring mode interaction in the vicinity of the critical points can be determined by the presented extremum principle. An advantage of the presented algorithm results from the simultaneous determination of spatial modes and parameters describing the temporal evolution. Our method

yields nonlinear equations with the occurrence of higher order correlation tensors both of the signal and the time derivative of the signal. In this respect it represents an alternative to PCA and similar approaches, like [22], where spatial modes are obtained out of linear equations and second order correlation tensors.

## ACKNOWLEDGMENTS

We gratefully acknowledge support and helpful discussions with M. Bestehorn concerning the blinking states.

## APPENDIX: ELIMINATION OF PARAMETERS

The starting point is the potential  $V$  [Eq. (9)],

$$V = \sum_s \left[ \frac{\langle (\mathbf{q}\mathbf{s}^\dagger - f_s[\{\mathbf{q}\mathbf{u}^\dagger\}]^2) \rangle}{c_s} + \lambda_s [\langle (\mathbf{q}\mathbf{s}^\dagger)^2 \rangle - c_s] \right] + \sum_u \frac{\langle (\mathbf{q}\mathbf{u}^\dagger - f_u[\{\mathbf{q}\mathbf{u}^\dagger\}]^2) \rangle}{\langle (\mathbf{q}\mathbf{u}^\dagger)^2 \rangle}, \quad (\text{A1})$$

with  $\lambda_s$  representing a Lagrange parameter fixing scaling of  $\mathbf{s}^\dagger$  and  $f_s$  and  $f_u$  being nonlinear functions in  $\mathbf{u}^\dagger$

$$\begin{aligned} f_s[\{\mathbf{q}\mathbf{u}^\dagger\}] &= \sum_{u,u'} k_{suu'}^{(2)} \mathbf{q}\mathbf{u}^\dagger \mathbf{q}\mathbf{u}'^\dagger \\ &\quad + \sum_{u,u',u''} k_{su'u''}^{(3)} \mathbf{q}\mathbf{u}^\dagger \mathbf{q}\mathbf{u}'^\dagger \mathbf{q}\mathbf{u}''^\dagger + \dots, \\ f_u[\{\mathbf{q}\mathbf{u}^\dagger\}] &= a_u^{(0)} + a_u^{(1)} \mathbf{q}\mathbf{u}^\dagger + \sum_{u',u''} a_{uu'u''}^{(2)} \mathbf{q}\mathbf{u}'^\dagger \mathbf{q}\mathbf{u}''^\dagger \\ &\quad + \sum_{u',u'',u'''} a_{uu'u''u'''}^{(3)} \mathbf{q}\mathbf{u}'^\dagger \\ &\quad \times \mathbf{q}\mathbf{u}''^\dagger \mathbf{q}\mathbf{u}'''^\dagger + \dots. \end{aligned}$$

(a) Variation of the potential [Eq. (A1)] with respect to  $\mathbf{s}^\dagger, k_{su_1u_2}^{(2)}, k_{su_1u_2u_3}^{(3)}$  yields,

$$\begin{aligned} \langle ((1+c_s\lambda_s)\mathbf{q}\mathbf{s}^\dagger - f_s[\{\mathbf{q}\mathbf{u}^\dagger\}])\mathbf{q} \rangle &= 0, \\ \langle ((\mathbf{q}\mathbf{s}^\dagger) - f_s[\{\mathbf{q}\mathbf{u}^\dagger\}])(\mathbf{q}\mathbf{u}_1^\dagger)(\mathbf{q}\mathbf{u}_2^\dagger) \rangle &= 0, \\ \langle ((\mathbf{q}\mathbf{s}^\dagger) - f_s[\{\mathbf{q}\mathbf{u}^\dagger\}])(\mathbf{q}\mathbf{u}_1^\dagger)(\mathbf{q}\mathbf{u}_2^\dagger)(\mathbf{q}\mathbf{u}_3^\dagger) \rangle &= 0, \end{aligned}$$

which represents a homogeneous linear set of equations for the variables  $\mathbf{x}$ ,

$$\mathbf{x} = (\mathbf{s}^\dagger, k_{suu'}^{(2)}, k_{su'u''}^{(3)})^T,$$

as a function of  $\{\mathbf{u}^\dagger\}$

$$L[\lambda_s, \{\mathbf{u}^\dagger\}] \mathbf{x} = 0, \quad (\text{A2})$$

with

$$L[\lambda_s, \{\mathbf{u}^\dagger\}] = \begin{pmatrix} (1+c_s\lambda_s)\Gamma_2 & -\Gamma_3:\mathbf{u}^\dagger:\mathbf{u}'^\dagger & -\Gamma_4:\mathbf{u}^\dagger:\mathbf{u}'^\dagger:\mathbf{u}''^\dagger \\ -\Gamma_3:\mathbf{u}_1^\dagger:\mathbf{u}_2^\dagger & -\Gamma_4:\mathbf{u}^\dagger:\mathbf{u}'^\dagger:\mathbf{u}_1^\dagger:\mathbf{u}_2^\dagger & -\Gamma_5:\mathbf{u}^\dagger:\mathbf{u}'^\dagger:\mathbf{u}''^\dagger:\mathbf{u}_1^\dagger:\mathbf{u}_2^\dagger \\ -\Gamma_4:\mathbf{u}_1^\dagger:\mathbf{u}_2^\dagger:\mathbf{u}_3^\dagger & -\Gamma_5:\mathbf{u}^\dagger:\mathbf{u}'^\dagger:\mathbf{u}_1^\dagger:\mathbf{u}_2^\dagger:\mathbf{u}_3^\dagger & -\Gamma_6:\mathbf{u}^\dagger:\mathbf{u}'^\dagger:\mathbf{u}''^\dagger:\mathbf{u}_1^\dagger:\mathbf{u}_2^\dagger:\mathbf{u}_3^\dagger \end{pmatrix}$$

We used the notation of higher order correlation tensors introduced in Sec. IV. To obtain nontrivial solutions, the determinant of the matrix  $L[\lambda_s, \{\mathbf{u}^\dagger\}]$  has to vanish, which leads to an equation for the Lagrange parameters  $\lambda_s$

$$\det L[\lambda_s, \{\mathbf{u}^\dagger\}] = 0 \implies \lambda_s = \lambda_s[\{\mathbf{u}^\dagger\}]. \quad (\text{A3})$$

Inserting Eq. (A3) back into the homogeneous set of Eqs. (A2), and solving for  $\mathbf{x}$ , one obtains the variables,  $s^\dagger, k_{su_1u_2}^{(2)}, k_{su_1u_2u_3}^{(3)}$ , as a function of  $\{\mathbf{u}^\dagger\}$

$$\mathbf{x} = \mathbf{x}[\{\mathbf{u}^\dagger\}]. \quad (\text{A4})$$

(b) Variation of the potential [Eq. (A1)] with respect to  $a_u^{(0)}, a_u^{(1)}, a_{uu_1u_2}^{(2)}, a_{uu_1u_2u_3}^{(3)}$  yields,

$$M[\{\mathbf{u}^\dagger\}] = \begin{pmatrix} 1 & \Gamma_1:\mathbf{u}^\dagger & \Gamma_2:\mathbf{u}^\dagger:\mathbf{u}''^\dagger & \Gamma_3:\mathbf{u}':\mathbf{u}'':\mathbf{u}'''^\dagger \\ \Gamma_1:\mathbf{u}^\dagger & \Gamma_2:(\mathbf{u}^\dagger)^2 & \Gamma_3:\mathbf{u}^\dagger:\mathbf{u}':\mathbf{u}''^\dagger & \Gamma_4:\mathbf{u}':\mathbf{u}':\mathbf{u}''':\mathbf{u}'''^\dagger \\ \Gamma_2:\mathbf{u}_1^\dagger:\mathbf{u}_2^\dagger & \Gamma_3:\mathbf{u}_1^\dagger:\mathbf{u}_1^\dagger:\mathbf{u}_2^\dagger & \Gamma_4:\mathbf{u}':\mathbf{u}':\mathbf{u}_1^\dagger:\mathbf{u}_2^\dagger & \Gamma_5:\mathbf{u}':\mathbf{u}':\mathbf{u}''':\mathbf{u}_1^\dagger:\mathbf{u}_2^\dagger \\ \Gamma_3 \cdots & \Gamma_4 \cdots & \Gamma_5 \cdots & \Gamma_6 \cdots \end{pmatrix}$$

and

$$\mathbf{y}[\{\mathbf{u}^\dagger\}] = (\Lambda_1:\mathbf{u}^\dagger, \Lambda_2:(\mathbf{u}^\dagger)^2, \Lambda_3:\mathbf{u}^\dagger:\mathbf{u}_1^\dagger:\mathbf{u}_2^\dagger, \Lambda_4:\mathbf{u}':\mathbf{u}_1^\dagger:\mathbf{u}_2^\dagger:\mathbf{u}_3^\dagger)^T.$$

For sets of vectors  $\{\mathbf{u}^\dagger\}$  with  $\det M[\{\mathbf{u}^\dagger\}] \neq 0$ , Eq. (A5) can be inverted, and we obtain the variables,  $a_u^{(0)}, a_u^{(1)}, a_{uu_1u_2}^{(2)}, a_{uu_1u_2u_3}^{(3)}$ , as a function of  $\{\mathbf{u}^\dagger\}$ :

$$\mathbf{a} = \mathbf{a}[\{\mathbf{u}^\dagger\}] = M^{-1}[\{\mathbf{u}^\dagger\}] \mathbf{y}[\{\mathbf{u}^\dagger\}]. \quad (\text{A6})$$

Inserting finally Eqs. (A4) and (A6) into Eq. (A1), we end up with a potential  $V$  depending on  $\{\mathbf{u}^\dagger\}$  only,

$$V = V[\{\mathbf{u}^\dagger\}],$$

which corresponds to Eq. (11) of Sec. III C.

$$\begin{aligned} \langle (\dot{\mathbf{q}}\mathbf{u}^\dagger - f_u[\{\mathbf{q}\mathbf{u}^\dagger\}]) \rangle &= 0, \\ \langle (\dot{\mathbf{q}}\mathbf{u}^\dagger - f_u[\{\mathbf{q}\mathbf{u}^\dagger\}])\mathbf{q}\mathbf{u}^\dagger \rangle &= 0, \\ \langle (\dot{\mathbf{q}}\mathbf{u}^\dagger - f_u[\{\mathbf{q}\mathbf{u}^\dagger\}])(\mathbf{q}\mathbf{u}_1^\dagger)(\mathbf{q}\mathbf{u}_2^\dagger) \rangle &= 0, \\ \langle (\dot{\mathbf{q}}\mathbf{u}^\dagger - f_u[\{\mathbf{q}\mathbf{u}^\dagger\}])(\mathbf{q}\mathbf{u}_1^\dagger)(\mathbf{q}\mathbf{u}_2^\dagger)(\mathbf{q}\mathbf{u}_3^\dagger) \rangle &= 0, \end{aligned}$$

which represents a nonhomogeneous linear set of equations for the variables  $\mathbf{a}$ ,

$$\mathbf{a} = (a_u^{(0)}, a_u^{(1)}, a_{uu_1u_2}^{(2)}, a_{uu_1u_2u_3}^{(3)})^T,$$

as a function of  $\{\mathbf{u}^\dagger\}$ :

$$M[\{\mathbf{u}^\dagger\}]\mathbf{a} = \mathbf{y}[\{\mathbf{u}^\dagger\}], \quad (\text{A5})$$

with

- [1] G. Berkooz, P. Holmes, and J. L. Lumley, *Annu. Rev. Fluid Mech.* **25**, 539 (1993).
- [2] G. Plaut and R. Vautard, *J. Atmos. Sci.* **51**, 210 (1994).
- [3] R. Friedrich and C. Uhl, in *Evolution of Dynamical Structures in Complex Systems*, edited by R. Friedrich and A. Wunderlin (Springer-Verlag, Berlin, 1992).
- [4] D. Gallez and A. Babloyantz, *Biol. Cybern.* **64**, 381 (1991).
- [5] A. Fuchs, J. A. S. Kelso, and H. Haken, *Int. J. Bifurcation Chaos* **2**, 917 (1992).
- [6] V. K. Jirsa, R. Friedrich, H. Haken, and J. A. S. Kelso, *Biol. Cybern.* **71**, 27 (1994).
- [7] H. Haken, *Information and Selforganization* (Springer-Verlag, Berlin, 1988).
- [8] P. Grassberger and I. Procaccia, *Physica D* **9**, 189 (1983).
- [9] F. Takens, in *Dynamical Systems and Turbulence*, edited by D. Rand and L. S. Young (Springer, Berlin, 1981).
- [10] D. S. Broomhead and G. P. King, *Physica D* **20**, 217 (1987).
- [11] H. D. I. Abarbanel, R. Brown, J. J. Sidorowich, and L. S. Tsimring, *Rev. Mod. Phys.* **65**, 1331 (1993).
- [12] E. Baake, M. Baake, H. G. Bock, and K. M. Briggs, *Phys.*

- Rev. A **45**, 5524 (1992).
- [13] S. P. Layne, G. Mayer-Kress, and J. Holzfuss, in *Dimensions and Entropies in Chaotic Systems*, edited by G. Mayer-Kress (Springer-Verlag, Berlin, 1986).
- [14] M. Paluš and I. Dvořák, *Physica D* **55**, 221 (1992).
- [15] J. P. Eckmann and D. Ruelle, *Physica D* **56**, 185 (1992).
- [16] A. Armbruster, R. Heiland, and E. J. Kostelich, *Chaos* **4**(2), 421 (1994).
- [17] C. Uhl, R. Friedrich, and H. Haken, *Z. Phys. B* **92**, 211 (1993).
- [18] H. Haken, *Synergetics. An Introduction*, 3rd ed. (Springer-Verlag, Berlin, 1983).
- [19] H. Haken, *Advanced Synergetics*, 3rd ed. (Springer-Verlag, Berlin, 1993).
- [20] J. Fineberg, E. Moses, and V. Steinberg, *Phys. Rev. Lett.* **61**, 838 (1988); P. Kolodner and C. M. Surko, *ibid.* **61**, 842 (1988).
- [21] M. Bestehorn, R. Friedrich, and H. Haken, *Z. Phys. B* **77**, 151 (1989); M. Bestehorn, R. Friedrich, and H. Haken, *Physica D* **37**, 295 (1989).
- [22] M. Kirby, *Physica D* **57**, 466 (1992).

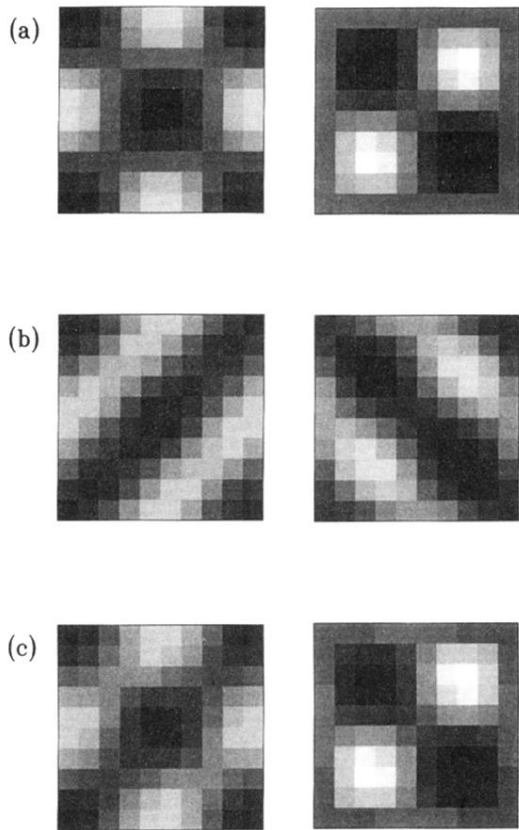


FIG. 2. (a) Simulated spatial modes  $\tilde{u}$  and  $\tilde{s}$ , (b) the resulting two vectors of PCA, and (c) modes, obtained by our method.

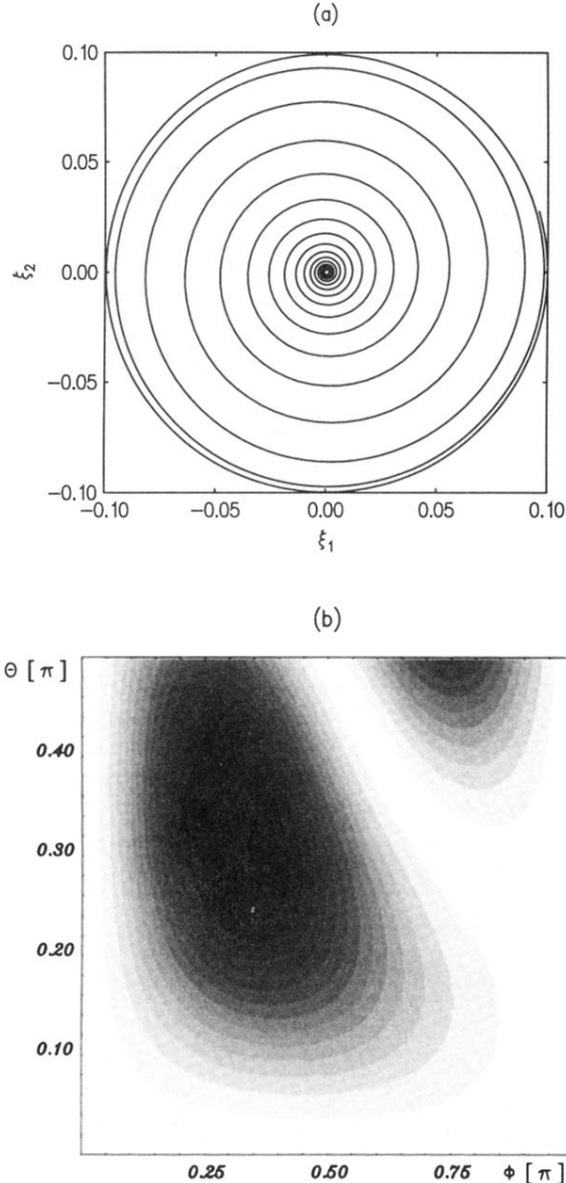


FIG. 4. (a) Phase portrait of the amplitudes  $\xi_1(t)$  and  $\xi_2(t)$  of a simulated super-critical Hopf bifurcation [Eq. (32),  $\epsilon=0.05$ ,  $\omega=1$ ,  $a=-5$ , and  $b=75$ ]. (b) Two-dimensional least-square-fit potential  $V_u(\phi, \theta)$  corresponding to the simulated Hopf bifurcation. The values of the potential  $V(\phi, \theta)$  are given by different grey values: Black represents the minimum of the potential, white the maximum. The potential shows one distinct minimum and the expected symmetry  $V(\phi-\pi/2, \theta=\pi/2) = V(\phi+\pi/2, \theta=\pi/2)$ .

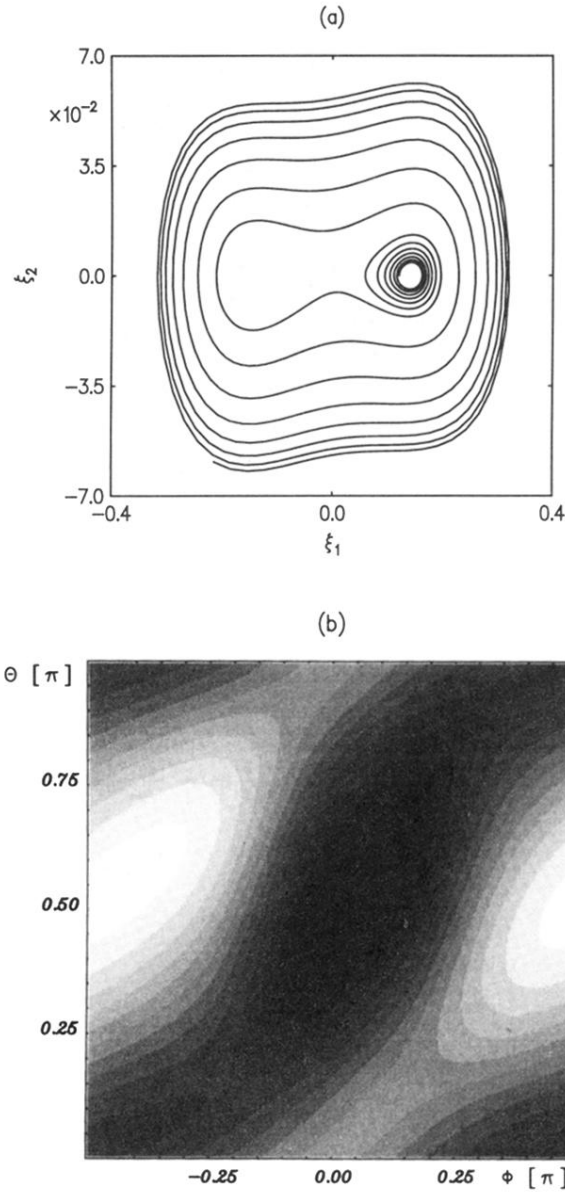


FIG. 5. (a) Phase portrait of the amplitudes  $\xi_1(t)$  and  $\xi_2(t)$  of a simulated codimension-two bifurcation [Eq. (46),  $\mu_1=0.02$ ,  $\mu_2=0.03$ ,  $c=-1$ ]. (b) Least-square-fit potential  $V_u(\phi, \theta)$  corresponding to the simulated codimension-two bifurcation with the same color coding as in Fig. 4(b). There occurs again one distinct minimum and the expected symmetry of a torus.

# Analysis of spatiotemporal signals: A method based on perturbation theory

A. Hutt,<sup>1,\*</sup> C. Uhl,<sup>1</sup> and R. Friedrich<sup>2</sup>

<sup>1</sup>*Max-Planck-Institute of Cognitive Neuroscience, Stephanstrasse 1a, 04103 Leipzig, Germany*

<sup>2</sup>*Institute for Theoretical Physics, University of Stuttgart, Pfaffenwaldring 57, 70550 Stuttgart, Germany*

(Received 18 December 1998)

We present a method of analyzing spatiotemporal signals with respect to its underlying dynamics. The algorithm aims at the determination of spatial modes and a criterion for the number of interacting modes. Simultaneously, a way of filtering of nonorthogonal noise is shown. The method is discussed by examples of simulated stable fixpoints and the Lorenz attractor. [S1063-651X(99)01908-X]

PACS number(s): 05.45.-a, 02.50.Sk

## I. INTRODUCTION

In various scientific fields the analysis of spatiotemporal patterns emerging from complex systems plays an important role. An investigation of measured multidimensional data allows us to learn more about the internal dynamics of the system. It represents the basis for microscopic modeling of interactions in investigated systems (e.g., [1]). Some typical fields of application are chemical reactions [2], meteorology (e.g., [3]) and hydrodynamics [4] or biological systems as analyzing electroencephalography (EEG) or magnetoencephalography (MEG) data [5–7].

Depending on the intended use, different kinds of data processing techniques can be applied. An often used method for linear data analysis is known as principal component analysis (PCA) [8] or Karhunen-Loëve expansion. Spatial modes are calculated based on maximizing signal projections on these modes. It leads to orthogonal spatial and temporal modes and gives a measure for the contribution of each mode to the signal. Modes with a signal contribution above a certain threshold are considered as relevant, those below the threshold as irrelevant. However, this method fails to separate signal from noise, if signal and noise are not orthogonal on each other, and if noise parts contribute more than parts of the relevant signal to the data. Furthermore an estimation of the number of interacting modes depends on the choice of the threshold. Underlying dynamic structures are neglected by this linear data technique.

A nonlinear approach aiming at extracting interacting modes and the underlying dynamics has been presented, e.g., in [9,10]. However, the numerical effort of these nonlinear approaches is considerably high, especially with an increasing dimensionality of the underlying dynamical system. An estimation of the number of interacting modes is also still an open question.

In this paper we will present a nonlinear technique based on (linear) perturbation theory, which focuses on internal deterministic dynamic patterns and extracts signal dynamics from noisy data sets. It improves PCA suspending the condition of orthogonality and allows an objective estimation of interacting spatial modes. Due to the linear equations to be solved, the method leads to a fast and robust algorithm.

The perturbational approach is based on a ground state of the PCA modes, which represents the exact solution of minimizing a cost function leading to a complete orthogonal basis. We introduce a perturbation by an additional term in the cost function for a determination of signal dynamics. Using a mathematical methodology similar to Hartree and Fock [11,12], we obtain dynamically coupled spatial modes. A criterion for the estimation of the number of interacting modes can be derived. We obtain the relevant signal subspace independent of an orthogonality relation between signal and noise, due to our special choice of a biorthogonal basis.

## II. METHOD

### A. Principal component analysis (PCA)

A  $N$ -dimensional spatiotemporal signal can be described by a vector  $\mathbf{q}(t)$  of dimension  $N$ . In order to determine significant parts of the signal, one can decompose the signal into spatial and temporal modes  $\mathbf{v}_i$  and  $x_i(t)$  by PCA. The properties are determined by a cost function

$$V = \sum_{i=1}^N \frac{\langle [\mathbf{q}(t) - (\mathbf{q} \cdot \mathbf{v}_i)\mathbf{v}_i]^2 \rangle}{\langle \mathbf{q}^2 \rangle} + \sum_{i,j=1}^N \tau_{ij}(\mathbf{v}_i \cdot \mathbf{v}_j - \delta_{ij}),$$

$$\frac{\partial V}{\partial \mathbf{v}_k} = 0, \quad (2.1)$$

where  $\langle \dots \rangle$  denotes time average and  $\tau_{ij}$  are Lagrange multipliers to fulfill the orthogonality constraint.

Standard cost functions of PCA lead to degenerated solution spaces. To obtain the known equations of PCA directly, here one sums up the single errors to the signal and fixes the amplitudes as projections on the modes. This breaks the invariance with respect to linear transformation.

It leads to an eigenvalue problem

$$\mathbf{C}\mathbf{v}_k = \lambda_k \mathbf{v}_k, \quad (2.2)$$

with  $\mathbf{C} = \langle \mathbf{q}(t) \otimes \mathbf{q}(t) \rangle / \langle \mathbf{q}^2 \rangle$ , orthogonal spatial modes  $\mathbf{v}_k$  and amplitudes  $x_k(t) = \mathbf{q}(t) \cdot \mathbf{v}_k$ , where  $\otimes$  denotes the dyadic product. They obey Eqs. (2.3),

$$\mathbf{v}_k \cdot \mathbf{v}_l = \delta_{kl}, \quad \langle x_k(t) x_l(t) \rangle = \lambda_k \delta_{kl}. \quad (2.3)$$

\*Electronic address: hutt@cns.mpg.de

Since  $V = N - \sum_i \lambda_i$ , the modes are sorted with respect to their contribution to the signal given by the eigenvalues  $\lambda_i$ :

$$\lambda_1 > \lambda_2 > \dots > \lambda_N. \quad (2.4)$$

By choosing a threshold  $\lambda_c$  and considering modes  $\mathbf{v}_i$  with  $\lambda_i > \lambda_c$  one obtains a subspace of the signal

$$\mathbf{q}(t) \approx \sum_{i=1}^{M < N} x_i(t) \mathbf{v}_i. \quad (2.5)$$

The following problems arise by such an approach: (i) The choice of  $\lambda_c$  and, therefore, an estimation of the number of interacting modes is an open question. (ii) Noisy parts of the signal can be represented by modes  $\mathbf{v}_i$  with  $\lambda_i > \lambda_c$  and/or dynamically relevant modes  $\mathbf{v}_j$  can be neglected because of  $\lambda_j < \lambda_c$ . (iii) If signal and noise are not orthogonal, the separation of signal from noise cannot be achieved by an orthogonal expansion.

### B. Perturbational approach

To improve PCA with respect to these points, a biorthogonal base  $\{\mathbf{w}_i^+\}, \{\mathbf{w}_i\}$  with

$$\mathbf{w}_i^+ \cdot \mathbf{w}_j = \delta_{ij}, \quad \mathbf{w}_i \cdot \mathbf{w}_i = 1 \quad (2.6)$$

is introduced. Amplitudes  $x_k(t)$  are now obtained by the signal projection  $x_i(t) = \mathbf{q} \mathbf{w}_i^+$ .

A second extension is done by introducing an additional term  $V_d(\mathbf{w}_i^+, \mathbf{w}_j, a_{i\alpha})$  in the cost function considering the dynamics of the signal. Since nonlinear interactions are assumed,  $V_d$  will depend nonlinearly on  $\mathbf{w}_i^+$ . In this paragraph the actual definition is irrelevant; it is sufficient to introduce parameters  $a_{i\alpha}$  as parameters of the dynamic fit. The exact specification of the cost function  $V_d$  will be given in the next section.

We can interpret  $V_d$  as a perturbation of the groundstate built by PCA modes. Considering also the constraints (2.6) we define the cost function  $V$  as

$$\begin{aligned} V = & \sum_{i=1}^M \frac{\langle [\mathbf{q}(t) - (\mathbf{q} \cdot \mathbf{w}_i^+) \mathbf{w}_i]^2 \rangle}{\langle \mathbf{q}^2 \rangle} + \epsilon V_d(\mathbf{w}_i^+, \mathbf{w}_j, a_{i\alpha}) \\ & + \sum_{i,j=1}^M \tau_{ij}(\mathbf{w}_i^+ \cdot \mathbf{w}_j - \delta_{ij}) + \sum_{i=1}^M \alpha_i[(\mathbf{w}_i)^2 - 1]. \end{aligned} \quad (2.7)$$

The parameter  $\epsilon$  is a measure for perturbation of the PCA state, and  $\tau_{ij}$  and  $\alpha_i$  are Lagrangian parameters of the introduced constraints.

The minimum of the cost function  $V$  represents the dynamically relevant subspace spanned by the biorthogonal basis  $\{\mathbf{w}_i^+\}, \{\mathbf{w}_i\}$  of dimension  $M \leq N$  in the given  $N$ -dimensional vector space. As  $\mathbf{w}_i^+$ ,  $\mathbf{w}_j$ ,  $a_{i\alpha}$ ,  $\tau_{kl}$ , and  $\alpha_k$  are independent of each other, the minimum is obtained by vanishing partial derivatives of  $V$ :

$$\frac{\partial V}{\partial \mathbf{w}_k^+} = \mathbf{0}, \quad \frac{\partial V}{\partial \mathbf{w}_k} = \mathbf{0}, \quad (2.8)$$

$$\frac{\partial V}{\partial a_{k\alpha}} = 0, \quad (2.9)$$

$$\frac{\partial V}{\partial \tau_{kl}} = 0, \quad \frac{\partial V}{\partial \alpha_k} = 0. \quad (2.10)$$

Inserting Eq. (2.7) into Eqs. (2.8) and (2.10), we get

$$-2\mathbf{C}\mathbf{w}_k + 2\mathbf{C}\mathbf{w}_k^+ + \epsilon \frac{\partial V_d}{\partial \mathbf{w}_k^+} + \sum_{j=1}^M \tau_{kj} \mathbf{w}_j = \mathbf{0}, \quad (2.11)$$

$$\begin{aligned} & -2\mathbf{C}\mathbf{w}_k^+ + 2(\mathbf{w}_k^+ \mathbf{C}\mathbf{w}_k^+) \mathbf{w}_k + \epsilon \frac{\partial V_d}{\partial \mathbf{w}_k} \\ & + \sum_{i=1}^M \tau_{ik} \mathbf{w}_i^+ + 2\alpha_k \mathbf{w}_k = \mathbf{0}, \end{aligned} \quad (2.12)$$

$$\mathbf{w}_k^+ \cdot \mathbf{w}_l = \delta_{kl}, \quad (2.13)$$

$$\mathbf{w}_k^2 = 1. \quad (2.14)$$

Because of the nonlinear dependence of  $\partial V_d / \partial \mathbf{w}_k^+$  and  $\partial V_d / \partial \mathbf{w}_k$ , Eqs. (2.11) and (2.12) cannot be solved directly. Therefore, a perturbational approach is chosen: the modes are expanded by power series in  $\epsilon$ ,

$$\mathbf{w}_i^+ = \mathbf{v}_i + \epsilon \mathbf{w}_i^{+(1)} + \epsilon^2 \mathbf{w}_i^{+(2)} + \dots, \quad (2.15)$$

$$\mathbf{w}_i = \mathbf{v}_i + \epsilon \mathbf{w}_i^{(1)} + \epsilon^2 \mathbf{w}_i^{(2)} + \dots, \quad (2.16)$$

as well as the Lagrangian parameters

$$\tau_{ij} = \tau_{ij}^0 + \epsilon \tau_{ij}^1 + \epsilon^2 \tau_{ij}^2 + \dots, \quad (2.17)$$

$$\alpha_i = \alpha_i^0 + \epsilon \alpha_i^1 + \epsilon^2 \alpha_i^2 + \dots \quad (2.18)$$

The eigenvalues  $\lambda_i$  are not expanded; the amplitudes  $x_i(t)$  remain the projections of the signal on the expanded modes  $\mathbf{w}_i^+$ . The expansion coefficients  $\mathbf{w}_i^{+(n)}$  and  $\mathbf{w}_i^{(n)}$  are built by superposition of the PCA modes  $\mathbf{v}_i$ ,

$$\mathbf{w}_i^{+(n)} = \sum_{j=1}^N c_{ij}^n \mathbf{v}_j, \quad \mathbf{w}_i^{(n)} = \sum_{j=1}^N d_{ij}^n \mathbf{v}_j. \quad (2.19)$$

Finally, the terms of Eqs. (2.11) and (2.12) can be sorted with respect to powers of  $\epsilon$  and evaluated separately.

#### I. Ground state

First we investigate the solution in perturbation order  $n = 0$ . With Eqs. (2.15) and (2.16) it follows that

$$\tau_{kl}^0 = 0, \quad \alpha_k^0 = 0. \quad (2.20)$$

Equation (2.12) leads to

$$\mathbf{C}\mathbf{v}_k = \lambda_k^0 \mathbf{v}_k, \quad (2.21)$$

$$\langle x_l(t) x_k(t) \rangle = \lambda_k \delta_{lk}, \quad (2.22)$$

with  $x_k(t)$  representing amplitudes of PCA. As constructed, the ground state corresponds to the PCA solution.

## 2. First-order perturbation

In the first-order perturbation, we have to deal with non-quadratic coefficient tensors  $\{c_{km}^n\}$  and  $\{d_{km}^n\}$  with  $1 \leq k \leq M$ ,  $1 \leq m \leq N$ .

First we investigate the case  $1 \leq k \leq M$  and  $1 \leq m \leq M$  and obtain from evaluating Eq. (2.6):

$$d_{km}^1 = -c_{mk}^1, \quad d_{kk}^1 = c_{kk}^1 = 0. \quad (2.23)$$

Equations (2.11) and (2.12) lead to Lagrangian parameters,

$$\alpha_k^1 = -\frac{\partial V_d}{\partial \mathbf{w}_k} \Big|_0 \cdot \mathbf{v}_k + \frac{\partial V_d}{\partial \mathbf{w}_k^+} \Big|_0 \cdot \mathbf{v}_k, \quad \tau_{kk}^1 = -\frac{\partial V_d}{\partial \mathbf{w}_k^+} \Big|_0 \cdot \mathbf{v}_k, \quad (2.24)$$

$$\tau_{km}^1 = \frac{\lambda_m^0}{(\lambda_k^0 - \lambda_m^0)} (\Delta_{mk} - \Delta_{km}) - \frac{\partial V_d}{\partial \mathbf{w}_k^+} \Big|_0 \cdot \mathbf{v}_m \quad \forall k \neq m, \quad (2.25)$$

and coefficients

$$c_{km}^1 = \frac{1}{(\lambda_k^0 - \lambda_m^0)^2} \left( \frac{1}{2} (\lambda_k^0 + \lambda_m^0) \Delta_{km} - \lambda_k^0 \Delta_{mk} \right) \quad \forall k \neq m \quad (2.26)$$

with

$$\Delta_{km} = \frac{\partial V_d}{\partial \mathbf{w}_m^+} \Big|_0 \cdot \mathbf{v}_k - \frac{\partial V_d}{\partial \mathbf{w}_k} \Big|_0 \cdot \mathbf{v}_m. \quad (2.27)$$

The terms  $\partial V_d / \partial \mathbf{w}_m^+ \Big|_0$  and  $\partial V_d / \partial \mathbf{w}_k \Big|_0$  represent partial derivatives with  $\mathbf{w}_k^+ = \mathbf{w}_k = \mathbf{v}_k$ .

In the case of  $1 \leq k \leq M$  and  $M < m \leq N$ , we get

$$c_{km}^1 = -\frac{1}{2\lambda_m^0(\lambda_k^0 - \lambda_m^0)} \left( \lambda_m^0 \frac{\partial V_d}{\partial \mathbf{w}_k} \Big|_0 \cdot \mathbf{v}_m + \lambda_k^0 \frac{\partial V_d}{\partial \mathbf{w}_k^+} \Big|_0 \cdot \mathbf{v}_m \right), \quad (2.28)$$

$$d_{km}^1 = -\frac{1}{2(\lambda_k^0 - \lambda_m^0)} \left( \frac{\partial V_d}{\partial \mathbf{w}_k} \Big|_0 \cdot \mathbf{v}_m + \frac{\partial V_d}{\partial \mathbf{w}_k^+} \Big|_0 \cdot \mathbf{v}_m \right), \quad (2.29)$$

and the Lagrangian parameters vanish.

In this paper we are dealing with low-dimensional dynamics; however, in the case of high-dimensional dynamics, the denominator  $(\lambda_k^0 - \lambda_m^0)$  may become small for high numbers  $k, l$  and, therefore, perturbation theory in degenerated states should be applied.

## C. Specification of $V_d$

So far we have not specified the cost function  $V_d$  considering dynamic interactions. Our choice relies on the PCA approach for the time derivative of the signal,

$$\sum_{i=1}^M \frac{\langle (\dot{\mathbf{q}} - \dot{x}_i \mathbf{w}_i)^2 \rangle}{\langle \dot{\mathbf{q}}^2 \rangle}. \quad (2.30)$$

Because of the assumed interactions, the time derivative of the amplitudes  $\dot{x}_i(t)$  can be described as a function of  $x_j$ ,

$$\dot{x}_i = f_i[x_j]. \quad (2.31)$$

Inserting this expression into Eq. (2.30), we obtain our definition of the cost function  $V_d$ :

$$V_d = \sum_{i=1}^M \frac{\langle (\dot{\mathbf{q}} - f_i \mathbf{w}_i)^2 \rangle}{\langle \dot{\mathbf{q}}^2 \rangle}. \quad (2.32)$$

The time derivative of  $\mathbf{q}(t)$  is calculated numerically and remains regular in the case of weak noise. Strong noise can lead to irregular numerical values, which need to be investigated separately.

As an ansatz for the function  $f_i[x_j]$  we choose a polynomial function,

$$f_i[x_j] = \sum_{j=1}^M \Gamma_{ij}^1 x_j + \sum_{j=1}^M \sum_{k=1}^j \Gamma_{ijk}^2 x_j x_k + \sum_{j=1}^M \sum_{k=1}^j \sum_{l=1}^k \Gamma_{ijk}^3 x_j x_k x_l, \quad (2.33)$$

since most of the generic cases can be modeled by such a set of differential equations. To abbreviate the notation, we can define a vector  $\{\xi_\alpha\}$  consisting of the powers of  $x_i$ ,

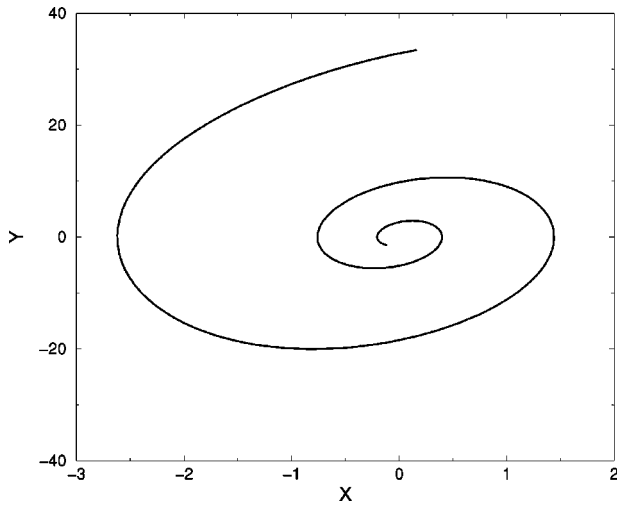
$$\{\xi_\alpha\} = \{x_1, x_2, \dots, x_M, x_1^2, x_1 x_2, \dots, x_M^2, x_1^3, x_1^2 x_1, \dots, x_M^3\}, \quad (2.34)$$

and summarize Eq. (2.33) to

$$f_i[x_j] = \sum_\alpha a_{i\alpha} \xi_\alpha. \quad (2.35)$$

The derivatives  $\partial V_d / \partial \mathbf{w}_k \Big|_0$  and  $\partial V_d / \partial \mathbf{w}_k^+ \Big|_0$  occurring in the expressions of coefficients  $c_{km}^1$  can now be evaluated to

$$\frac{\partial V_d}{\partial \mathbf{w}_k} \Big|_0 = \frac{2}{\langle \dot{\mathbf{q}}^2 \rangle} \sum_\alpha \left( \sum_\beta a_{k\beta}^0 M_{\alpha\beta} \mathbf{v}_k - \langle \xi_\alpha^0 \dot{\mathbf{q}} \rangle \right) a_{k\alpha}^0, \quad (2.36)$$

FIG. 1. Trajectory near a stable fixpoint in the  $x$ - $y$  plane.

$$\frac{\partial V_d}{\partial \mathbf{w}_k^+} \Big|_0 = \frac{2}{\langle \dot{\mathbf{q}}^2 \rangle} \sum_{i=1}^M \sum_{\beta} \left\langle \left( \sum_{\alpha} a_{i\alpha}^0 \xi_{\alpha}^0 - \dot{\mathbf{q}} \cdot \mathbf{v}_i \right) a_{i\beta}^0 \frac{\partial \xi_{\beta}^0}{\partial \mathbf{w}_k^+} \right\rangle. \quad (2.37)$$

Thereby, the polynomial coefficients  $a_{k\alpha}^0$  are obtained from Eq. (2.9) as

$$a_{k\alpha}^0 = \sum_{\beta} b_{k\beta} M_{\beta\alpha}^{-1} \quad (2.38)$$

with

$$b_{k\beta} = \langle (\mathbf{q} \cdot \mathbf{v}_k) \xi_{\beta}^0 \rangle, \quad M_{\alpha\beta} = \langle \xi_{\alpha}^0 \xi_{\beta}^0 \rangle, \quad (2.39)$$

and the derivatives of  $\xi_{\beta}^0$  are given as

$$\begin{aligned} \xi_{\beta}^0 &= x_r : \frac{\partial \xi_{\beta}^0}{\partial \mathbf{w}_k^+} = \mathbf{q} \delta_{rk}, \\ \xi_{\beta}^0 &= x_r x_s, \quad r \leq s: \frac{\partial \xi_{\beta}^0}{\partial \mathbf{w}_k^+} = \mathbf{q}(\delta_{kr} x_s + \delta_{ks} x_r), \quad (2.40) \\ \xi_{\beta}^0 &= x_r x_s x_t, \\ r \leq s \leq t: \frac{\partial \xi_{\beta}^0}{\partial \mathbf{w}_k^+} &= \mathbf{q}(\delta_{kr} x_s x_t + \delta_{ks} x_r x_t + \delta_{kt} x_r x_s). \end{aligned}$$

#### D. Dynamically relevant subspace

Assuming a  $M$ -mode interaction, the modes  $\mathbf{w}_k^+, \mathbf{w}_k$  given by Eqs. (2.15), (2.16), and (2.19) are calculated in first-order correction out of  $M$  PCA modes. In the  $N$ -dimensional signal space, there are  $\binom{N}{M}$  possible combinations to choose  $M$  out of  $N$  PCA modes as the ground state. Therefore, we obtain  $\binom{N}{M}$  alternatives improving the corresponding PCA modes. Since the cost function  $V_d$  measures dynamics representation, the best estimation of the relevant subspace is spanned by modes  $\mathbf{w}_k^+, \mathbf{w}_k$  with minimal value of  $V_d(\mathbf{w}_k^+, \mathbf{w}_k, \epsilon, M)$ , i.e., by investigation of  $\sum_{M=1}^N \binom{N}{M}$  branches, the best choice

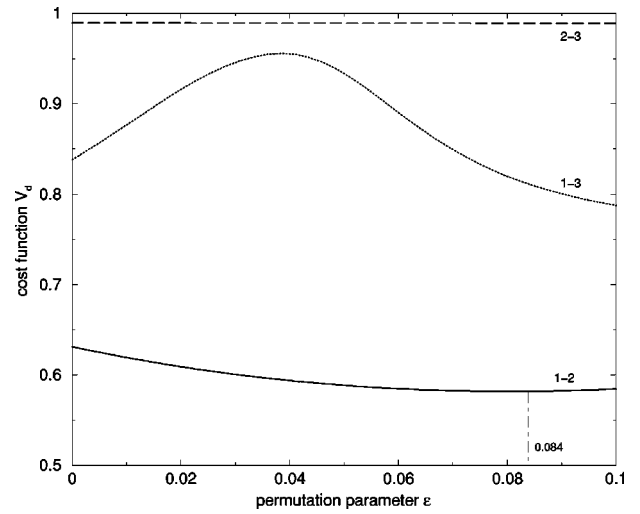


FIG. 2. Calculated cost function  $V_d(M=2, \epsilon)$  for the signal near a stable fixpoint. The plot shows a minimum with a combination of the first two PCA modes (solid line) at  $\epsilon_{min} = 0.084$ . The dotted line corresponds to the combination of PCA modes 1 and 3; the dashed line corresponds to the combination of PCA modes 2 and 3.

of spatial modes (in first-order perturbation theory) spanning the dynamically relevant subspace and the number of interacting modes is obtained.

### III. APPLICATIONS TO SIMULATED DATA SETS

To illustrate our approach we will present in the following the analysis of three simulated data sets consisting of two-mode interactions with one- and three-dimensional noise orthogonal to the signal, and a chaotic three-mode interaction, with additive noise nonorthogonal to the signal.

#### A. Noisy signal near a stable fixed point

First we assume a three-dimensional spatiotemporal signal near a two-dimensional stable fixed point and additive orthogonal noise,

$$\mathbf{q}(t) = x(t) \begin{pmatrix} 10 \\ 0 \\ 0 \end{pmatrix} + y(t) \begin{pmatrix} 0 \\ 1 \\ 0 \end{pmatrix} + z(t) \begin{pmatrix} 0 \\ 0 \\ 1 \end{pmatrix}. \quad (3.1)$$

The amplitudes  $x(t)$  and  $y(t)$  thereby obey the following set of differential equations:

$$\dot{x} = -y,$$

$$\dot{y} = ax + by + cx^2y, \quad (3.2)$$

where  $a = 0.06$ ,  $b = -0.1$ ,  $c = 0.01$ ,  $x(t_0) = 0.3$ , and  $y(t_0) = 0.7$ . The noise amplitude  $z(t)$  is modeled by

$$z(t) = \mathcal{N} \sum_{i=1}^{\eta} \rho_i(t) G_i(\mu_i, \sigma_i^2, t). \quad (3.3)$$

Here  $\rho_i \in [-0.5; 0.5]$  and  $\eta \in [0; T]$  denote random numbers,  $T$  denotes the number of time steps, and  $G_i(\mu_i, \sigma_i^2, t)$  represent temporal Gaussian functions with random means

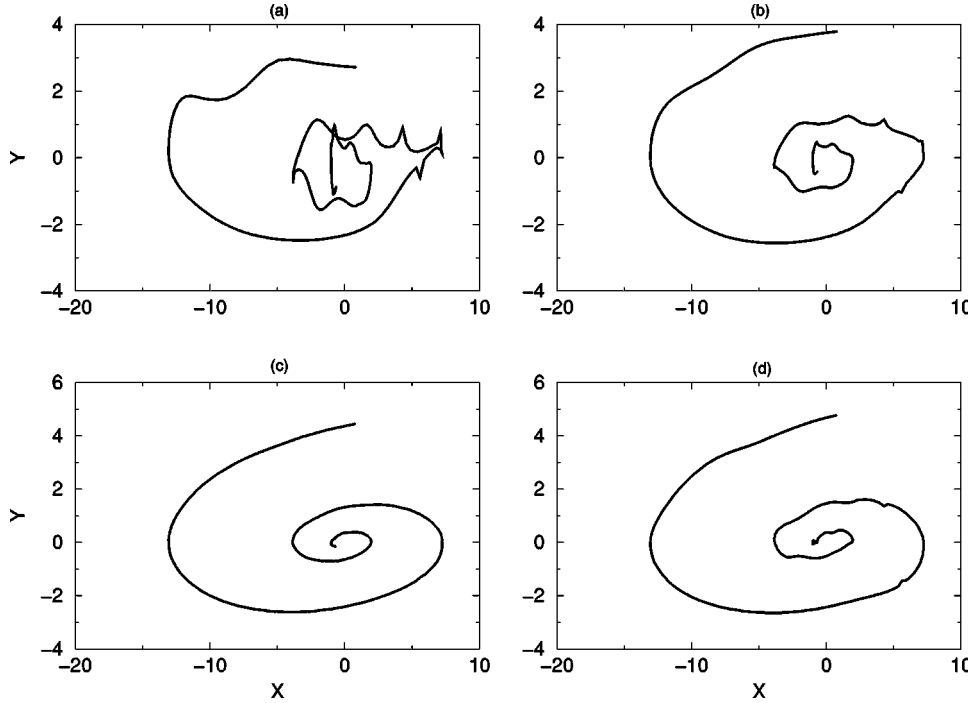


FIG. 3. Projected trajectories in the plane spanned by new modes  $\mathbf{w}_1^+, \mathbf{w}_2^+$ . The perturbation parameter  $\epsilon$  is varied from  $\epsilon = 0.000$  (a) over  $\epsilon = 0.052$  (b) and  $\epsilon = 0.084$  (c) to  $\epsilon = 0.100$  (d). We recognize the best projection in (c), as predicted by Fig. 2.

$\mu_i$  and random variances  $\sigma_i^2$ . The factor  $\mathcal{N}$  is introduced to scale  $z(t)$  to  $\langle z^2(t) \rangle = 1$ ,  $n$  in Eq. (3.1) allows tuning the signal-to-noise ratio.

Figure 1 shows the signal in  $x$ - $y$  plane: the trajectory cycles into a stable fixed point.

We investigate the three-dimensional ( $N=3$ ) data set considering  $M=2$  interacting modes. Thus, we deal with  $\binom{3}{2}$  branches of ground states: PCA modes 1 and 2, modes 1 and 3, and modes 2 and 3. The corresponding values of the cost function  $V_d$  are plotted in dependence of  $\epsilon$  in Fig. 2. The branch of PCA modes 1 and 2 represents the best dynamic fit; they capture most of the dynamics. From the figure we expect the best improvement of the PCA modes for a perturbation value of  $\epsilon_{min} = 0.084$ . This effect of the perturbation by the nonlinear cost function  $V_d$  is

illustrated in Fig. 3: the projections  $x(t) = \mathbf{w}_1^+ \cdot \mathbf{q}(t)$  and  $y(t) = \mathbf{w}_2^+ \cdot \mathbf{q}(t)$  are presented in the  $x$ - $y$  phase space for different values of  $\epsilon$ . In agreement with our expectations from Fig. 2, the best fit compared to Fig. 1 is obtained for  $\epsilon = \epsilon_{min}$ , with a dramatic improvement compared to the PCA solution ( $\epsilon = 0$ ).

The influence of the noisy part of the signal is investigated by varying the scaling  $n$  of the noise amplitude. Figure 4 presents the results by plots of  $V_d(M=2, \epsilon)$ . Increasing signal-noise ratio  $s/n$ , defined by  $s/n = \sqrt{\langle \mathbf{q}_{signal}^2 \rangle / \langle \mathbf{q}_{noise}^2 \rangle}$ , decreases the quality of the fit by increasing values of  $V_d$  and increases  $\epsilon_{min}$ , i.e., for higher noise levels the influence of our additional cost function  $V_d$  becomes more important, which is reflected by increasing values of  $\epsilon_{min}$ . For high noise levels the

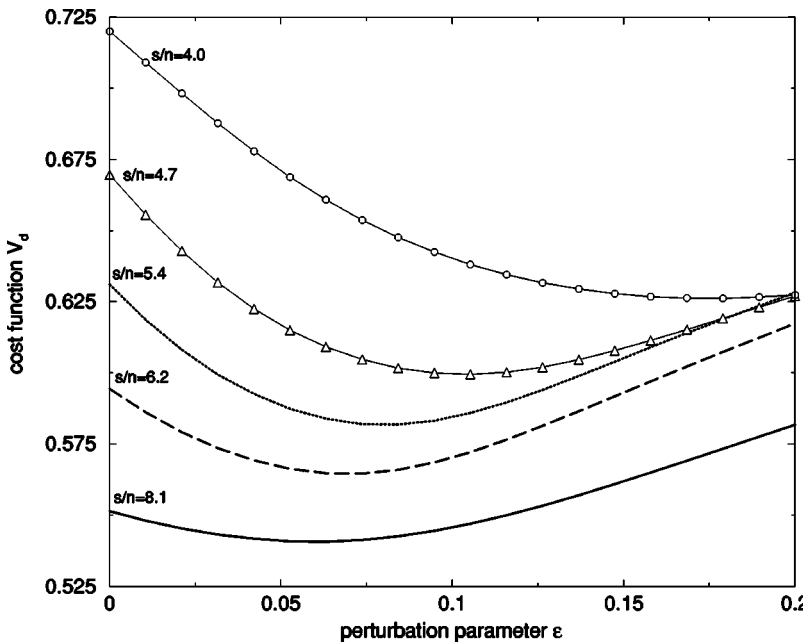


FIG. 4. Cost function  $V_d(\epsilon)$  for different values of the signal-to-noise ratio  $s/n$ .

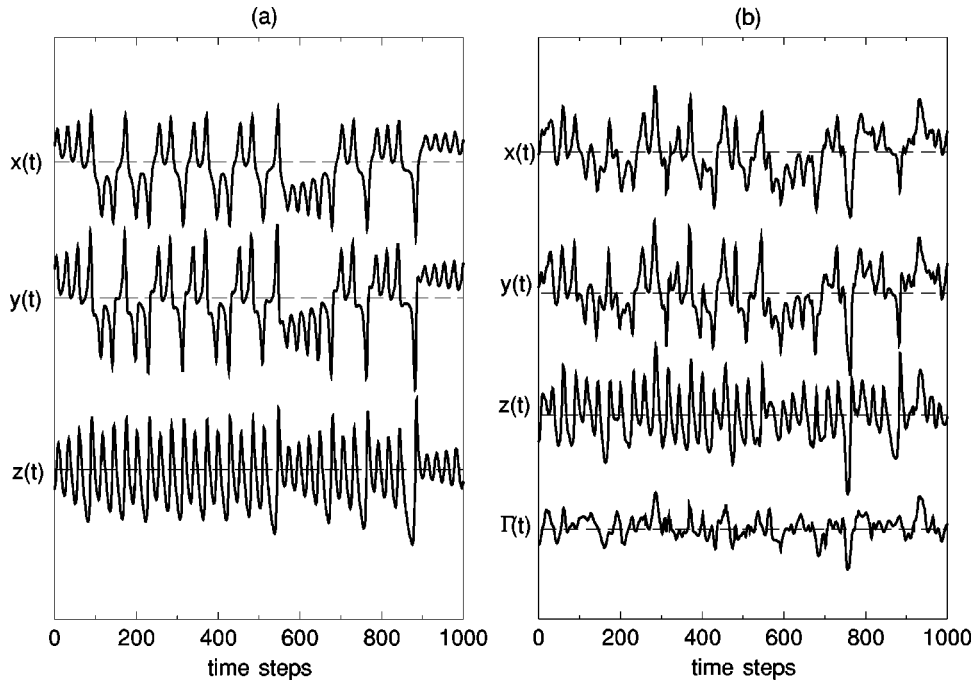


FIG. 5. Amplitudes of the Lorenz attractor without noise (a) and with nonorthogonal noise where a channel with pure noise is added in an additional dimension (b).

first-order perturbation may not be sufficient to capture most of the dynamics, higher-order perturbation terms may be considered.

The chaotic signal is modeled by the Lorenz equations,

$$\dot{x} = -\sigma(x - y) + \alpha(t), \quad (3.5)$$

### B. Noisy Lorenz attractor

The second example deals with a four-dimensional signal  $\mathbf{q}(t)$ , consisting of a three-mode chaotic signal  $[x(t), y(t), z(t)]$  and additive nonorthogonal noise,

$$\mathbf{q}(t) = x(t) \begin{pmatrix} 1 \\ 0 \\ 0 \\ 0 \end{pmatrix} + y(t) \begin{pmatrix} 0 \\ 1 \\ 0 \\ 0 \end{pmatrix} + z(t) \begin{pmatrix} 0 \\ 0 \\ 1 \\ 0 \end{pmatrix} + \Gamma(t) \begin{pmatrix} 1 \\ 1 \\ 1 \\ 1 \end{pmatrix}. \quad (3.4)$$

with  $\sigma = 10$ ,  $r = 2.8$ ,  $b = 8/3$ ,  $x(t_0) = 0.1$ ,  $y(t_0) = 0.2$ , and  $z(t_0) = 0.3$ .

The noise amplitude  $\Gamma(t)$  is modeled by

$$\Gamma(t) = \mathcal{N} \sum_{i=1}^{\eta} \rho_i(t) G_i(\mu_i, \sigma_i^2, t), \quad (3.6)$$

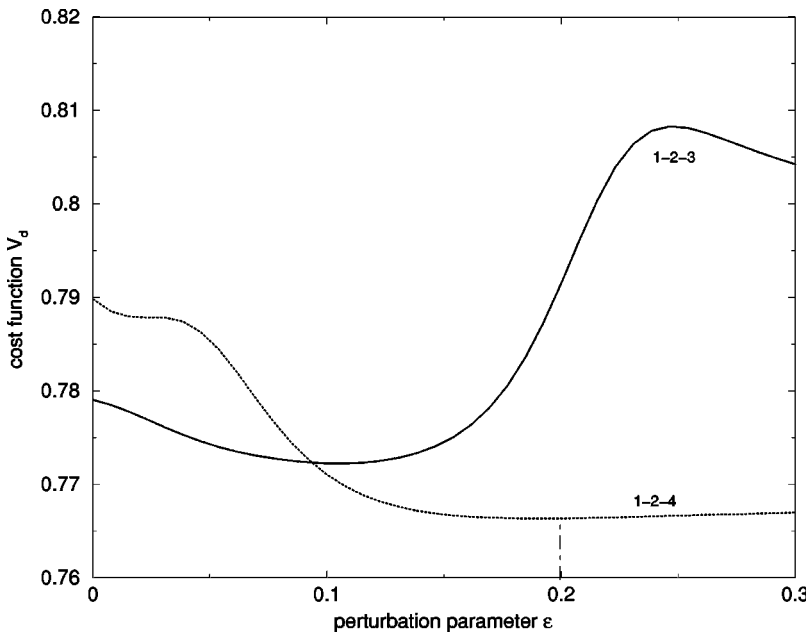


FIG. 6. Dynamic cost function for the Lorenz signal with respect to the perturbation parameter  $\epsilon$  with number of interacting modes  $M = 3$ . The deepest minimum is observed at  $\epsilon = 0.2$  with a combination of PCA modes 1, 2, and 4 (dotted line). The solid line corresponds to the combination of PCA modes 1, 2, and 3.

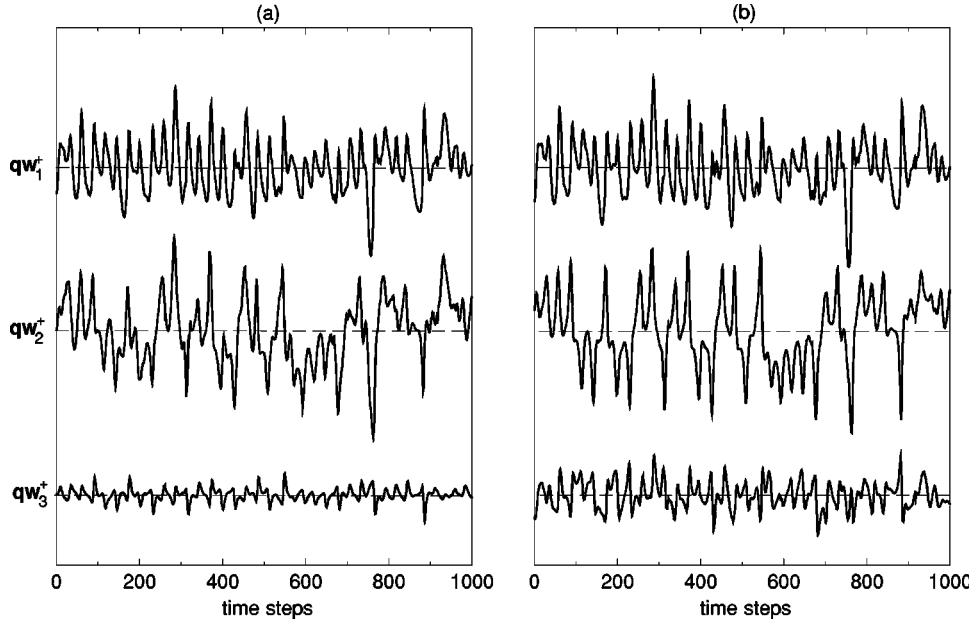


FIG. 7. Amplitudes  $\mathbf{q} \cdot \mathbf{w}_i^+$  obtained by the PCA fit (a) and our perturbational approach (b).

with the same abbreviations as in the example above;  $\alpha$  denotes correlated low noise. In Fig. 5(a) the amplitudes of the “pure” three-mode interaction without noise,  $x(t)$ ,  $y(t)$ , and  $z(t)$ , are presented. Fig. 5(b) shows the four-dimensional spatiotemporal signal  $\mathbf{q}(t)$ , as given by Eq. (3.4).

We investigate the simulated signal by assuming a three-mode interaction. Therefore, we deal with  $\binom{4}{3}$  PCA ground states and corresponding branches  $V_d$ . Figure 6 shows two branches (corrections based on PCA modes 1, 2, and 3, as well as based on modes 1, 2, and 4), the other two omitted branches are considerably higher. One observes that corrections of the 1–2–4 PCA ground state lead to better dynamics representation as the 1–2–3 combination, i.e., in the third PCA mode there is a higher contribution of the noisy part than of the deterministic part, whereas in the fourth PCA mode the deterministic part overbalances the noisy contribution. This behavior is corrected by our approach, in such a way that the separation of the deterministic—even though chaotic—part from the noisy part is improved.

Figure 7 presents the PCA amplitudes in comparison to the amplitudes obtained by our algorithm at  $\epsilon = \epsilon_{\min}$ .

A comparison of both results to the deterministic signal  $\mathbf{y}$  is shown in Fig. 8. Here we transformed the original deterministic signal part  $\mathbf{x} = (x, y, z)^t, \Gamma(t) = 0$  by a transformation matrix  $\mathbf{L}$  to neglect any scaling effects due to different orientations or scales of the compared signals.

$\mathbf{L}$  is determined by

$$\frac{\partial}{\partial L_{kl}} \langle [\mathbf{y}(t) - \mathbf{L}\mathbf{x}(t)]^2 \rangle = 0 \quad (3.7)$$

$$\rightarrow L_{kl} = \sum_j \langle y_k x_j \rangle \langle x_j x_l \rangle^{-1}. \quad (3.8)$$

The improvement obtained by our algorithm compared to the PCA approach can be clearly observed in Fig. 8.

### C. Estimation of the number of interacting modes

We simulate a five-dimensional signal  $\mathbf{q}(t) = (x(t), y(t), \Gamma_1(t), \Gamma_2(t), \Gamma_3(t))^T$  based on the two-mode interaction given by Eq. (3.2) and orthogonal noise given by normalized amplitudes,

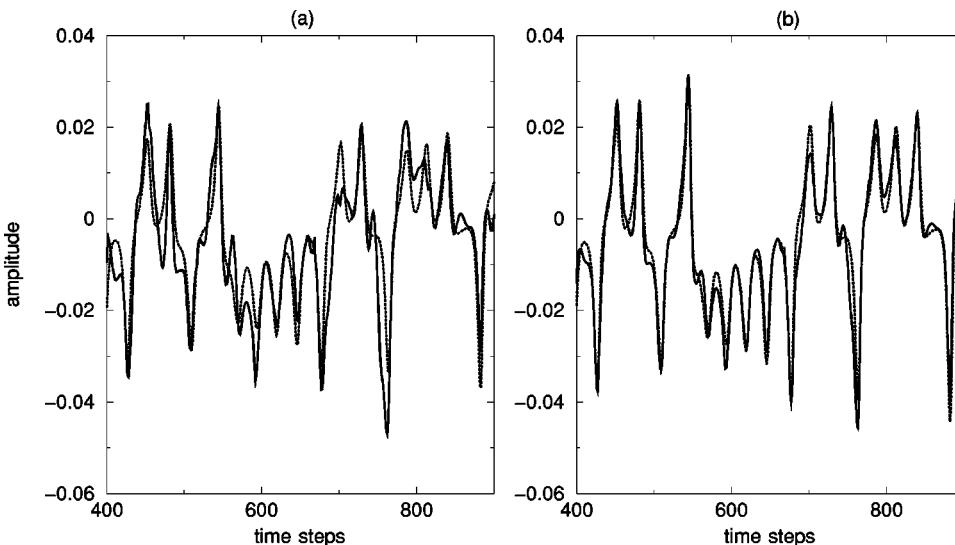


FIG. 8. A direct comparison of deterministic (dotted line) and reconstructed signals (solid line). The best PCA fit is shown in (a), the best perturbation fit in (b), where a better match can be recognized. We cut off parts of the time window to improve the comparison.

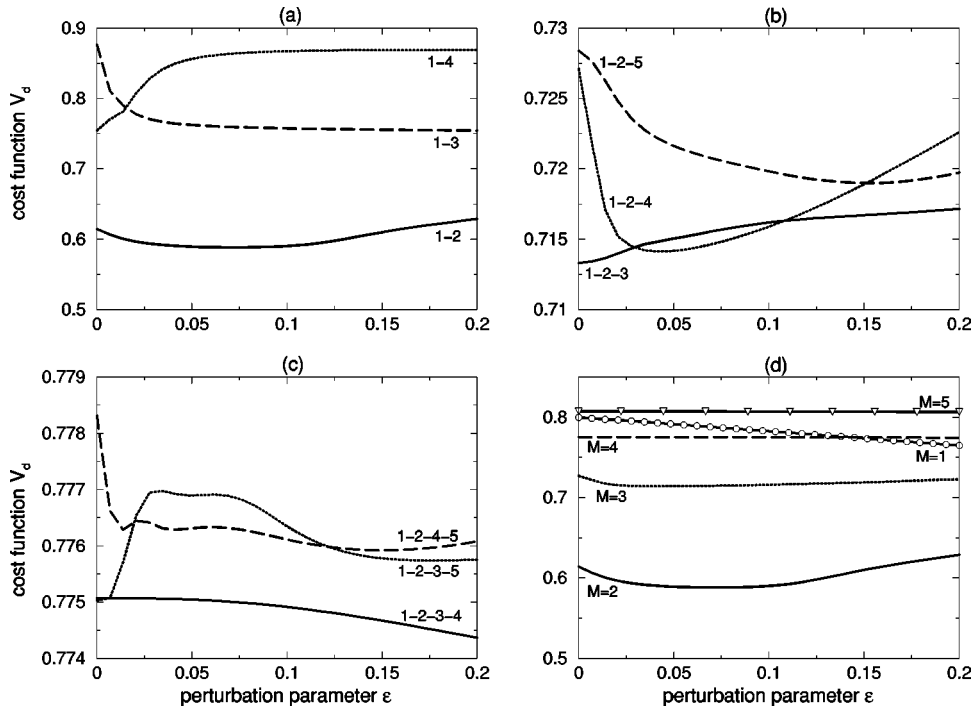


FIG. 9. Dynamic cost functions  $V_d(M, \epsilon)$  calculated for the noisy signal near a stable fixpoint. Only combinations  $m-n$  of PCA modes yielding the deepest minimum of  $V_d$  are shown for various numbers of interacting modes:  $M = 2$  in (a),  $M = 3$  in (b), and  $M = 4$  in (c). In (d), a comparison of the best fits of all  $M$  interacting modes is presented. We recognize an obvious best fit at  $M = 2$ . The cases where  $M = 1$  and  $M = 5$  were not plotted with different PCA ground states because of their visible irrelevance to the result in (d).

$$\Gamma_j(t) = \mathcal{N} \sum_{i=1}^n G_i(\mu_i, \sigma^2, t), \quad (3.9)$$

again with Gauss functions  $G_i(\mu_i, \sigma^2, t)$  with random means  $\mu_i$  and constant variances  $\sigma^2$ .

The applied dynamic fits are shown in Fig. 9 varying the assumed number of interacting modes and the different combinations of PCA modes as ground states. In the case of  $M = 2$  interacting modes [Fig. 9(a)] we recognize the deepest minimum with a combination of the first and second PCA mode. Dynamic fits with three and four interacting modes [Figs. 9(b) and 9(c)] show minima as well, but with higher values of  $V_d$ . A comparison of the best fits [Fig. 9(d)] presents the differences with respect to the number of interacting modes: the two-mode interaction is clearly detected.

Finally, we investigate the noisy Lorenz attractor (3.4). Dynamic fits are shown in Fig. 10 with varying number of interacting modes and PCA ground states. The investigation of two coupling modes leads to the 1-2 branch with minimal values; for three interacting modes the method neglects one noisy mode by combinations of the 1-2-4 PCA modes. A comparison of the best fits with  $M = 2$  and  $M = 3$  shows an interesting feature: though the Lorenz signal is determined by a three-dimensional set of differential equations our method detects a two-mode interaction: there is a deeper minimum for  $M = 2$ . This is due to the similarity of the two amplitudes  $x(t)$  and  $y(t)$  [compare Fig. 5(a)] and the resulting correlation dimension  $d_C = 2.06$  of the Lorenz attractor [13]. The small differences between these two amplitudes cannot be resolved by our method in the presence of noise. However, the detection of two interacting modes and the

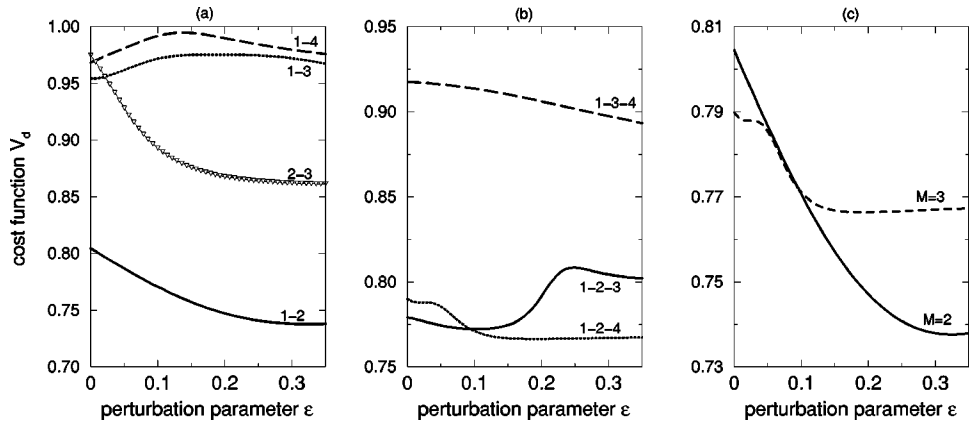


FIG. 10. Dynamic cost functions  $V_d(M, \epsilon)$  calculated for the noisy Lorenz attractor, at various PCA ground states  $m-n$ . We recognize a best fit with the first two PCA modes as ground state (solid line) at  $M=2$  (a) and a best fit with a PCA ground state built by modes 1, 2, and 4 (dotted line) at  $M=3$ , seen in (b). A comparison of the fits at  $M=2$  and  $M=3$  is presented in (c); a deeper minimum is found at  $M = 2$  (solid line), but the difference to the minimum at  $M = 3$  (dotted line) is quite small. PCA ground states at  $M = 1$  and  $M = 4$  are found at much higher values of  $V_d$  and are thus left out.

good correspondence to the exact solution (compare Fig. 8) is a considerable improvement compared to PCA approaches.

#### IV. CONCLUSIONS

We introduced a concept in nonlinear signal analysis for analyzing spatiotemporal signals. It considers signal dynamics beside a maximum signal representation. The idea mainly consists of an additional signal dynamics fit to a pure signal fit, interpreted as a perturbation of a PCA ground state. Introducing a biorthogonal basis, first-order perturbation leads to expansion coefficients of modes and polynoms of differential equations.

This approach improves PCA, since signal-noise separa-

tion is achieved even in the case of nonorthogonal signal and noise, and in the case of noise levels with larger contributions than signal contributions to the data. Finally, the number of interacting modes can be estimated by the presented algorithm.

The method is illustrated by examples of its application to simulated data sets: In the case of a noisy trajectory near a stable fixed point the dimensionality of the dynamics subspace is correctly estimated and a dramatic improvement compared to PCA is achieved. For a noisy three-dimensional chaotic signal embedded in a four-dimensional phase space the dimensionality is underestimated due to the fractal geometry of the attractor. However, the dominant structure of the attractor is reconstructed and noisy parts are separated.

The algorithm may represent a helpful tool for analyzing spatiotemporal signals in different fields of research.

- 
- [1] V. K. Jirsa and H. Haken, *Phys. Rev. Lett.* **77**, 962 (1996).
  - [2] A. V. Holden, M. Markus, and H. G. Othmer, *Nonlinear Wave Processes in Excitable Media* (Plenum Press, New York, 1991).
  - [3] G. Plaut and R. Vautard, *J. Atmos. Sci.* **51**, 210 (1994).
  - [4] M. Bestehorn, *Phys. Rev. Lett.* **76**, 46 (1996).
  - [5] R. Friedrich and C. Uhl, *Physica D* **98**, 171 (1996).
  - [6] A. Fuchs, J. A. S. Kelso, and H. Haken, *Int. J. Bifurcation Chaos Appl. Sci. Eng.* **2**, 917 (1992).
  - [7] C. Uhl, *Analysis of Neurophysiological Brain Functioning* (Springer-Verlag, Berlin, 1999).
  - [8] G. Berkooz, P. Holmes, and J. L. Lumley, *Annu. Rev. Fluid Mech.* **25**, 539 (1993).
  - [9] F. Kwasniok, *Phys. Rev. E* **55**, 5365 (1997).
  - [10] C. Uhl, R. Friedrich, and H. Haken, *Phys. Rev. E* **51**, 3890 (1995).
  - [11] D. R. Hartree, *Proc. Cambridge Philos. Soc.* **24**, 111 (1928).
  - [12] V. Fock, *Z. Phys.* **61**, 126 (1930); **62**, 795 (1930).
  - [13] H. G. Schuster, *Deterministic Chaos* (VCH-Verlag, Weinheim, 1995).

# Modeling of nonlinear Lévy processes by data analysis

Silke Siegert\* and Rudolf Friedrich

*Institute for Theoretical Physics 3, University of Stuttgart, Pfaffenwaldring 57, D-70550 Stuttgart, Germany*  
 (Received 28 August 2000; published 25 September 2001)

The paper presents a method to analyze time series of nonlinear Lévy processes. The Lévy stability index as well as the nonlinear deterministic and stochastic parts of the dynamics together with their uncertainties can be calculated numerically. As last step of the analysis the membership of the investigated system to the regarded class of dynamical systems is validated. For demonstration the algorithm is applied to artificially created time series with different Lévy indices.

DOI: 10.1103/PhysRevE.64.041107

PACS number(s): 05.40.Fb, 05.45.-a, 05.10.Gg

## I. INTRODUCTION

Normal diffusion under the influence of an external force field is often described by a Langevin equation for the  $d$ -dimensional stochastic variable  $\mathbf{X}(t)$  (see, e.g., [1–3])

$$d\mathbf{X}(t) = \mathbf{g}(\mathbf{X}(t), t)dt + \mathbf{h}(\mathbf{X}(t), t)d\mathbf{W}(t). \quad (1)$$

The trajectory of the stochastic variable  $\mathbf{X}(t)$  is determined by a deterministic part  $\mathbf{g}$  and a stochastic part  $\mathbf{h}$ .  $d\mathbf{W}$  stands for an infinitesimal Brownian motion, i.e., an infinitesimal Wiener process. The  $d$ -dimensional driving noise source  $\Gamma(t)$  of the Wiener process  $d\mathbf{W} = \Gamma(t)dt$  is a  $\delta$ -function correlated Gaussian white noise with

$$\langle \Gamma_i(t) \rangle = 0, \quad (2)$$

$$\langle \Gamma_i(t) \Gamma_j(t') \rangle = \delta_{ij} \delta(t - t'). \quad (3)$$

A lot of physical and biological systems can be described by models like Eq. (1) (see, e.g., [4,5]).

If the deterministic part  $\mathbf{g}$  and the stochastic part  $\mathbf{h}$  of Eq. (1) are not explicitly time dependent, one talks about a stationary process. In this case the probability density distribution  $w(\mathbf{x}, t) = w(\mathbf{x})$  in state space  $\{\mathbf{x}\}$  is stationary, i.e. it does not change in time.

For such stationary stochastic processes that can be described by a Langevin equation (1) with  $\mathbf{g} = \mathbf{g}(\mathbf{X}(t))$  and  $\mathbf{h} = \mathbf{h}(\mathbf{X}(t))$  a data-driven method to determine the deterministic and stochastic parts of the dynamics by data analysis directly from measured time series was proposed in Refs. [6,7].

The results of an application of the method to experimental data sets originating from physical, technical, and medical research was shown in Refs. [8–10].

The method can be extended to an application on nonstationary systems by a moving window technique. Then, the dynamics is assumed to be quasistationary within each window.

In this paper, the class of Langevin systems (1) will be extended to the bigger class of Langevin-like systems where the Gaussian white noise function is replaced by the more general Lévy noise (see, e.g., [11–13]). Stochastic Lévy pro-

cesses constitute an interesting generalization of normal diffusion processes (see, e.g., [14–16]). The typical length of Lévy flights grows according to

$$\langle |x| \rangle \sim t^{1/\alpha}, \quad \alpha \in (0, 2], \quad (4)$$

where  $\alpha=2$  stands for the behavior of normal diffusion. This property has made Lévy flights natural candidates for the description of enhanced diffusion.

The distribution of Lévy noise has a long-range algebraic tail corresponding to large but infrequent steps, so-called rare events. Therefore, rare events become more important in Lévy flights than in Brownian motion. The superdiffusive characteristics of Lévy flights have recently been used to model a broad variety of physical processes. Some examples are the description of anomalous transport in one dimension with absorbing boundary [16], the modeling of anomalous diffusion at liquid surfaces (so-called bulk-mediated surface diffusion), where the molecules execute Lévy walks on the surface [17], and the application of this modeling in the cases of porous glasses [18] and eye lenses [19]. Enhanced diffusion has been observed in systems of polymerlike breakable micelles [20]. Turbulence has been investigated under the point of view of Lévy flights [21]. Even the wandering of albatrosses has been modeled by the theory of Lévy flights [22].

Among the different theoretic frameworks connected with the description of anomalous diffusion are continuous random walk schemes [23,24], fractional diffusion equations [25,15], and generalized Langevin and Fokker-Planck equations [14].

In the following the theoretical model of a generalized Langevin equation as generalization of the Langevin equation for normal diffusion processes (1) will be used. For dynamic systems that are describable by such an evolution equation an analysis method will be presented that provides us with a direct data-driven tool to formulate model equations for the dynamics of the system.

## II. CONSIDERED SYSTEMS

Instead of Eq. (1) the following nonlinear Langevin-like differential equation for a stochastic vector  $\mathbf{X}(t)$  is assumed to describe the dynamics of the investigated systems (see, e.g., [11–13,15]):

\*Email address: silke@theo3.physik.uni-stuttgart.de

$$d\mathbf{X}(t) = \mathbf{g}(\mathbf{X}(t), t) + \mathbf{h}(\mathbf{X}(t), t) d\mathbf{L}_\alpha^{(\gamma, \beta, \mu)}. \quad (5)$$

$d\mathbf{L}_\alpha^{(\gamma, \beta, \mu)}$  stands for an infinitesimal  $d$ -dimensional  $\alpha$ -stable Lévy motion with

$$(d\mathbf{L}_\alpha^{(\gamma, \beta, \mu)})_i = (\mathbf{f}_\alpha^{(\gamma, \beta, \mu)})_i(t) dt, \quad (6)$$

where the  $d$  stochastically independently chosen components  $(\mathbf{f}_\alpha^{(\gamma, \beta, \mu)})_i(t)$  of the Lévy noise creating such a motion are characterized by the four parameters: Lévy stability  $\alpha \in (0, 2]$ , scale parameter  $\gamma \geq 0$ , skewness  $\beta \in [-1, 1]$ , and center  $\mu \in \mathbb{R}$ . For  $\alpha=2$ ,  $\gamma=0.5$ ,  $\beta=0$ , and  $\mu=0$  Eq. (5) is equal to the original Langevin equation (1). For decreasing  $\alpha$  the larger deviations of the realization become larger and more frequent. On the left side of Fig. 4 realizations of Lévy noise are shown for different values of  $\alpha$ .

For simplicity of the model

$$d\mathbf{X}(t) = \mathbf{g}(\mathbf{X}(t), t) + \tilde{\mathbf{h}}(\mathbf{X}(t), t) \widetilde{d\mathbf{L}}_\alpha^{(\gamma, \beta, \mu)} \quad (7)$$

with

$$\tilde{h}_{ij}(\mathbf{X}(t), t) = \tilde{h}_{ii}(\mathbf{X}(t), t) \delta_{ij}, \quad \tilde{h}_{ii} > 0, \quad (8)$$

$$\widetilde{d\mathbf{L}}_\alpha^{(\gamma, \beta, \mu)} = \widetilde{\mathbf{f}}_\alpha^{(\gamma, \beta, \mu)} dt \quad (9)$$

is considered instead of Eq. (5). Now, the  $d$  components  $(\widetilde{\mathbf{f}}_\alpha^{(\gamma, \beta, \mu)})_i$  of the introduced Lévy-noise creating the infinitesimal Lévy-motions  $(\widetilde{d\mathbf{L}}_\alpha^{(\gamma, \beta, \mu)})_i$  are no longer necessarily stochastically independent.

In general, Lévy noise is not defined by its probability density, but by its characteristic function. The probability density distribution exists and is continuous but, with some exceptions, it is not known in closed form. The characteristic function of each Lévy noise component, i.e. the Fourier transform of the probability density distribution  $p_\alpha^{(\gamma, \beta, \mu)}$  of each component, has the following form:

$$\begin{aligned} \langle e^{iqx} \rangle &= \int_{-\infty}^{\infty} p_\alpha^{(\gamma, \beta, \mu)}(x) e^{iqx} dx \\ &= \begin{cases} \exp \left\{ -\gamma|q|^\alpha \left( 1 - i\beta(\operatorname{sgn} q) \tan \frac{\pi\alpha}{2} \right) + i\mu q \right\} & \text{if } \alpha \neq 1, \\ \exp \left\{ -\gamma|q| \left( 1 + i\beta \frac{2}{\pi} (\operatorname{sgn} q) \ln|q| \right) + i\mu q \right\} & \text{if } \alpha = 1. \end{cases} \end{aligned} \quad (10)$$

It is the most general form of a characteristic function of a stable process. For  $(\beta=0, \mu=0)$  the probability density distribution is given by

$$p_\alpha^{(\gamma, \beta=0, \mu=0)}(x) = \frac{1}{\pi} \int_0^\infty \exp(-\gamma|q|^\alpha) \cos(qx) dq. \quad (11)$$

For the following considerations,  $\gamma=1$ ,  $\mu=0$  is set without loss of generality for the model equations (5) and (7). Besides,  $\beta=0$  is chosen. In this case, a series expansion of Eq. (11) valid for large arguments ( $|x| \gg 0$ ) is given by

$$\begin{aligned} p_\alpha^{(\gamma=1, \beta=0, \mu=0)}(|x|) &= -\frac{1}{\pi} \sum_{k=1}^n \frac{(-1)^k}{k!} \frac{\Gamma(\alpha k + 1)}{|x|^{\alpha k + 1}} \sin \left[ \frac{k\pi\alpha}{2} \right] \\ &\quad + R(|x|), \end{aligned} \quad (12)$$

where  $\Gamma(x)$  is the Euler  $\Gamma$  function and

$$R(|x|) = \mathcal{O}(|x|^{-\alpha(n+1)-1}). \quad (13)$$

From this expansion, an asymptotic approximation of a stable distribution of index  $\alpha$  for large values of  $|x|$  can be found as

$$p_\alpha^{(\gamma=1, \beta=0, \mu=0)}(|x|) \sim \frac{\Gamma(1+\alpha) \sin(\pi\alpha/2)}{\pi|x|^{1+\alpha}} \sim |x|^{-(1+\alpha)}. \quad (14)$$

The asymptotic behavior for large values of  $|x|$  is a power-law behavior. It results in a divergence of all moments  $\langle |x|^n \rangle$  with  $n \geq \alpha$  when  $\alpha < 2$ . In particular, all Lévy stable processes with  $\alpha < 2$  have infinite variance.

In the following, a method to determine the Lévy stability index  $\alpha$ , when  $\alpha \in (1, 2]$  and the deterministic and stochastic parts of a Langevin-like equation (7) directly from given time series will be presented. For the analysis the process has to be stationary, i.e., deterministic and stochastic parts are not explicitly time dependent. If instationary systems are investigated, a moving window technique has to be applied, i.e., the system is assumed to be stationary within one window and the time dependence of the functionals is estimated later on by taking together the results of the overlapping windows.

These considerations together with the considerations about the Lévy parameters above lead to the following class of model equations for the investigated considered dynamic systems:

$$\begin{aligned} d\mathbf{X}(t) &= \mathbf{g}(\mathbf{X}(t)) + \tilde{\mathbf{h}}(\mathbf{X}(t)) \widetilde{d\mathbf{L}}_\alpha^{(\gamma=1, \beta=0, \mu=0)}, \\ \alpha &\in (1, 2], \quad h_{ij} = h_{ii} \delta_{ij}. \end{aligned} \quad (15)$$

For small  $\tau$  the evolution equation (15) is integrated and iterated in an analogous way to the Euler method as:

$$\begin{aligned} \mathbf{X}(t+\tau) &\approx \mathbf{X}(t) + \mathbf{g}(\mathbf{X}(t)) \tau + \tilde{\mathbf{h}}(\mathbf{X}(t)) \tau^{1/\alpha} \mathbf{f}_\alpha^{(\gamma=1, \beta=0, \mu=0)}(t), \\ \tau &\ll 1. \end{aligned} \quad (16)$$

This iteration may be understood as definition of the differential equation (15) and will form the basis of the procedure described in the following.

### III. A METHOD FOR ANALYZING LÉVY-STOCHASTIC SYSTEMS

For the extracting of deterministic and stochastic parts from fluctuating data, first, it is assumed that the underlying dynamics can be described by an iteration like Eq. (16). In the end, after all analysis results are found, this assumption can be verified.

Because of  $\beta=\mu=0$  the function  $\mathbf{g}(\mathbf{x})$  in state space  $\{\mathbf{x}\}$  (i.e. the space  $\{\mathbf{x}\}$  of all values  $\mathbf{x}$  that can be taken by the stochastic variable  $\mathbf{X}(t)$ ) can be expressed as conditional average according to

$$\mathbf{g}(\mathbf{x}) = \lim_{\tau \rightarrow 0} \frac{1}{\tau} \langle \mathbf{X}(t+\tau) - \mathbf{x} \rangle|_{\mathbf{X}(t)=\mathbf{x}} = \lim_{\tau \rightarrow 0} \frac{1}{\tau} \mathbf{T}^{(1)}(\mathbf{x}, \tau) \quad (17)$$

with

$$\mathbf{T}^{(1)}(\mathbf{x}, \tau) := \langle \mathbf{X}(t+\tau) - \mathbf{x} \rangle|_{\mathbf{X}(t)=\mathbf{x}}. \quad (18)$$

If stationarity is given, what has been assumed, the deterministic and stochastic functions  $\mathbf{g}$  and  $\tilde{\mathbf{h}}$  are not explicitly time dependent. So, the ensemble average  $\mathbf{T}^{(1)}$  can be estimated as conditional temporal average over the whole time series  $\mathbf{X}(t_n)$ . For this, the state space of the process is discretized. The condition  $\mathbf{X}(t)=\mathbf{x}$  is fulfilled if only pairs  $\mathbf{X}(t_n+\tau), \mathbf{X}(t_n)$  with  $\mathbf{X}(t_n)=\mathbf{x}$  within some limits  $\Delta\mathbf{x}$ , i.e. with  $\mathbf{X}(t_n)$  and  $\mathbf{x}$  lying within the same bin of the discretized state space, are taken into consideration. In the following this is expressed by the condition  $\mathbf{X}(t_n)=\mathbf{x} \pm \Delta\mathbf{x}$ . The conditional average  $\mathbf{T}^{(1)}$  has to be calculated for every  $\mathbf{x}$  separately.  $N$  shall be the number of data pairs for a certain  $\mathbf{x}$  that fulfill the condition. Then,  $\mathbf{T}^{(1)}$  can be estimated as

$$\begin{aligned} \mathbf{T}^{(1)}(\mathbf{x}, \tau) &\approx \mathbf{T}_E^{(1)(N)}(\mathbf{x}, \tau) \\ &:= \frac{1}{N} \sum_{n=1}^N (\mathbf{X}(t_n+\tau) - \mathbf{X}(t_n)) \Big|_{\mathbf{X}(t_n)=\mathbf{x} \pm \Delta\mathbf{x}}. \end{aligned} \quad (19)$$

The subscript  $E$  will be added whenever an estimation value for an observable is introduced. Generally,  $N$  is different for every point  $\mathbf{x}$  and has to be large for a good result (see uncertainty discussion in next section). To be reminded that  $N$  has an influence on the estimated value even if it is not treated as direct functional dependence, the index  $(N)$  is added as superscript to the estimation value.

If  $\mathbf{T}_E^{(1)(N)}$  is calculated for different (but small) values of  $\tau$  like e.g.  $\Delta t_{\text{samp}}, 2\Delta t_{\text{samp}}, 3\Delta t_{\text{samp}}, \dots$ , where  $\Delta t_{\text{samp}}$  is the sampling time of the time series, the limit  $\tau \rightarrow 0$  of  $\mathbf{T}^{(1)}/\tau$  according to relationship (17) can be found by extrapolation. By this way, an estimation  $\mathbf{g}_E^{(N)}(\mathbf{x})$  for the deterministic part  $\mathbf{g}(\mathbf{x})$  of the dynamics can be calculated.

To estimate the stochastic part  $\tilde{\mathbf{h}}(\mathbf{x})$ , the Lévy index  $\alpha$  has to be determined, first. Therefore, the following conditional average is considered and approximated for small  $\tau$  as

$$\begin{aligned} &\langle |X_i(t+\tau) - x_i - g_i(\mathbf{x})\tau| \rangle|_{\mathbf{X}(t)=\mathbf{x}} \\ &= T_i^{(2)}(\mathbf{x}, \tau) \approx \tilde{h}_{ii}(\mathbf{x}) \tau^{1/\alpha} \int_{-\infty}^{\infty} |x'| p_{\alpha}^{(\gamma=1, \beta=0, \mu=0)}(x') dx' \\ &= \tilde{h}_{ii}(\mathbf{x}) \tau^{1/\alpha} F(\alpha), \quad \tau \ll 1, \end{aligned} \quad (20)$$

respectively,

$$\ln[T_i^{(2)}(\mathbf{x}, \tau)] \approx \ln[\tilde{h}_{ii}(\mathbf{x})F(\alpha)] + \frac{1}{\alpha} \ln(\tau), \quad \tau \ll 1, \quad (21)$$

with

$$T_i^{(2)}(\mathbf{x}, \tau) := \langle |X_i(t+\tau) - x_i - g_i(\mathbf{x})\tau| \rangle|_{\mathbf{X}(t)=\mathbf{x}}, \quad (22)$$

$$F(\alpha) := \int_{-\infty}^{\infty} |x'| p_{\alpha}^{(\gamma=1, \beta=0, \mu=0)}(x') dx'. \quad (23)$$

For  $\mathbf{g}(\mathbf{x})$  being known in form of the estimation  $\mathbf{g}_E^{(N)}(\mathbf{x})$  in the meantime, the conditional averages  $T_i^{(2)}(\mathbf{x}, \tau)$  can be estimated as

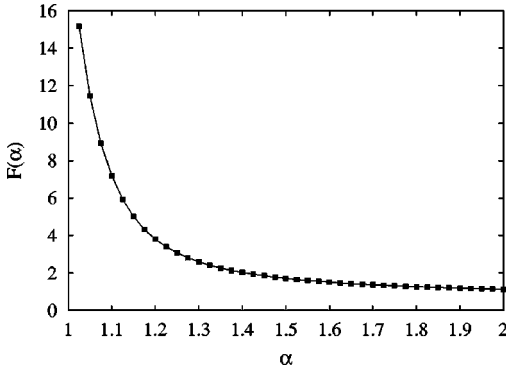
$$\begin{aligned} &T_i^{(2)}(\mathbf{x}, \tau) \\ &\approx T_{iE}^{(2)(N)}(\mathbf{x}, \tau) \\ &:= \frac{1}{N} \sum_{n=1}^N |X_i(t_n+\tau) - X_i(t_n) - g_{iE}^{(N)}(\mathbf{x})\tau| \Big|_{\mathbf{X}(t_n)=\mathbf{x} \pm \Delta\mathbf{x}}. \end{aligned} \quad (24)$$

The proceeding is analogous to the calculations described above.

When  $T_i^{(2)}$  is calculated for several small values of  $\tau$  (e.g.  $\Delta t_{\text{samp}}, 2\Delta t_{\text{samp}}, 3\Delta t_{\text{samp}}, \dots$ ) and is plotted for fixed  $\mathbf{x}$  and  $i$  in a ln-ln-plot over  $\tau$ ,  $\alpha$  can be determined as inverse slope of a fitted straight line. In theory, for each  $\mathbf{x}$  and  $i$  the same value for  $\alpha$  should be received by this method. In praxis, errors because of finite time series, finite discretization of state space, extrapolation, and measurement (see Sec. IV) can be minimized by taking the mean of all values for  $\alpha$ , that have been calculated for the different  $\mathbf{x}$  and  $i$ . This average value  $\alpha_E$  is used as an estimate for the Lévy index. The standard deviation of this distribution can be taken as uncertainty  $\Delta\alpha_E$ .

Now, expression  $F(\alpha)$  can be estimated numerically according to Eq. (23) by simulating a Lévy motion with  $(\alpha = \alpha_E, \gamma=1, \beta=0, \mu=0)$  and taking the average of the absolute value of the realization. The realization  $f_{\alpha}^{(\gamma=1, \beta=0, \mu=0)}$  of the Lévy noise can be constructed as follows [26,27]: A realization  $r$  of a uniformly distributed random variable in the interval  $[-\pi/2, \pi/2]$  is taken and, independently, a realization  $v$  of an exponential random variable with mean 1. Then

$$f_{\alpha}^{(\gamma=1, \beta=0, \mu=0)} = \frac{\sin(\alpha r)}{(\cos r)^{1/\alpha}} \left( \frac{\cos[(1-\alpha)r]}{v} \right)^{(1-\alpha)/\alpha}. \quad (25)$$

FIG. 1. Numerically determined integral  $F(\alpha)$  and the derivative  $F'(\alpha) = dF(\alpha)/d\alpha$  over  $\alpha$ .

The numerical result for  $F(\alpha)$  in the range  $\alpha \in (1.0, 2.0]$  is presented on the left side of Fig. 1.

The stochastic part  $\tilde{h}(\mathbf{x})$  is given by

$$\begin{aligned}\tilde{h}_{ii}(\mathbf{x}) &= \lim_{\tau \rightarrow 0} \frac{\langle |X_i(t+\tau) - x_i - g_i(\mathbf{x})\tau| \rangle|_{\mathbf{X}(t)=\mathbf{x}}}{\tau^{1/\alpha} F(\alpha)} \\ &= \lim_{\tau \rightarrow 0} \frac{T_i^{(2)}(\mathbf{x}, \tau)}{\tau^{1/\alpha} F(\alpha)}.\end{aligned}\quad (26)$$

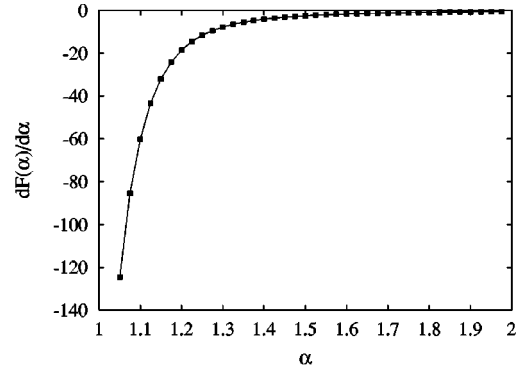
It can be estimated as

$$\tilde{h}_{iiE}^{(N, \alpha_E)}(\mathbf{x}) = \lim_{\tau \rightarrow 0} \frac{T_{iE}^{(2)(N)}(\mathbf{x}, \tau)}{\tau^{1/\alpha_E} F(\alpha_E)}. \quad (27)$$

Additionally to  $N$ , the estimated Lévy index  $\alpha_E$  has been added as superscript to remind on a possible uncertainty propagation caused by this estimation value. The procedure concerning the calculation of the limit  $\tau \rightarrow 0$  is analogous to the determination of the deterministic part.

#### IV. UNCERTAINTIES OF THE RESULTS

Up to this point of the analysis just the uncertainty of the Lévy index  $\alpha$  has been concerned. But for experimentally as well as for numerically set up values error bars are of great importance for a correct interpretation and further application of the results. In addition to this quite general justification for uncertainty discussions, for the presented algorithm error bars have an additional importance. The necessary extrapolations to  $\tau=0$  can be calculated with greater accuracy if explicit uncertainties for the  $\tau$ -dependent values are known compared with an extrapolation under the assumption of unit standard deviations. The analysis results calculated so far for the Lévy index  $\alpha$ , the deterministic part  $\mathbf{g}(\mathbf{x})$  and the stochastic part  $\tilde{\mathbf{h}}(\mathbf{x})$  provide us with first (already very good) estimations for the real observables. With the help of these values uncertainties can be calculated as will be described below. Afterwards the extrapolations to  $\tau=0$  can be determined again, this time under the use of real error bars instead of unit standard deviations. So, new estimations for  $\alpha$ ,  $\mathbf{g}(\mathbf{x})$  and  $\tilde{\mathbf{h}}(\mathbf{x})$  can be calculated. They do not differ very much from the first estimations, anyhow. This procedure may be



run a few times, calculating new error bars under the use of the estimations, determining new estimations with the help of the error bars. One will recognize that the procedure is convergent after at most one or two runs. In the following, the analytic expressions for the uncertainties of interest will be presented.

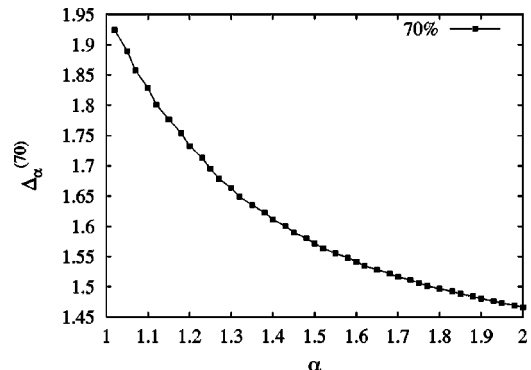
The term  $\mathbf{T}_E^{(1)(N)}(\mathbf{x}, \tau)$  is calculated as sum of  $N$  independently identically Lévy distributed stochastic variables. Therefore,  $\mathbf{T}_E^{(1)(N)}(\mathbf{x}, \tau)$  itself is a stochastic variable, which is also Lévy distributed.

$$\begin{aligned}\frac{1}{\tau} \mathbf{T}_E^{(1)(N)}(\mathbf{x}, \tau) &= \frac{1}{\tau} \frac{1}{N} \sum_{n=1}^N [\mathbf{X}(t_n + \tau) - \mathbf{X}(t_n)]|_{\mathbf{X}(t_n) = \mathbf{x} \pm \Delta \mathbf{x}} \\ &\approx \mathbf{g}(\mathbf{x}) + \tilde{\mathbf{h}}(\mathbf{x}) \frac{1}{\tau^{1-1/\alpha}} \mathbf{f}_\alpha^{(\gamma=1/N^{\alpha-1}, \beta=0, \mu=0)} \\ &= \mathbf{g}(\mathbf{x}) + \tilde{\mathbf{h}}(\mathbf{x}) \frac{1}{(\tau N)^{1-1/\alpha}} \mathbf{f}_\alpha^{(\gamma=1, \beta=0, \mu=0)}.\end{aligned}\quad (28)$$

As uncertainty of a Lévy distributed stochastic variable  $Z = f_\alpha^{(\gamma=1, \beta=0, \mu=0)}$  the width  $\Delta_\alpha^{(70)}$  is introduced with

$$\int_{-\Delta_\alpha^{(70)}}^{\Delta_\alpha^{(70)}} p(z) dz \geq 0.7. \quad (29)$$

$\Delta_\alpha^{(70)}$  can be calculated numerically and is illustrated in Fig. 2.

FIG. 2. Numerically determined uncertainty  $\Delta_\alpha^{(70)}$ , defined by Eq. (29), over  $\alpha$ .

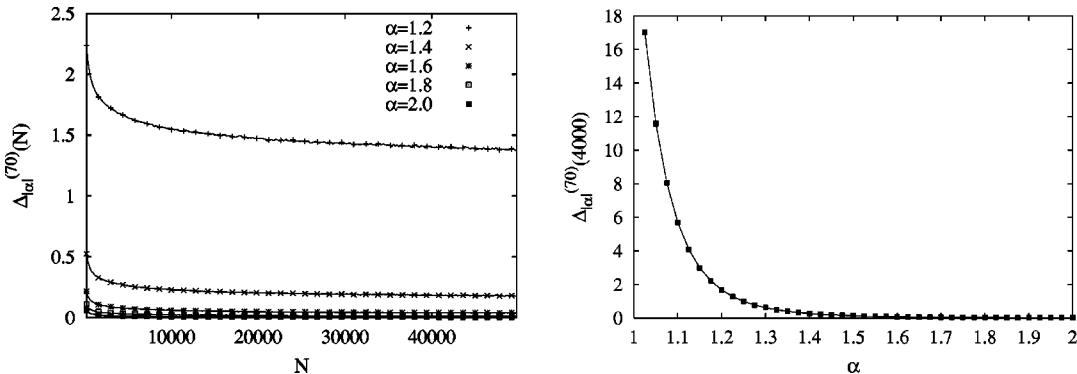


FIG. 3. Numerically determined uncertainty  $\Delta_{|\alpha|}^{(70)}$ , defined by Eq. (32), over  $N$  for fixed  $\alpha$  (left side) and over  $\alpha$  for fixed  $N=4000$  (right side).

With the help of definition (29) the uncertainty of  $1/\tau T_E^{(1)(N)}(\mathbf{x}, \tau)$  can be expressed as

$$\frac{1}{\tau} \Delta T_E^{(1)(N)}(\mathbf{x}, \tau) = \tilde{\mathbf{h}}_E^{(N)}(\mathbf{x}) \frac{1}{(\tau N)^{1-1/\alpha_E}} \Delta_{\alpha_E}^{(70)}. \quad (30)$$

The results together with their uncertainty limits have a confidence of 70%. This width of the confidence interval is used in the whole contribution whenever a standard deviation is not applicable. Now, the confidence of  $\mathbf{g}_E^{(N)}(\mathbf{x})$  can be determined by extrapolation of  $1/\tau T_E^{(1)(N)}(\mathbf{x}, \tau)$  to  $\tau=0$  under consideration of the error bars.

The influence of the uncertainty  $\Delta \mathbf{x}$  of  $\mathbf{x}$  will not be considered explicitly in the following. It is taken into account as uncertainty in phase space and has the value of the discretization width. If differentiable functions for  $\mathbf{g}(\mathbf{x})$  and  $\tilde{\mathbf{h}}(\mathbf{x})$  are assumed, the estimated values in every bin are always within the interval from the minimum to the maximum of the actual, correct function within this bin. So, the estimated values for deterministic and stochastic parts in each bin will represent the correct value of the observables at least somewhere within the considered bin.

The uncertainty of  $T_{iE}^{(2)(N)}(\mathbf{x}, \tau)$  can be found in an equivalent way to the determination of the uncertainty of  $T_E^{(1)(N)}$ . The only difficulty in this case is the fact that  $T_{iE}^{(2)(N)}$  is not a sum of independently identically Lévy distributed stochastic variables, but the sum of absolute values of such variables. Therefore,  $T_{iE}^{(2)(N)}$  itself is of course again a stochastic variable, but in general not Lévy distributed anymore.

$$\begin{aligned} T_{iE}^{(2)(N)}(\mathbf{x}, \tau) &= \frac{1}{N} \sum_{n=1}^N |[X_i(t_n + \tau) - X_i(t_n) - g_i(\mathbf{x})\tau]| \Big|_{\mathbf{X}(t_n) = \mathbf{x} \pm \Delta \mathbf{x}} \\ &\stackrel{\tau \ll 1}{\approx} \tilde{h}_{ii}(\mathbf{x}) \tau^{1/\alpha} \frac{1}{N} \sum_{n=1}^N |f_{\alpha}^{(\gamma=1, \beta=0, \mu=0)}(t_n)| \\ &\rightarrow \tilde{h}_{ii}(\mathbf{x}) \tau^{1/\alpha} F(\alpha). \end{aligned} \quad (31)$$

The uncertainty of  $T_{iE}^{(2)(N)}$  can be expressed with the help of a new defined width  $\Delta_{|\alpha|}^{(70)}(N)$ : As uncertainty of a stochastic variable  $Z = 1/N \sum_{n=1}^N |f_{\alpha}^{(\gamma=1, \beta=0, \mu=0)}|$  the width  $\Delta_{|\alpha|}^{(70)}(N)$  is defined by

$$\int_{F(\alpha) - \Delta_{|\alpha|}^{(70)}(N)}^{F(\alpha) + \Delta_{|\alpha|}^{(70)}(N)} p(z) dz \geq 0.7. \quad (32)$$

$\Delta_{|\alpha|}^{(70)}(N)$  can be determined numerically by simulating Lévy processes as described above, calculating the stochastic variable  $Z$  with fixed  $N$  for statistically representative times and estimating  $\Delta_{|\alpha|}^{(70)}(N)$  for the distribution. On the left side of Fig. 3 the results for  $\Delta_{|\alpha|}^{(70)}(N)$  are plotted over  $N$  for different values of  $\alpha$ . The right side of the figure illustrates the dependence of the width on  $\alpha$  for fixed  $N=4000$ .

Now, the uncertainty of  $T_{iE}^{(2)}$  can be calculated as

$$\Delta(T_{iE}^{(2)(N)}(\mathbf{x}, \tau)) = \tilde{h}_{ii}^{(N, \alpha_E)}(\mathbf{x}) \tau^{1/\alpha_E} \Delta_{\alpha_E}^{(70)}(N), \quad (33)$$

respectively,

$$\begin{aligned} \Delta(\ln[T_{iE}^{(2)(N)}(\mathbf{x}, \tau)]) &= \frac{1}{T_{iE}^{(2)(N)}(\mathbf{x}, \tau)} \Delta T_{iE}^{(2)(N)}(\mathbf{x}, \tau) \\ &= \frac{1}{T_{iE}^{(2)(N)}(\mathbf{x}, \tau)} \tilde{h}_{ii}^{(N, \alpha_E)}(\mathbf{x}) \tau^{1/\alpha_E} \Delta_{\alpha_E}^{(70)}(N). \end{aligned} \quad (34)$$

These uncertainty intervals can be used in the determination of the Lévy index  $\alpha$  when a straight line is fitted to the data points. The determination of the error of  $\alpha_E$  itself has already been discussed above. It is taken as the standard deviation of all single values determined for different  $\mathbf{x}$  and  $i$ .

As the last step, the uncertainty of  $\tilde{h}_{ii}$  has to be discussed.

$$\tilde{h}_{ii}^{(N, \alpha_E)}(\mathbf{x}) = \lim_{\tau \rightarrow 0} \frac{T_{iE}^{(2)(N)}(\mathbf{x}, \tau)}{\tau^{1/\alpha_E} F(\alpha_E)} = \lim_{\tau \rightarrow 0} T_{iE}^{(3)(N, \alpha_E)}(\mathbf{x}, \tau) \quad (35)$$

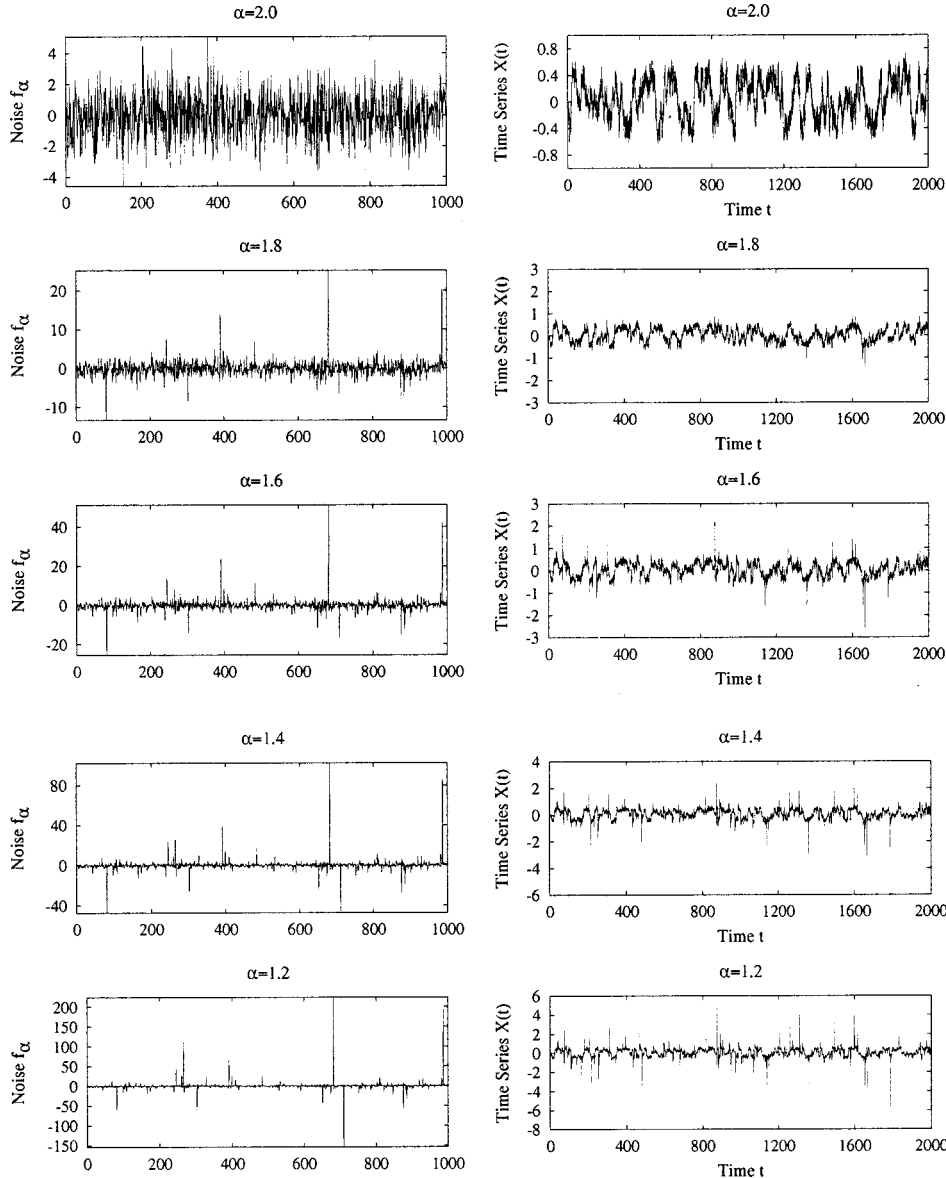


FIG. 4. Realizations of Lévy noise for different values of the Lévy index  $\alpha$  and subsequences of the affiliated integrated nonlinear Lévy motion according to the relations (40)–(42).

$$T_{iE}^{(3)(N,\alpha_E)}(\mathbf{x},\tau) := \frac{T_{iE}^{(2)(N)}(\mathbf{x},\tau)}{\tau^{1/\alpha_E} F(\alpha_E)}. \quad (36)$$

Errors of this estimation are caused by the uncertainty of  $T_{iE}^{(2)(N)}$ , which is primarily originated in the finite number  $N$  of relevant data points for every bin  $\mathbf{x}[X(t_n) = \mathbf{x} \pm \Delta \mathbf{x} \ \forall n]$ , and by the uncertainty of  $\alpha_E$  which has to be inserted in the formulas (35) and (36). The total uncertainty of  $T_{iE}^{(3)(N,\alpha_E)}$  can be expressed under consideration of the law of error propagation as

$$\begin{aligned} \Delta(T_{iE}^{(3)(N,\alpha_E)}(\mathbf{x},\tau)) &= \frac{\Delta T_{iE}^{(2)(N)}(\mathbf{x},\tau)}{\tau^{1/\alpha_E} F(\alpha_E)} + \frac{T_{iE}^{(2)(N)}(\mathbf{x},\tau)}{\tau^{2/\alpha_E} F^2(\alpha_E)} \\ &\times \left( \left| F'(\alpha_E) \tau^{1/\alpha_E} - \tau^{1/\alpha_E} \ln \tau \frac{F(\alpha_E)}{\alpha_E^2} \right| \right) \Delta \alpha_E \end{aligned}$$

$$\begin{aligned} &= \frac{\tilde{h}_{iiE}^{(N,\alpha_E)}(\mathbf{x}) \Delta_{|\alpha_E|}^{(70)}(N)}{F(\alpha_E)} + \frac{T_{iE}^{(2)(N)}(\mathbf{x},\tau)}{\tau^{1/\alpha_E} F(\alpha_E)} \\ &\times \left( \frac{F'(\alpha_E)}{F(\alpha_E)} - \frac{\ln \tau}{\alpha_E^2} \right) \Delta \alpha_E. \end{aligned} \quad (37)$$

The numerical results for the derivative  $F'(\alpha)$  are illustrated on the right side of Fig. 1.

## V. VALIDATION OF THE ASSUMPTIONS

The only assumption concerning the investigated system that has been made is the pure describability of the dynamics by an evolution equation like Eq. (16). No further ansatz has been taken into account, no further knowledge about the system of interest is necessary. Now, after the application of the algorithm to the data set, when the deterministic and stochastic parts as well as the Lévy index are known, the assumption

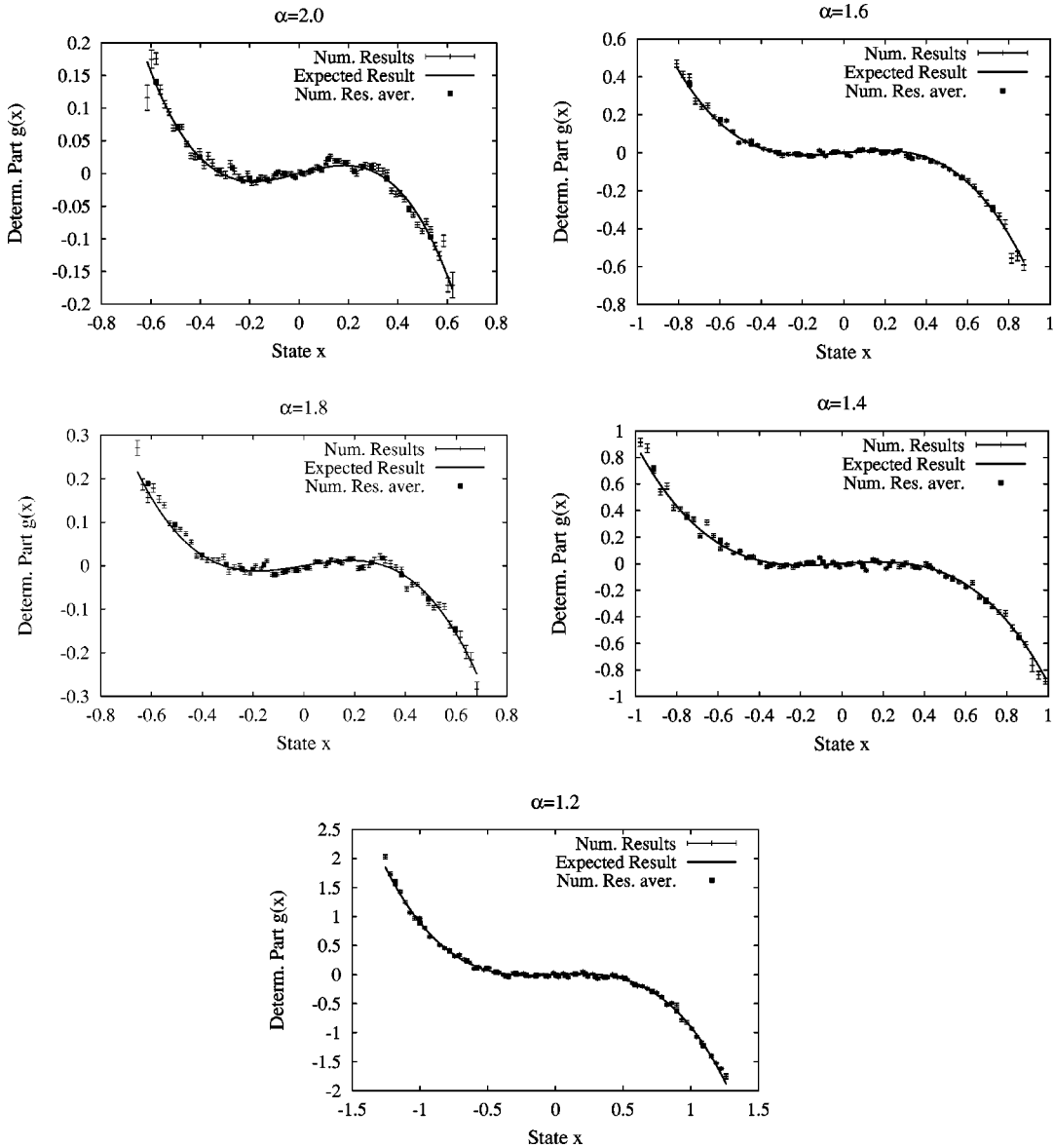


FIG. 5. Numerically determined values for the deterministic function  $g(x)$  of system (40)–(42) in state space  $\{x\}$  for different Lévy indices  $\alpha$ . The values were calculated directly by data analysis of the time series shown in subsequences in Fig. 4, were smoothed, and were compared with the theoretical curve.

of the system belonging to this class of Langevin-like systems can be tested. Therefore, a new numerically calculated time series  $\mathbf{Y}(t)$  can be integrated according to

$$\begin{aligned} Y_i(t + \Delta t_{sim.}) &= g_{iE}(\mathbf{Y}(t)) \Delta t_{sim} \\ &+ \tilde{h}_{iiE}(\mathbf{Y}(t)) (\Delta t_{sim})^{(1/\alpha_E)} f_{(\alpha_E)}^{(\gamma=1, \beta=0, \mu=0)}(t). \end{aligned} \quad (38)$$

$\Delta t_{sim}$  should be in the range of the internal dynamical time scale. If the dynamical structure is known it is possible to choose a suitable integration step. Besides, the relation

$$\Delta t_{samp} = n \Delta t_{sim} \quad (39)$$

should be fulfilled with large  $n$  and  $\Delta t_{samp}$  being the sampling time of the measured and investigated time series  $\mathbf{X}(t)$ .

The needed values for the deterministic and stochastic functions can be found by interpolation within that part of the state space where numerical results exist. In the outer part of the phase space, for large deviations of the time series, the numerical results can be extrapolated. According to the law of rare events the extrapolation is done in a linear way.

If the investigated time series  $\mathbf{X}(t)$  is describable by an iteration like Eq. (16) then all statistical qualities of both series  $\mathbf{X}(t)$  and  $\mathbf{Y}(t)$  should be equal within the range of the determined uncertainties. As one example, the conditional probability densities  $p(x_1, t + \Delta t_{samp} | x_0, t)$  can be calculated for every  $x_0$  for both time series and the functions can be compared. If there is a good agreement of the distributions

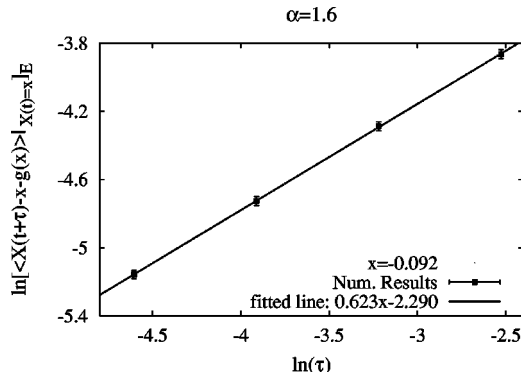


FIG. 6. Logarithm of the numerically calculated conditional average  $1/N \sum_{n=1}^N [X(t_n + \tau) - X(t_n) - g(x)\tau] |_{X(t)=x \pm \Delta x}$  of the stochastic variable  $X(t)$  over the logarithm of the time difference  $\tau$  with  $x = 0.092$ . The straight line was fitted to the numerically calculated values represented by the points with error bars.

for all  $x_0$  the investigated time series  $X(t)$  belongs to the class of Langevin-like equations and it was justified to make the assumption of the algorithm.

## VI. APPLICATION OF THE ALGORITHM

Results of an application of the presented algorithm to artificially created data sets will be shown in this section. As example, the dynamical system of a one-dimensional Pitchfork bifurcation with dynamical Lévy noise is used,

$$dX(t) = g(X(t)) + h(X(t))dL_\alpha^{(\gamma=1, \beta=0, \mu=0)}(t) \quad (40)$$

with

$$g(x) = 0.1x - x^3, \quad (41)$$

$$\begin{aligned} h(x) &= \frac{1}{1000x^2 + 2000\sqrt{0.1}x + 120} \\ &+ \frac{1}{1000x^2 - 2000\sqrt{0.1}x + 120} + 0.05. \end{aligned}$$

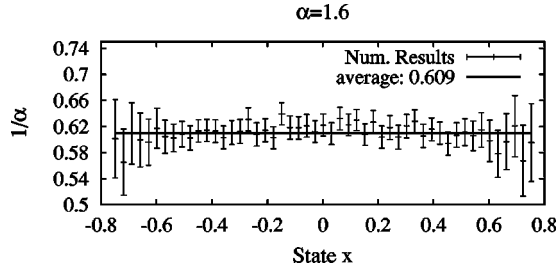


FIG. 7. Numerically determined values for  $1/\alpha$ ,  $\alpha$  being the Lévy index, over state  $x$ . The calculated values are represented by points with error bars, the straight line represents the average of all values.

TABLE I. Theoretical values and numerically determined values with uncertainties for different Lévy indices  $\alpha$  and their inverse  $1/\alpha$ .

$\alpha$	$1/\alpha$	$\alpha$ num.	$1/\alpha$ num.
2.0	0.50	$2.01 \pm 0.03$	$0.50 \pm 0.01$
1.8	0.56	$1.82 \pm 0.03$	$0.55 \pm 0.01$
1.6	0.63	$1.64 \pm 0.04$	$0.61 \pm 0.01$
1.4	0.71	$1.45 \pm 0.06$	$0.69 \pm 0.03$
1.2	0.83	$1.28 \pm 0.09$	$0.78 \pm 0.06$

$h(x)$  has been chosen in this way to produce a positive function with two maxima and constant asymptotic behavior for  $|x| \rightarrow \infty$ . The differential equation has been integrated numerically according to

$$\begin{aligned} X(t + \Delta t_{sim}) &= X(t) + g(X(t))\Delta t_{sim} \\ &+ h(X(t))(\Delta t_{sim})^{1/\alpha} f_\alpha^{(\gamma=1, \beta=0, \mu=0)}(t). \end{aligned} \quad (42)$$

$\Delta t_{sim}$  has been chosen as 0.001 time units, but just every tenth data point of the sample path has been stored for further analysis. This corresponds to a sampling time step of  $\Delta t_{samp} = 0.01$  time units. For  $\alpha$  the values 2.0, 1.8, 1.6, 1.4, 1.2 have been taken. Figure 4 illustrates Lévy noise realizations for these Lévy indices and subsequences of the corresponding integrated motions according to the relations (40)–(42).

For each of the time series the deterministic part of the underlying dynamics has been determined according to relation (17). The results are shown in Fig. 5. The numerically determined values are represented by points with error bars, which are quite small. The numerical results have been averaged to eliminate smaller fluctuations, the results are given by circles. The solid line is the expected curve according to Eq. (41).

If  $g(x)$  is known,  $\alpha$  can be determined. As an example for the proceeding that has been described in detail above, the ln-ln-plot and the fitted straight line for  $\alpha = 1.6$  and  $x = -0.092$  are shown in Fig. 6. Figure 7 shows the distribution of all numerically calculated results for  $\alpha$  for different  $x$  in the case  $\alpha = 1.6$  and the affiliated mean value.

In Table I the numerically determined values for  $1/\alpha$  and  $\alpha$  together with their uncertainties are listed for all investigated cases.

Finally, Fig. 8 shows the determined stochastic functions for all investigated cases. As in Fig. 4 the points with error bars stand for the numerically calculated values. The squares are averages of these analysis results. The solid curve represents the expected function according to system (40)–(42).

With the help of the numerically determined values for the deterministic and the stochastic parts of the dynamics a new time series  $Y(t)$  has been integrated according to relation (38). The needed values for the deterministic and stochastic function have been found by interpolation or linear extrapolation. Figure 9 shows the original, analyzed time series  $X(t)$  and the reconstructed time series  $Y(t)$  for the different Lévy indices  $\alpha$ .

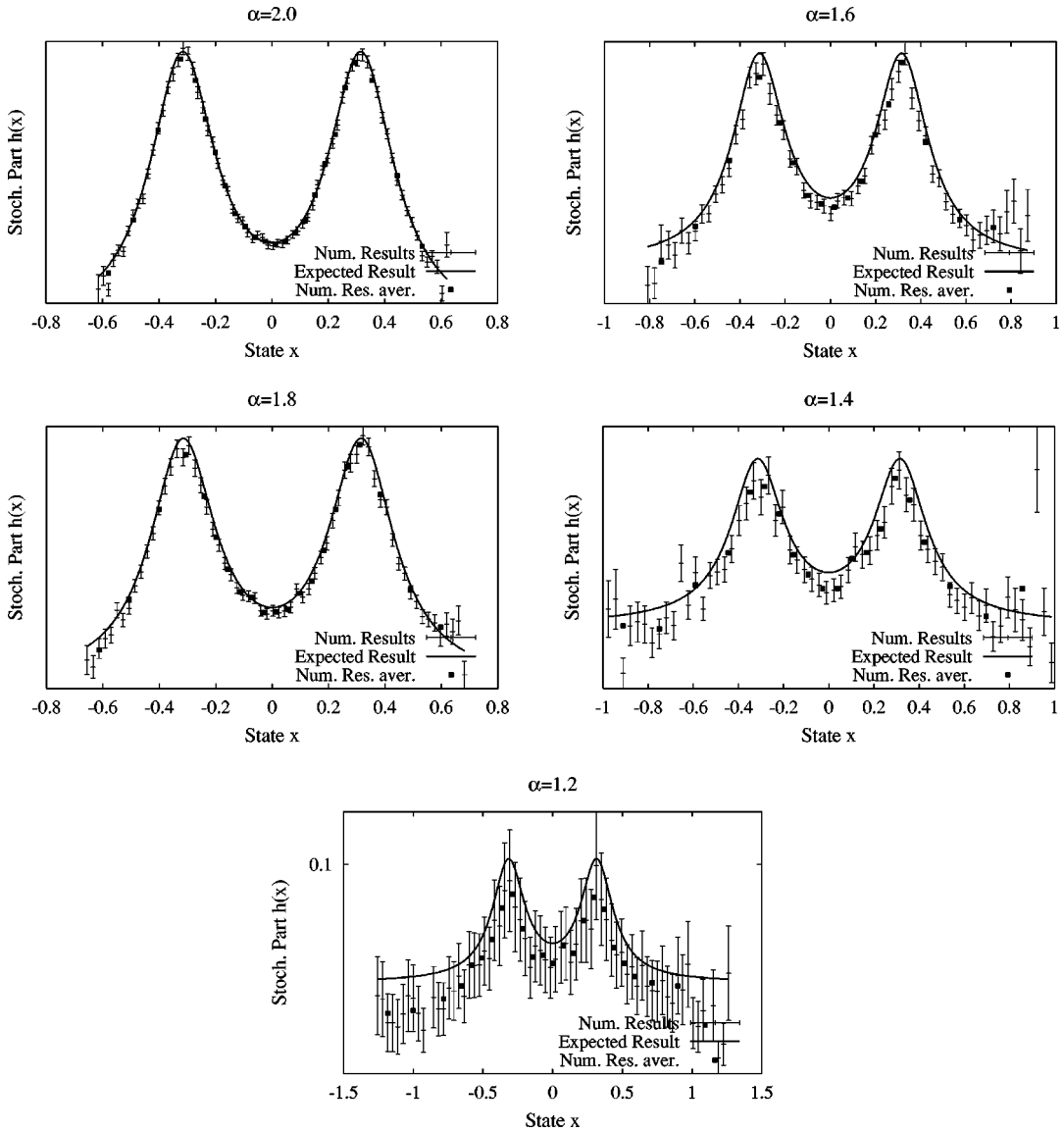


FIG. 8. Numerically determined values for the stochastic function  $h(x)$  of system (40)–(42) in state space  $\{x\}$  for different Lévy indices  $\alpha$ . The values were calculated directly by data analysis of the time series shown in subsequences in Fig. 4, were smoothed and were compared with the theoretical curve.

As last step of the analysis, the assumption that the investigated system belongs to the class (16) of dynamical systems has to be validated. This is done by comparison of the conditional probability densities  $p(x_1, t + \Delta t_{\text{samp}} | x_0, t)$  for different  $x_0$  calculated on the one hand side by the measured trajectory and on the other hand by the reconstructed trajectory. For the Lévy index  $\alpha = 2.0$  (Gaussian process) Fig. 10 shows the probability distributions for some values of  $x_0$ . For calculating the distributions of the reconstructed time series 20 million points have been integrated.

## VII. DISCUSSION OF THE RESULTS

In Figs. 5 and 8 numerical analysis results for the deterministic and stochastic parts of the investigated dynamical system are presented. Some interesting things concerning these results shall be remarked.

The  $x$  range in state space of the results increases with decreasing  $\alpha$ . Numerical results can only be calculated for those  $x$  values in state space that are visited statistically often by the measured trajectory. Smaller Lévy indices  $\alpha$  lead to larger, quite frequent deviations so that the area of the phase space that is covered by the investigated trajectory increases with decreasing Lévy index.

The greater the number of the trajectory's visits of a point  $x$  in state space is, the smaller is the uncertainty of the numerical results at this point. This explains why the error bars are bigger in the extreme regions of the covered and analyzed phase space than at the attracting points. The impression of smaller error bars in the deterministic parts for smaller Lévy indices is just caused by different scales of the coordinate axis.

If the behavior of the system shall be investigated in regions that are normally not visited by the trajectory, the sys-

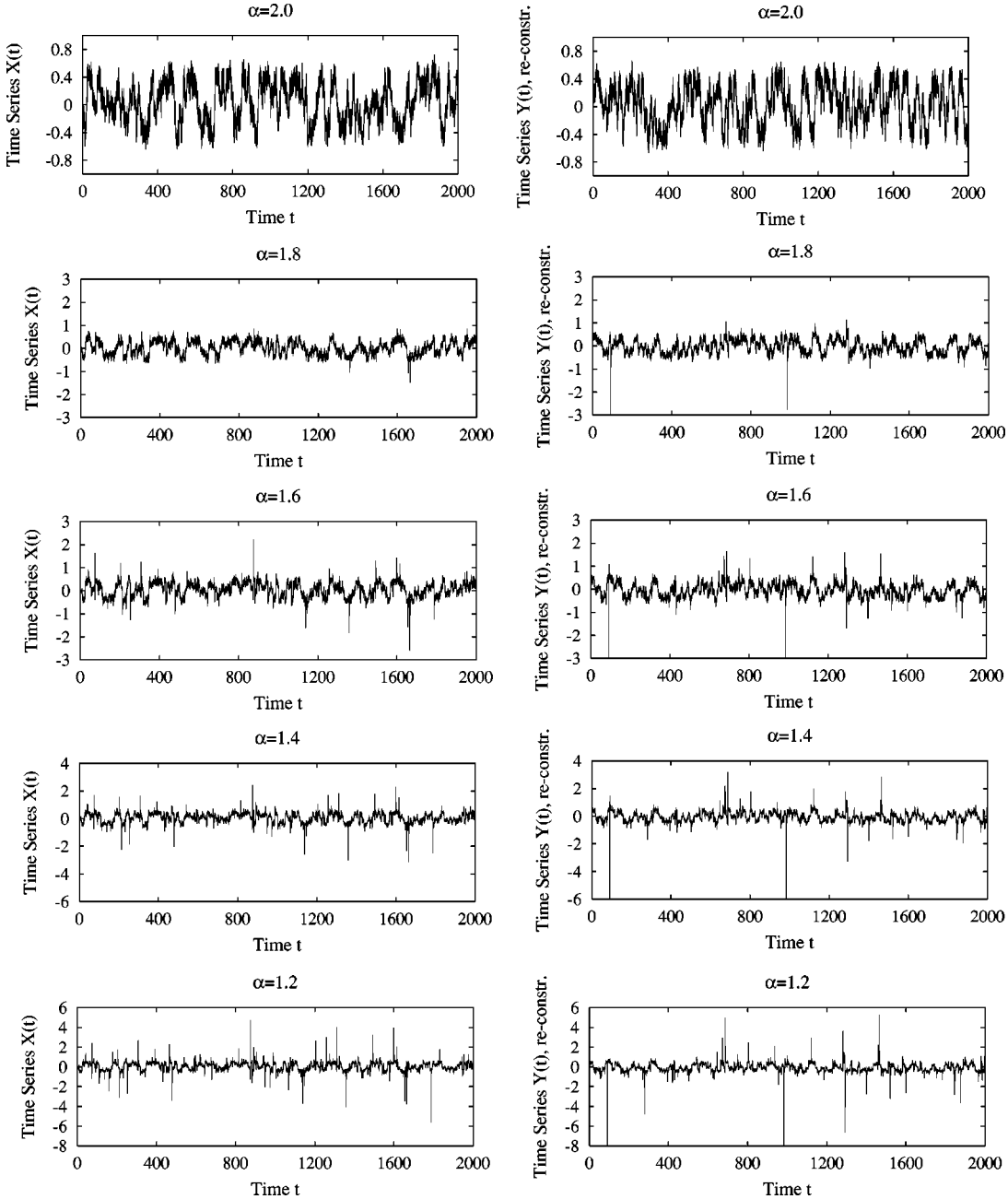


FIG. 9. Investigated time series  $X(t)$ , generated by iteration (42), over time  $t$ , in comparison with the reconstructed time series  $Y(t)$  over time  $t$ , generated according to Eq. (38) with the numerically determined dynamical functions that have been found by data analysis.

tem has to be disturbed by additional dynamical noise in such a way that the trajectory covers the parts of state space of interest.

In Fig. 7 the determined values for  $\alpha$  in the case  $\alpha=1.6$  are plotted together with their uncertainties for different values of  $x$ . Again, it can be recognized that the uncertainty increases for extreme values of the covered state space because of a decreasing number of visits.

In Fig. 8 numerical results for the stochastic part of the investigated dynamical system are presented. Additionally to the comments above about both, the deterministic and stochastic results, one recognizes a strong increase of the uncertainties with smaller Lévy index  $\alpha$ . This can be understood by relation (37).

In Fig. 9 subsequences of the analyzed time series and the reconstructed time series are plotted for different values of  $\alpha$ . The reconstructed time series has been calculated with the help of the numerically determined values for the deterministic and the stochastic part and the Lévy index. But values for the state dependent functions exist only in those areas of the phase space that have been visited by the trajectory statistically often. In regions in the outer part results can only be found by extrapolation. According to the law of rare events this has been done in a linear way. When comparing the original and the reconstructed time series one recognizes a statistically identical behavior in the main part of the covered state space, but a slightly different behavior in strong deviations. The extreme values are taken by the recon-

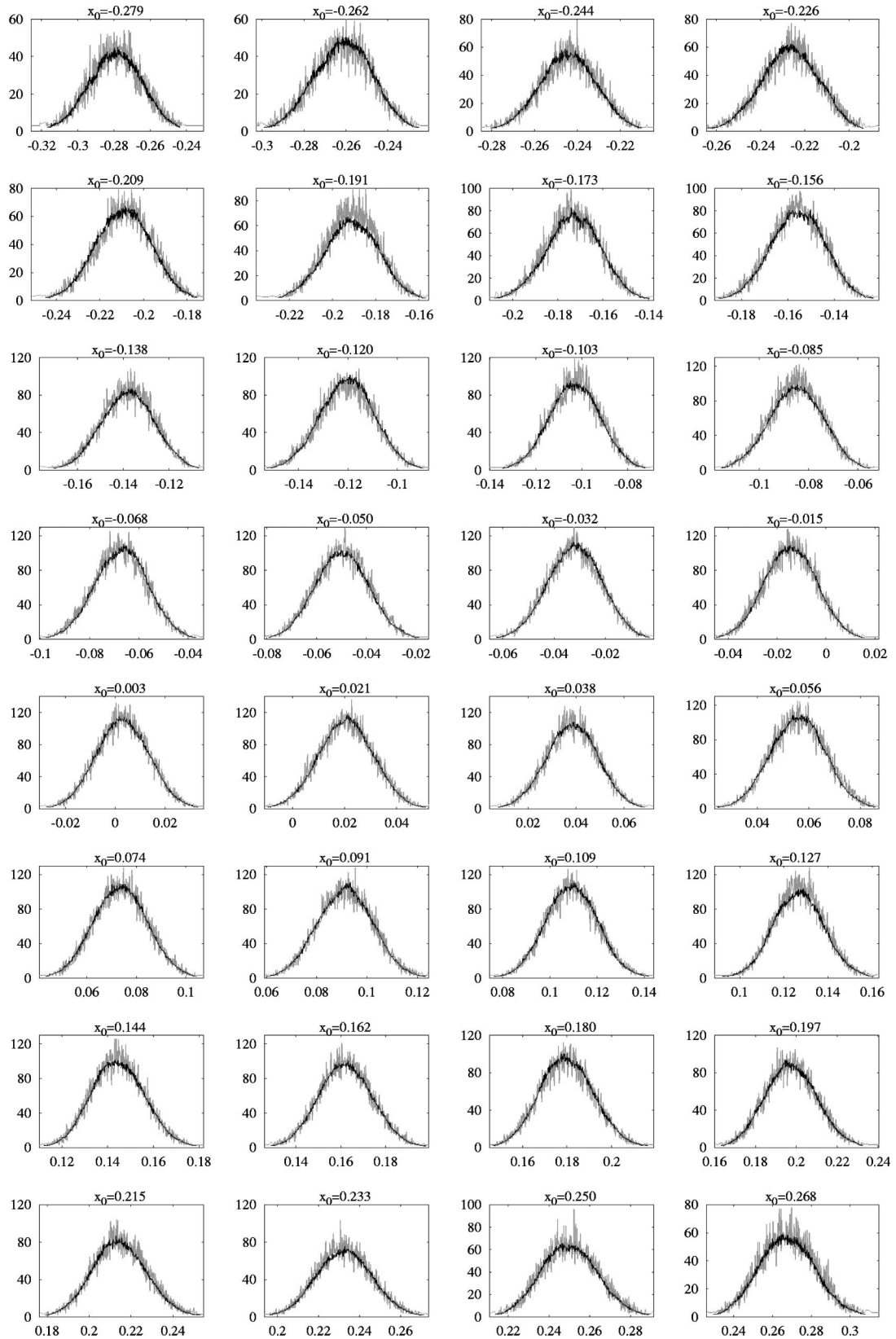


FIG. 10. Conditional probability density functions  $p(x_1, t + \Delta t_{\text{samp}} | x_0, t)$  in arbitrary units over state  $x_1$  for different values of  $x_0$  for  $\alpha=2.0$ . The light curve belongs to the measured time series, the dark curve has been determined by the reconstructed time series.

structed trajectory statistically as often as by the original time series, but the recurrence to the main part of the state space is fulfilled in a slower way because of the linear extrapolation.

In Fig. 10 the functions of the probability density distribution  $p(x_1, t + \Delta t_{\text{sample}} | x_0, t)$  are plotted for different values of  $x_0$  for the Lévy index  $\alpha = 2.0$ . A good agreement of the affiliated distributions can be recognized. The stronger fluctuations of the distributions of the measured trajectory for  $\alpha = 2.0$  in comparison with the distributions of the reconstructed trajectory are caused by the smaller number of data points (factor 20). The more data points are used for the calculation of the probability density distributions the smaller are the fluctuations.

### VIII. SUMMARY

A method was presented that allows the data analysis of nonlinear Lévy systems. The Lévy index  $\alpha$  can be determined as well as the deterministic and stochastic nonlinear parts of the dynamics. Model equations for the dynamical evolution of the investigated system can be formulated. Error bars show the uncertainties of the calculated values.

One remarkable feature of the algorithm is that no pre-knowledge about the system, no assumption or functional

ansatz are necessary for the analysis. The only assumption, that the system belongs to the considered class of dynamical Lévy systems, is validated as last step of the procedure.

The fact that systems with nonlinear deterministic as well as nonlinear stochastic parts, can be investigated opens up the way to a lot of unknown, so far not investigated and modeled systems, physical systems as well as biological, medical or technical systems. Model equations that have been set up by logical reasons, symmetry or just experience can be validated or formulated in a more detailed way.

It was shown how time series can be reconstructed. By this way time series with any number of data points can be calculated. With the help of these reconstructed time series the long-time behavior of the investigated system can be simulated and characteristics whose calculation requires long series can be determined.

The presented method allows a data-driven formulation of model equations for the wide class of self-consistent nonlinear stochastic processes.

### ACKNOWLEDGMENTS

The authors thank A. Zanker for fruitful discussions and the German foundation “Studienstiftung des deutschen Volkes” for their support of this work.

- 
- [1] C. W. Gardiner, *Handbook of Stochastic Methods*, 2nd ed. (Springer-Verlag, Berlin, 1985).
  - [2] H. Risken, *The Fokker-Planck Equation* (Springer-Verlag, Berlin, 1989).
  - [3] J. Honerkamp, *Stochastische Dynamische Systeme* (VCH Verlagsgesellschaft, Weinheim, 1990).
  - [4] H. Haken, *Advanced Synergetics* (Springer-Verlag, Berlin, 1983).
  - [5] H. Haken, *Information and Self-Organization* (Springer-Verlag, Berlin, 1988).
  - [6] S. Siegert, R. Friedrich, and J. Peinke, Phys. Lett. A **243**, 275 (1998).
  - [7] R. Friedrich, S. Siegert, and J. Peinke, in *Transport and Structure*, edited by S. C. Müller, J. Parisi, and W. Zimmermann (Springer-Verlag, Berlin, 1999).
  - [8] R. Friedrich, S. Siegert, J. Peinke, St. Lück, M. Siefert, M. Lindemann, J. Raethjen, G. Deuschl, and G. Pfister, Phys. Lett. A **271**, 217 (2000).
  - [9] J. Gradišek, S. Siegert, R. Friedrich, and I. Grabec, Phys. Rev. E **62**, 3146 (2000).
  - [10] J. Gradišek, S. Siegert, R. Friedrich, and I. Grabec, in *Stochastic and Chaotic Dynamics in the Lakes: Stochaos*, edited by D. S. Broomhead, E. A. Luchinskaya, P. V. E. McClintock, and T. Mullin, AIP Conf. Proc. No. 502 (AIP, Melville, NY, 2000), pp. 476–481.
  - [11] P. Lévy, *Calcul des Probabilités* (Gauthier-Villars, Paris, 1925).
  - [12] P. Lévy, *Théorie de l'Addition des Variables Aléatoires* (Gauthier-Villars, Paris, 1937).
  - [13] W. Feller, *An Introduction to Probability Theory and Its Application* (Wiley, New York, 1957), Vol. 1; W. Feller, *An Introduction to Probability Theory and Its Application* (Wiley, New York, 1966), Vol. 2.
  - [14] H. C. Fogedby, Phys. Rev. Lett. **73**, 2517 (1994).
  - [15] S. Jespersen, R. Metzler, and H. C. Fogedby, Phys. Rev. E **59**, 2736 (1999).
  - [16] G. Zumofen and J. Klafter, Phys. Rev. E **51**, 2805 (1995).
  - [17] O. V. Bychuk and B. O'Shaughnessy, Phys. Rev. Lett. **74**, 1795 (1995).
  - [18] S. Stapf, R. Kimmich, and R.-O. Seitter, Phys. Rev. Lett. **75**, 2855 (1995).
  - [19] J. Bodurka, R.-O. Seitter, R. Kimmich, and A. Gutsze, J. Chem. Phys. **107**, 5621 (1997).
  - [20] A. Ott, J. P. Bouchaud, D. Langevin, and W. Urbach, Phys. Rev. Lett. **65**, 2201 (1990).
  - [21] G. Zumofen, A. Blumen, J. Klafter, and M. F. Shlesinger, J. Stat. Phys. **54**, 1519 (1989).
  - [22] G. M. Viswanathan, V. Afanasyev, S. V. Buldyrev, E. Murphy, P. A. Prince, and H. E. Stanley, Nature (London) **381**, 413 (1996).
  - [23] J. Klafter, A. Blumen, and M. F. Shlesinger, Phys. Rev. A **35**, 3081 (1987).
  - [24] H. C. Fogedby, Phys. Rev. E **50**, 1657 (1994).
  - [25] R. Metzler, E. Barkai, and J. Klafter, Europhys. Lett. **46**, 431 (1999).
  - [26] G. Samorodnitzky and M. Taqqu, *Stable Non-Gaussian Random Processes* (Chapman & Hall, New York, 1994).
  - [27] J. Honerkamp, *Statistical Physics* (Springer-Verlag, Berlin, 1998).

## Analysis of time series from stochastic processes

Janez Gradisek,<sup>1,\*</sup> Silke Siegert,<sup>2</sup> Rudolf Friedrich,<sup>2</sup> and Igor Grabec<sup>1</sup>

<sup>1</sup>*Faculty of Mechanical Engineering, University of Ljubljana, Aškerčeva 6, SI-1000 Ljubljana, Slovenia*

<sup>2</sup>*Institute for Theoretical Physics 3, University of Stuttgart, Pfaffenwaldring 57/5, D-70550 Stuttgart, Germany*

(Received 5 April 2000)

Analysis of time series from stochastic processes governed by a Langevin equation is discussed. Several applications for the analysis are proposed based on estimates of drift and diffusion coefficients of the Fokker-Planck equation. The coefficients are estimated directly from a time series. The applications are illustrated by examples employing various synthetic time series and experimental time series from metal cutting.

PACS number(s): 02.50.Ey, 02.50.Fz, 05.45.-a

### I. INTRODUCTION

All experimental data are to a certain extent contaminated by noise. Generally, one can distinguish between measurement noise and dynamic noise. Measurement noise is caused by measurement procedures; it is superimposed on the measured signal, and it can not influence the dynamics of the process. Dynamic noise is part of the process dynamics and can play an important role when the process is close to an instability point [1]. Time series from various processes in nature are stochastic, and it is often reasonable to assume that they contain both types of noise. However, most nonlinear techniques for time series analysis, especially those inspired by chaos theory [2], require the time series to be generated by a deterministic process, and only allow for negligible measurement noise. Consequently, the applicability of these methods to the analysis of stochastic time series is limited.

A method for analysis of stochastic data sets was recently proposed [3,4] which assumes that the data contain the additive type of dynamic noise. The evolution law of a process which generates such signals can be written as  $\dot{\mathbf{X}}(t) = \mathcal{F}[\mathbf{X}(t)] + \boldsymbol{\eta}(t)$ , where  $\mathbf{X}(t)$  denotes the process state at time  $t$ ,  $\mathcal{F}(\cdot)$  is a nonlinear function, and  $\boldsymbol{\eta}(t)$  denotes noise. The dynamics of this type of processes can also be described by the Fokker-Planck equation, which is determined by drift and diffusion coefficients. Using the method proposed in Refs. [3,4], one can estimate these coefficients directly from noisy data for a certain class of processes. Thus, a complete description of a stochastic process can be found, and the deterministic laws of the process dynamics, as well as the form and the strength of the noise, can be determined.

By extracting drift and diffusion coefficients separately from a time series, the dynamics of a stochastic process are decomposed into a deterministic and a random component. Such decomposition of the dynamics offers several new possibilities for analysis of stochastic processes. The aim of this paper is to demonstrate the following: (a) When the deterministic dynamics' component is represented as a vector field, it provides qualitative information about the local stability properties of the process in the phase space. (b) The

extracted dynamics' components can be used to reconstruct the process evolution. Deterministic evolution can be reconstructed based only on the deterministic component. (c) When both the deterministic and the random component are employed for the reconstruction, one can generate typical stochastic trajectories of the process. These trajectories possess the same deterministic and random properties as the original time series. (d) Typical trajectories can be applied to estimate the mean first passage time, i.e., the mean time elapsed between successive visits of the process trajectory to selected locations in the phase space.

We first illustrate these applications by examples employing synthetic time series generated by (1) a stochastic system exhibiting the pitchfork bifurcation, (2) the stochastic van der Pol oscillator, and (3) the stochastic Lorenz system in a chaotic regime. Next, we use the applications to analyze experimental time series obtained under different regimes of metal cutting.

### II. METHOD FOR ANALYSIS OF STOCHASTIC PROCESSES

The method proposed in Refs. [3,4] is a general method for the estimation of the drift and diffusion coefficients of the Fokker-Planck equation for stationary continuous Markovian stochastic processes. Let the evolution of a continuous  $m$ -dimensional stochastic variable  $\mathbf{X}(t)$  in phase space  $s_{\mathbf{X}}$  be governed by the Langevin equation:

$$\frac{dX_i(t)}{dt} = h_i(\mathbf{X}(t)) + \sum_j g_{ij}(\mathbf{X}(t))\Gamma_j(t), \quad (1)$$

where the fluctuating Langevin forces  $\Gamma_j(t)$  represent random noise, which is assumed to be uncorrelated,  $\langle \Gamma_i(t)\Gamma_j(t') \rangle = Q\delta_{ij}\delta(t-t')$ , with vanishing mean,  $\langle \Gamma_i(t) \rangle = 0$ , for each  $i,j$ . Due to the random term, Eq. (1) can only rarely be solved. Alternatively, the dynamic behavior of the underlying stochastic process can be described by the Fokker-Planck equation, which describes the evolution of the conditional probability density distribution of the stochastic variable  $\mathbf{X}$  in the phase space  $s_{\mathbf{X}}$ :

\*Electronic address: janez.gradisek@fs.uni-lj.si

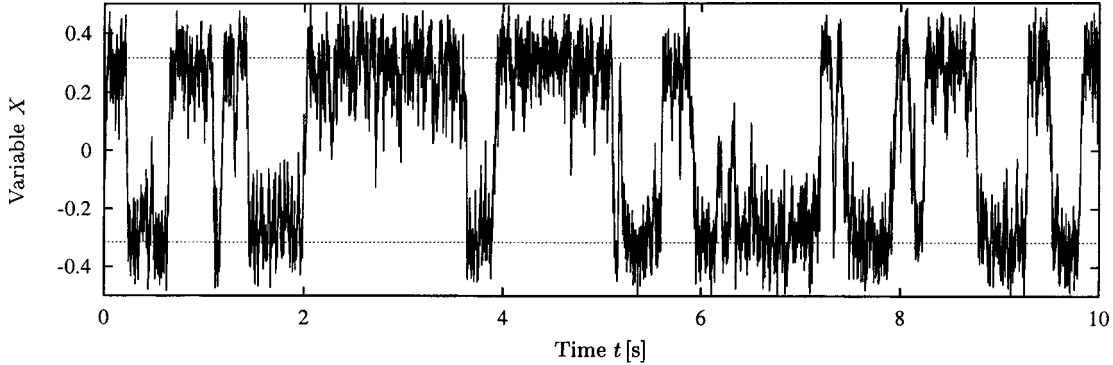


FIG. 1. Time series of a variable  $X$  from Eq. (A1). The dotted lines at  $\pm\sqrt{0.1}$  denote the two stable fixed points.

$$\begin{aligned} \frac{\partial p(\mathbf{x}, t+\tau | \mathbf{x}, t)}{\partial t} = & \left( - \sum_i \frac{\partial}{\partial x_i} D_i^{(1)}(\mathbf{x}, t) \right. \\ & \left. + \frac{1}{2} \sum_{i,j} \frac{\partial^2}{\partial x_i \partial x_j} D_{ij}^{(2)}(\mathbf{x}, t) \right) p(\mathbf{x}, t+\tau | \mathbf{x}, t). \end{aligned} \quad (2)$$

$D_i^{(1)}$  and  $D_{ij}^{(2)}$  are called drift and diffusion coefficients, respectively. If Itô's definitions of stochastic integrals are applied [5], the coefficients  $\mathbf{D}^{(1)}$  and  $\mathbf{D}^{(2)}$  can be related to the deterministic and random terms of the Langevin equation as [6]

$$D_i^{(1)}(\mathbf{x}, t) = h_i(\mathbf{x}, t), \quad (3a)$$

$$D_{ij}^{(2)}(\mathbf{x}, t) = Q \sum_k g_{ik}(\mathbf{x}, t) g_{jk}(\mathbf{x}, t). \quad (3b)$$

If coefficients  $\mathbf{D}^{(1)}$  and  $\mathbf{D}^{(2)}$  are estimated from the time series generated by the stochastic process, the dynamics of the process are in fact completely determined. Using Eqs. (3), one can further determine the deterministic term, as well as the form and strength of the fluctuating term in the Langevin equation.

For the class of stationary continuous Markovian processes with uncorrelated dynamical noise, it is always possible to determine drift and diffusion coefficients directly from given data [3,4] by using their statistical definition [6]:

$$D_i^{(1)}(\mathbf{x}, t) = \lim_{\tau \rightarrow 0} \frac{1}{\tau} \langle X_i(t+\tau) - x_i \rangle_{X(t)=\mathbf{x}}, \quad (4a)$$

$$D_{ij}^{(2)}(\mathbf{x}, t) = \lim_{\tau \rightarrow 0} \frac{1}{\tau} \langle (X_i(t+\tau) - x_i)(X_j(t+\tau) - x_j) \rangle_{X(t)=\mathbf{x}}. \quad (4b)$$

Here  $\mathbf{X}(t+\tau)$  is a solution of Eq. (1) which starts at  $\mathbf{X}(t) = \mathbf{x}$  at time  $t$ . In practice,  $\mathbf{D}^{(i)}$  can be determined from the following relations for a small time step  $\tau$ :

$$D_i^{(1)}(\mathbf{x}) = T_i^{(1)}(\mathbf{x}, \tau), \quad (5a)$$

$$D_{ij}^{(2)}(\mathbf{x}) = T_{ij}^{(2)}(\mathbf{x}, \tau) - \tau T_i^{(1)}(\mathbf{x}, \tau) T_j^{(1)}(\mathbf{x}, \tau). \quad (5b)$$

The terms

$$T_i^{(1)}(\mathbf{x}, \tau) = \frac{1}{\tau} \int_{-\infty}^{\infty} (y_i - x_i) p(\mathbf{y}, t+\tau | \mathbf{x}, t) \prod_k dy_k, \quad (6a)$$

$$T_{ij}^{(2)}(\mathbf{x}, \tau) = \frac{1}{\tau} \int_{-\infty}^{\infty} (y_i - x_i)(y_j - x_j) p(\mathbf{y}, t+\tau | \mathbf{x}, t) \prod_k dy_k \quad (6b)$$

denote the conditional moments which can be determined by numerical integration. For a stationary process,  $p(\mathbf{y}, t+\tau | \mathbf{x}, t)$  and, consequently,  $\mathbf{T}^{(i)}$  and  $\mathbf{D}^{(i)}$  are independent of time.

We illustrate the method using a one-dimensional time series generated by the Langevin equation valid for systems which exhibit noisy pitchfork bifurcation. A typical segment of a time series is shown in Fig. 1. The corresponding equation and its parameters are described in the Appendix. The estimated drift and diffusion coefficients are shown in Fig. 2 together with their theoretical dependence on  $x$ . The dependences  $D^{(i)}(x)$  estimated from the time series closely follow the theoretical ones. The largest discrepancies between the theoretical and the estimated dependences are observed in the vicinity of  $x=0$ , and at the edges of the phase space. The reason for this lies in the infrequent visits of the process trajectory to these intervals of  $x$  (Fig. 1), which results in less reliable estimates of conditional probability density in these intervals.

Obviously, the better the estimate of conditional probability density, the better the estimates of the coefficients  $\mathbf{D}^{(i)}$  obtained by the method. For the results presented in this paper we estimated the probability density using histograms with equidistant bins.

An important issue related to the estimation of coefficients  $\mathbf{D}^{(i)}$  is their dependence on the time step  $\tau$ . This dependence is discussed in detail elsewhere [7], and only the main results are given below.

*The effect of time step  $\tau$ .* For the sake of simplicity, let us consider a one-dimensional process for which the Fokker–Planck operator  $L$ ,

$$L = - \frac{\partial}{\partial x} D^{(1)}(x) + \frac{1}{2} \frac{\partial^2}{\partial x^2} D^{(2)}(x), \quad (7)$$

possesses real eigenvalues  $\lambda_j \leq 0$  and eigenvectors  $\Phi_j(x)$ . The conditional probability density can be expressed in the form of an infinite series as

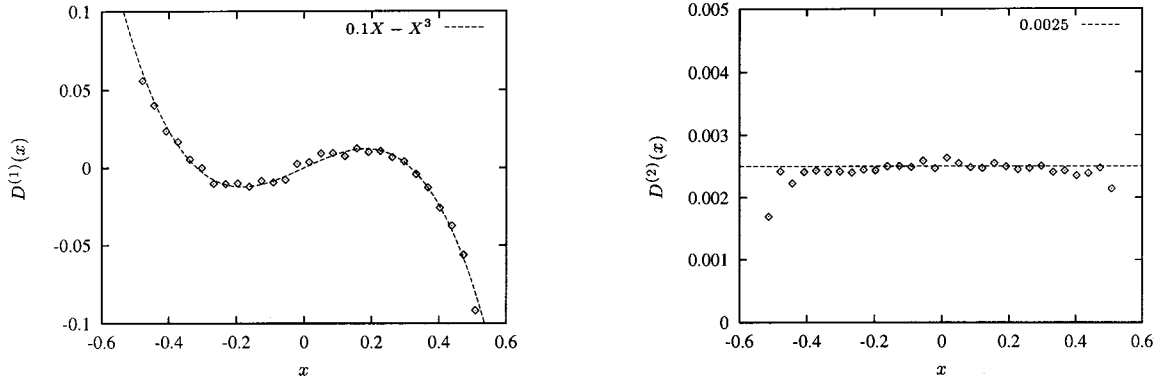


FIG. 2. The estimated drift and diffusion coefficients (diamonds) compared to their theoretical dependence on  $x$  (dashed line).

$$p(y, t' | x, t) = \sum_j e^{\lambda_j(t' - t)} \Phi_j^\dagger(x) \Phi_j(y), \quad (8)$$

where  $t' - t = \tau$ . The conditional moments are given by

$$\begin{aligned} & \langle (y(t') - x(t))^k \rangle_{y(t) = x(t)} \\ &= \sum_j e^{\lambda_j(t' - t)} \Phi_j^\dagger(x) \int_{-\infty}^{\infty} (y - x)^k \Phi_j(y) dy \end{aligned} \quad (9)$$

and the following expansions for drift and diffusion coefficients are obtained [7]:

$$D^{(1)}(x) = \sum_j \lambda_j \Phi_j^\dagger(x) \int_{-\infty}^{\infty} (y - x) \Phi_j(y) dy, \quad (10a)$$

$$D^{(2)}(x) = \sum_j \lambda_j \Phi_j^\dagger(x) \int_{-\infty}^{\infty} (y - x)^2 \Phi_j(y) dy. \quad (10b)$$

When coefficients  $D^{(i)}$  are estimated from data, the infinite series (8)–(10) are approximated by finite ones which contain  $N$  eigenfunctions. In order to obtain accurate information about the conditional probability distribution and coefficients  $D^{(i)}$ , one has to choose a time step  $\tau$  such that  $e^{\lambda_N \tau} > 0$ , for sufficiently large  $N$  [7].

As an example, let us use a time series generated by Eq. (A1). Coefficients  $D^{(i)}$  estimated from the data using different values of  $\tau$  are shown in Fig. 3. At  $\tau = 0.01, 0.1$ , and  $1$ , the estimated drift coefficients match the theoretical values well, whereas for the diffusion coefficient the agreement

with the theoretical values is already lost at  $\tau = 1$ . Indeed, the dependence of root-mean-squared error  $\mathcal{E}$  of the estimates on the time step  $\tau$  confirms that the error of  $D^{(2)}$  estimates grows with increasing  $\tau$  faster than the error of  $D^{(1)}$  estimates (Fig. 4). Our experience suggests that the maximum acceptable time step  $\tau_{\max}$  for accurate estimate of the diffusion coefficient is approximately one order of magnitude smaller than  $\tau_{\max}$  which is acceptable for the estimate of drift coefficient. In terms of Eqs. (10) this means that, if the series are to approximate both coefficients equally well, the number of terms  $N$  in the series which approximates  $D^{(2)}$  must be larger.

In general, the maximum acceptable time step  $\tau_{\max}$  or, equivalently, the number of terms  $N$  required in a series depend on the properties of the process. Based on our experience,  $\tau_{\max}$  for the drift coefficient is usually not much shorter than the time step  $t_i$  required for the integration of the corresponding differential equations. For example, in the case of the van der Pol oscillator [Eqs. (A2)] we found  $\tau_{\max} \approx 0.1$ , which results in approximately 80 points per oscillation cycle, whereas the longest reasonable integration step for which the limit cycle is not yet too distorted is approximately  $t_i \approx 0.3$ .

However, in practice one is often faced with experimental data recorded with a time step for which coefficients with decreasing  $\tau$  do not converge to a limit value. In this case, the estimated coefficients should be considered a crude approximation and treated with caution. The lack of convergence of  $D^{(i)}$  with decreasing  $\tau$  can be regarded as an indication of the non-Markovian properties of the process [7].

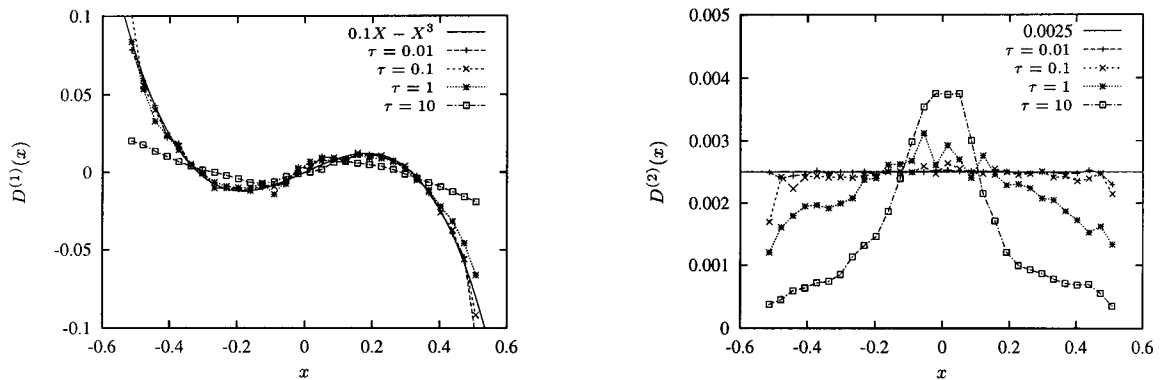
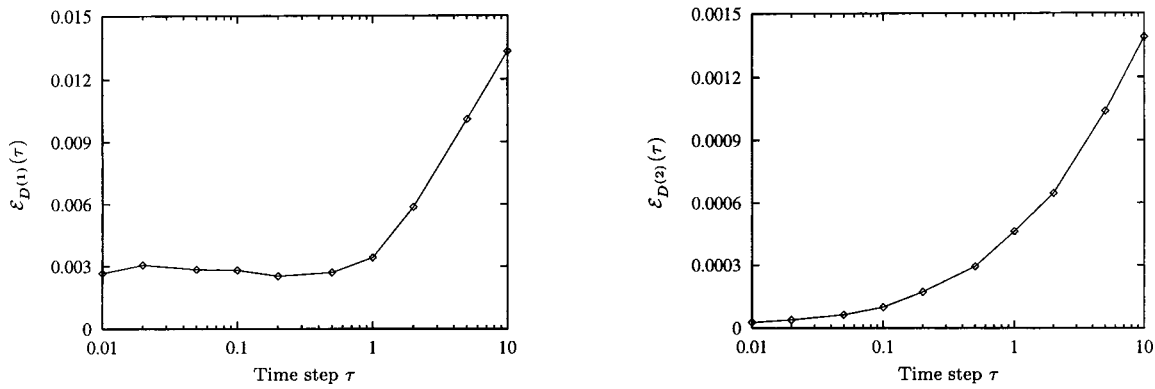


FIG. 3. Coefficients  $D^{(i)}$  estimated using four different time steps  $\tau$ .

FIG. 4. Root-mean-squared error  $\mathcal{E}$  of the coefficients  $D^{(i)}$  versus the time step  $\tau$ .

### III. APPLICATIONS OF THE METHOD

Applications discussed in this section are based mainly on the decomposition of stochastic process dynamics into a deterministic and a random component. For stationary continuous Markovian stochastic processes, such decomposition is performed by estimating the drift and diffusion coefficients of the Fokker–Planck equation as described in Sec. II. According to the relations in Eqs. (3), the drift coefficient  $\mathbf{D}^{(1)}$  corresponds to the deterministic component [Eq. (3a)], while the diffusion coefficient  $\mathbf{D}^{(2)}$  is related to the random component of process dynamics [Eq. (3b)].

Applications are illustrated by examples employing data sets from (a) a stochastic system exhibiting the pitchfork bifurcation, (b) a stochastic van der Pol oscillator, and (c) a stochastic Lorenz system. The corresponding Langevin equations and their parameters are given in the Appendix.

#### A. Deterministic vector field

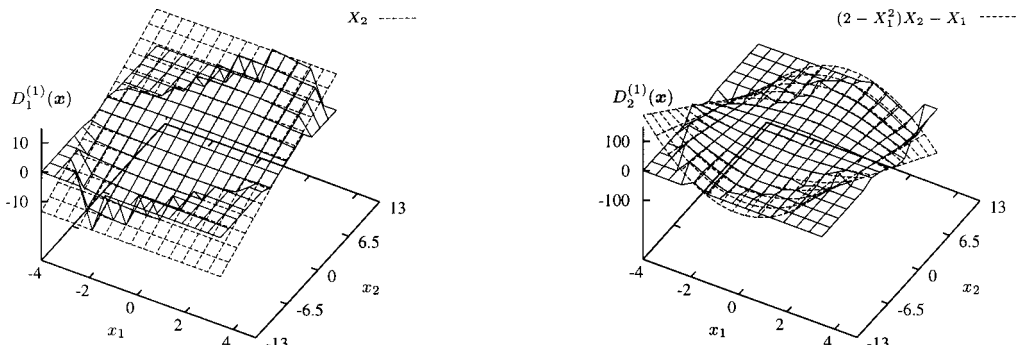
When studying the dynamics of a stochastic process it is interesting to explore how the process would evolve if it was subject to no random influences. This evolution is governed by the deterministic component of the stochastic process dynamics, which in our case is determined by the drift coefficient of the Fokker–Planck equation.

Having extracted the drift coefficient  $\mathbf{D}^{(1)}$  from a stochastic time series, one can plot its components  $D_i^{(1)}$  separately versus the phase space coordinates. Such a plot is shown in Fig. 5 for a stochastic van der Pol oscillator [Eqs. (A2)].  $\mathbf{D}^{(1)}$  was estimated from a vector time series, a portion of which is

shown in the left-hand panel of Fig. 6. Except for the regions where there is no data, the estimates agree well with the theoretical values. However, for an experimentally studied process, for which the dynamics equations are not known, coefficients presented in this way are not easy to interpret.

A more informative presentation of the drift coefficient  $\mathbf{D}^{(1)}$  is achieved by plotting it as a vector field (the right-hand panel of Fig. 6). An arrow in the field graph represents a value of the drift coefficient  $\mathbf{D}^{(1)}(\mathbf{x})$  estimated at location  $\mathbf{x}$  in phase space. The orientation of the arrow indicates the average direction of deterministic motion at  $\mathbf{x}$ . In the case of a van der Pol oscillator (the right-hand panel of Fig. 6), arrows in the vector field point on average in the clockwise direction, suggesting motion on a stable nonsymmetric limit cycle in that direction. Arrows outside the limit cycle run approximately parallel to the cycle around most of the cycle, except at the upper left and at the bottom right corners, where they point towards the cycle. This indicates that the dissipation is close to zero around most of the cycle, and strongly negative at the two corners. The arrows inside the limit cycle point out towards the cycle, suggesting that an unstable fixed point is located in the center of phase space.

The example shows that examination of the drift coefficient presented as a field yields information about the local stability properties of the process. However, the information obtained from the drift coefficient is limited to the region visited by the trajectory during experiments. In order to get information about process properties in other regions of phase space, one should randomly disturb the process during experiments to make it explore a greater portion of its phase space.

FIG. 5. Components of drift coefficient  $\mathbf{D}^{(1)}(\mathbf{x})$  for a stochastic van der Pol oscillator. Solid grid, estimated values. Dashed grid, theoretical values.

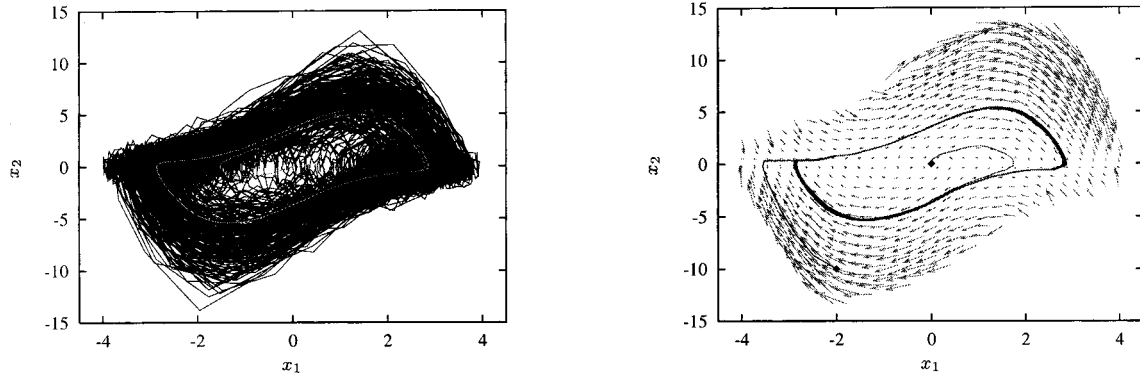


FIG. 6. Left: Phase portraits of a stochastic and a deterministic van der Pol oscillator. Right: The estimated drift coefficient is shown as a vector field with two trajectories superimposed. The trajectories were integrated using the estimated drift coefficient.

### B. Reconstruction of deterministic dynamics

The relationship between the drift coefficient of the Fokker–Planck equation and the deterministic term of the Langevin equation can also be exploited to reconstruct the deterministic dynamics of the process. If we drop the random term of the Langevin equation (1), we can solve the truncated equation numerically using the estimated  $\mathbf{D}^{(1)}$  as

$$\mathbf{X}(t+\Delta t) = \mathbf{X}(t) + \mathbf{D}^{(1)}(\mathbf{X}(t))\Delta t. \quad (11)$$

The solution represents a deterministic trajectory of the process. Two such solutions are shown superimposed on the vector field in the right-hand panel of Fig. 6. The initial conditions of these trajectories (marked by a diamond) lie outside or inside the limit cycle, respectively. Both trajectories terminate on the stable limit cycle after a transient period. For the purpose of comparison, a theoretical deterministic trajectory is shown superimposed on the stochastic phase portrait in the left-hand panel of Fig. 6. This trajectory is a numerical solution of the deterministic term of the equations governing the dynamics of the oscillator [Eqs. (A2)]. The deterministic trajectories obtained by integrating Eq. (11) agree closely with the theoretical deterministic trajectory.

To illustrate that the method is not restricted to trivial attractors, such as fixed points and limit cycles, a vector time series from the stochastic Lorenz system in a chaotic regime was analyzed [Eqs. (A3)]. A portion of the stochastic time series and the extracted drift coefficient are shown in the left-hand and the right-hand panels of Fig. 7. The drift coef-

ficient was used to generate a deterministic trajectory, which is plotted superimposed on the vector field. A trajectory obtained by solving numerically the deterministic equations of the Lorenz system [Eqs. (A3)] is shown superimposed on the stochastic trajectory. Although both deterministic trajectories start at the same point in phase space, they do not follow the same path (the bottom traces in Fig. 8). This discrepancy stems from the imperfect estimation of conditional probability density and from the chaotic nature of the Lorenz system. However, both deterministic trajectories possess similar characteristic patterns, and the phase portraits formed by the trajectories are qualitatively similar (Fig. 7). The main difference can be seen in the inner regions of the two lobes, where the probability density was presumably poorly estimated.

In order to gain an impression of the influence of dynamic noise on the Lorenz system dynamics, compare the upper two traces in Fig. 8 which correspond to the original stochastic and deterministic trajectories. In the stochastic case, noise drives the trajectory from one lobe of the attractor to the other more frequently, and thus prevents the trajectory spiraling in a particular lobe for a protracted period, as is the case in the deterministic system. Nevertheless, the spiraling typical of the Lorenz attractor is clearly observed in the reconstructed deterministic trajectory (the bottom trace). Moreover, note the difference between the extent of the deterministic attractor and the vector field in the right-hand panel of Fig. 7. Dynamic noise increases the extent of the attractor from 45% in the  $x_1$  direction up to 83% in the  $x_3$  direction. Although the noise repeatedly drives the trajectory away

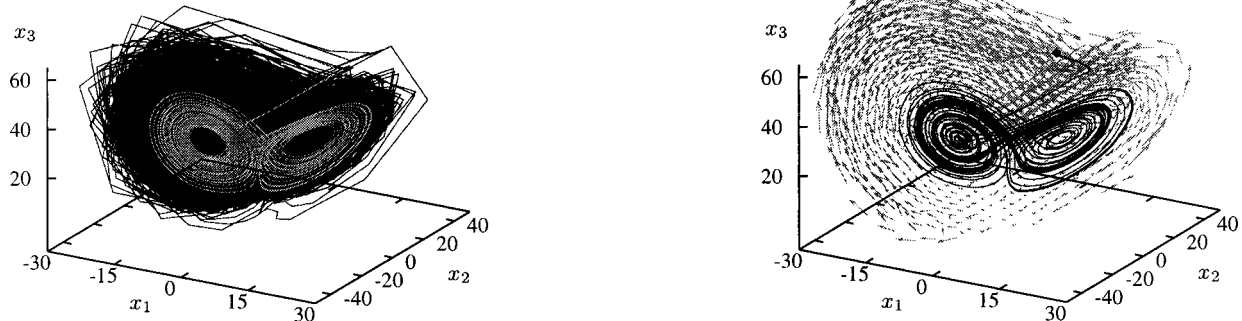


FIG. 7. Left: Phase portraits of a stochastic and a deterministic Lorenz system. Right: The estimated drift coefficient is shown as a vector field with a trajectory superimposed. The trajectory was integrated using the estimated drift coefficient.

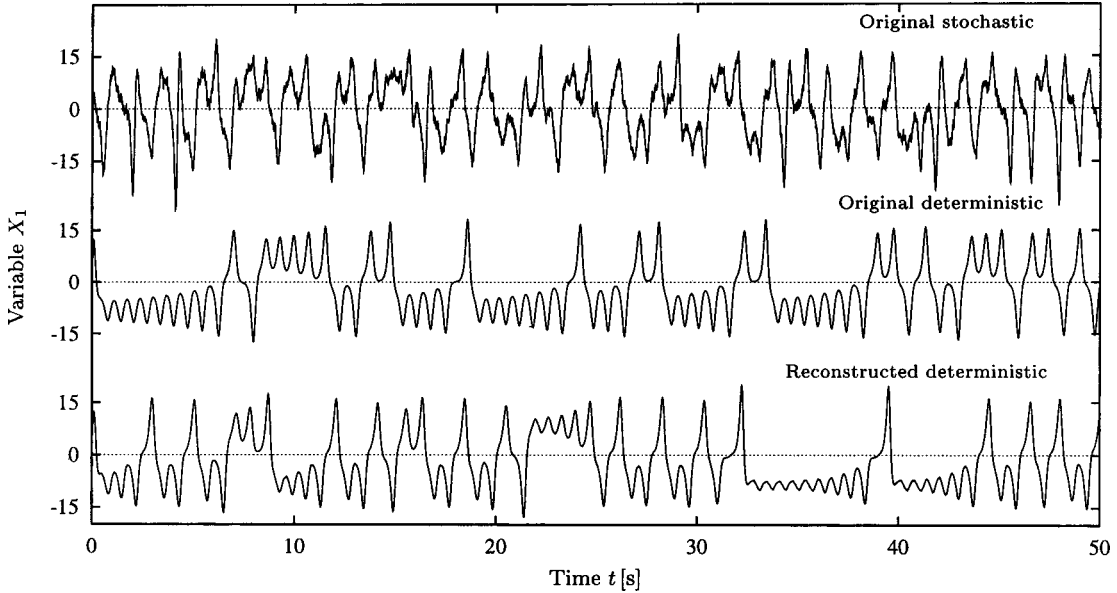


FIG. 8. Comparison of the original stochastic trajectory with the original and reconstructed deterministic trajectories of the Lorenz system.

from the deterministic attractor, the trajectory generated by the extracted drift coefficient forms an attractor which resembles the shape and the extent of the original deterministic attractor. Hence using our method, we obtain information about the deterministic properties of the process from stochastic data, although the dynamics of the process are significantly altered by the noise.

### C. Reconstruction of stochastic dynamics

In order to reconstruct a stochastic trajectory which possesses deterministic and random properties similar to those of the studied process, drift and diffusion coefficients must be estimated from the stochastic data set. A stochastic trajectory can be obtained from the Langevin equation as

$$X_i(t + \Delta t) = X_i(t) + D_i^{(1)}(\mathbf{X}(t))\Delta t + \sqrt{\Delta t} \sum_{j=1}^i g_{ij}(\mathbf{X}(t))\Gamma_j(t), \quad (12)$$

where  $\Gamma_j(t)$  represents uncorrelated noise,  $\langle \Gamma_i(t)\Gamma_j(t') \rangle$

$= Q\delta_{ij}\delta(t-t')$ , with vanishing mean,  $\langle \Gamma_i(t) \rangle = 0$ , for each  $i,j$ . Following Eq. (3b), the noise amplitudes  $g_{ij}$  can be calculated from

$$Q\mathbf{g}\mathbf{g}^\dagger = \mathbf{D}^{(2)} \quad (13)$$

using the Cholesky decomposition [8], p. 96, iff. (i)  $\mathbf{D}^{(2)}$  is positive definite and symmetric, and (ii)  $\mathbf{g}$  is a lower triangular matrix. Diffusion coefficient fulfills the condition (i), and we assume that  $\mathbf{g}$  is of a lower triangular form. The sum in Eq. (12) therefore includes only the first  $i$  terms.

For the van der Pol oscillator, the original and the reconstructed stochastic trajectories are shown in Fig. 9. As expected, the trajectories are not the same because the noise time series used to generate them are different. However, both stochastic trajectories are qualitatively similar and they possess the same deterministic and random properties.

For the Lorenz system, the original and the reconstructed stochastic trajectories are compared in Fig. 10. Again, both trajectories match qualitatively.

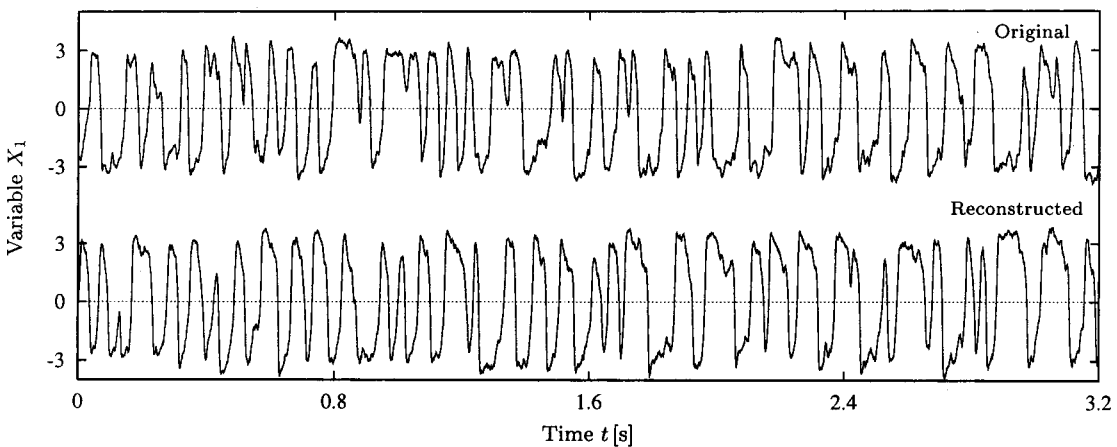


FIG. 9. Comparison of the original and reconstructed stochastic trajectories of the van der Pol oscillator.

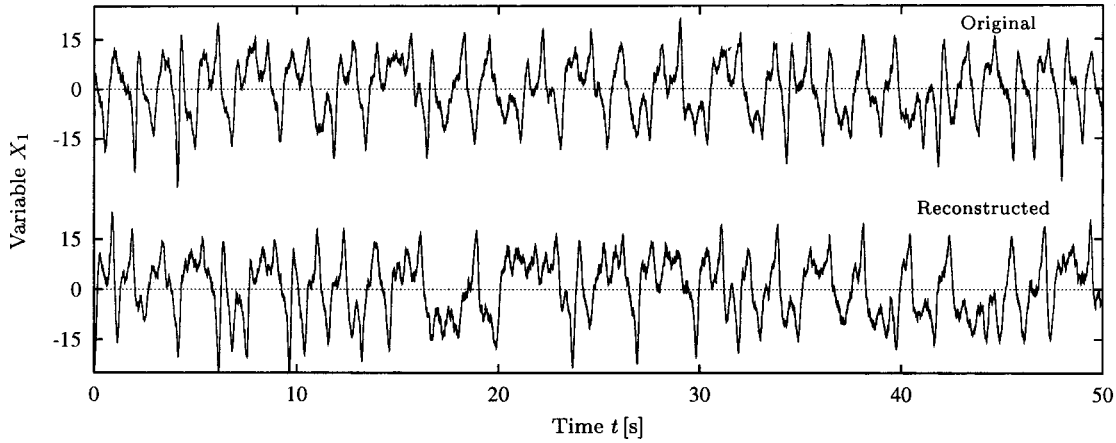


FIG. 10. Comparison of the original and reconstructed stochastic trajectories of the Lorenz system.

The possibility of generating a stochastic trajectory which resembles the deterministic as well as the random properties of the original trajectory can be applied effectively for various purposes. One of them is discussed below.

*Estimation of the mean first passage time.* The mean first passage time denotes the mean period between successive visits of the process trajectory to a selected location in phase space. Suppose that we had measured a trajectory in which only a few passages of interest were observed. To estimate reliably the mean first passage time, we would need many such passages. One solution to this problem which does not involve additional measurements is to extract drift and diffusion coefficients from the measured trajectory, and to reconstruct a stochastic trajectory which is sufficiently long to contain enough passages.

As an example, we again use a stochastic process which exhibits a pitchfork bifurcation [Eq. (A1)]. The time series generated by the process (Fig. 1) can be considered as a trace of a randomly disturbed particle in a one-dimensional two-well potential. Our goal is to estimate the mean time needed by the particle to pass from the well at  $x = -\sqrt{\epsilon}$  to the well at  $x = \sqrt{\epsilon}$ . Based on a time series containing only 3 passages, a stochastic trajectory was reconstructed containing 200 passages. In Fig. 11(a), the distribution of the estimated passage

times is compared to the distribution obtained from the original trajectory containing 200 passages. The overall shapes of both distributions agree quite well, although the curves differ in details. Still, the mean first passage times, marked by the vertical lines, are similar.

The passage times depend on the noise amplitude  $g$ . In the case of a particle in a two-well potential, the higher the noise amplitude, the shorter the mean passage time. The dependences of the mean first passage times on the noise amplitude obtained from the original and reconstructed trajectories are compared in Fig. 11(b). The agreement between the two dependences is very good.

#### IV. ANALYSIS OF EXPERIMENTAL DATA

In this section we apply the method to analyze experimental time series measured in different regimes of metal cutting [9]. The dynamics of metal cutting involve several nonlinear dynamic phenomena, such as material flow and fracture, friction between the tool and the workpiece, coupled vibrations of a machine–tool–workpiece assembly, etc. By varying the cutting parameters, dynamically different cutting regimes can be achieved. For example, if the cutting depth is increased over a certain critical value, self-excited large-

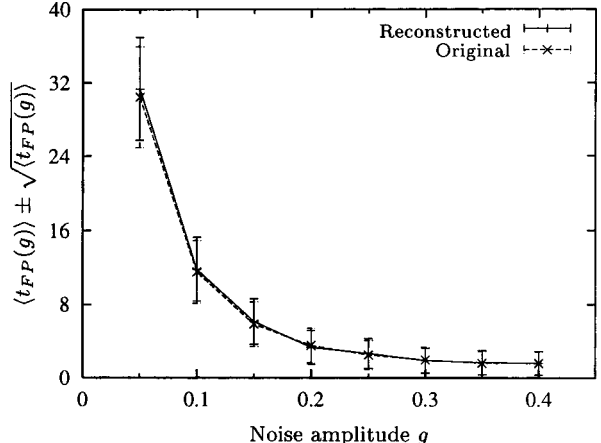
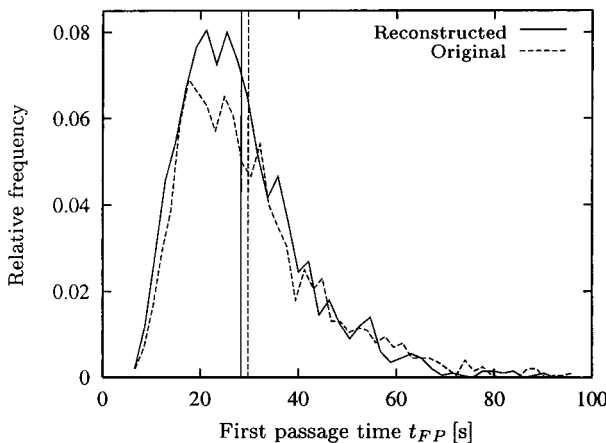


FIG. 11. (a) Comparison of distributions of first passage times from  $x = -\sqrt{\epsilon}$  to  $x = \sqrt{\epsilon}$  at noise amplitude of  $g = 0.05$  for the original and reconstructed trajectories. The vertical lines denote the mean values. (b) A comparison of dependences of the mean first passage times on the noise amplitude  $g$  for the original and the reconstructed trajectories.

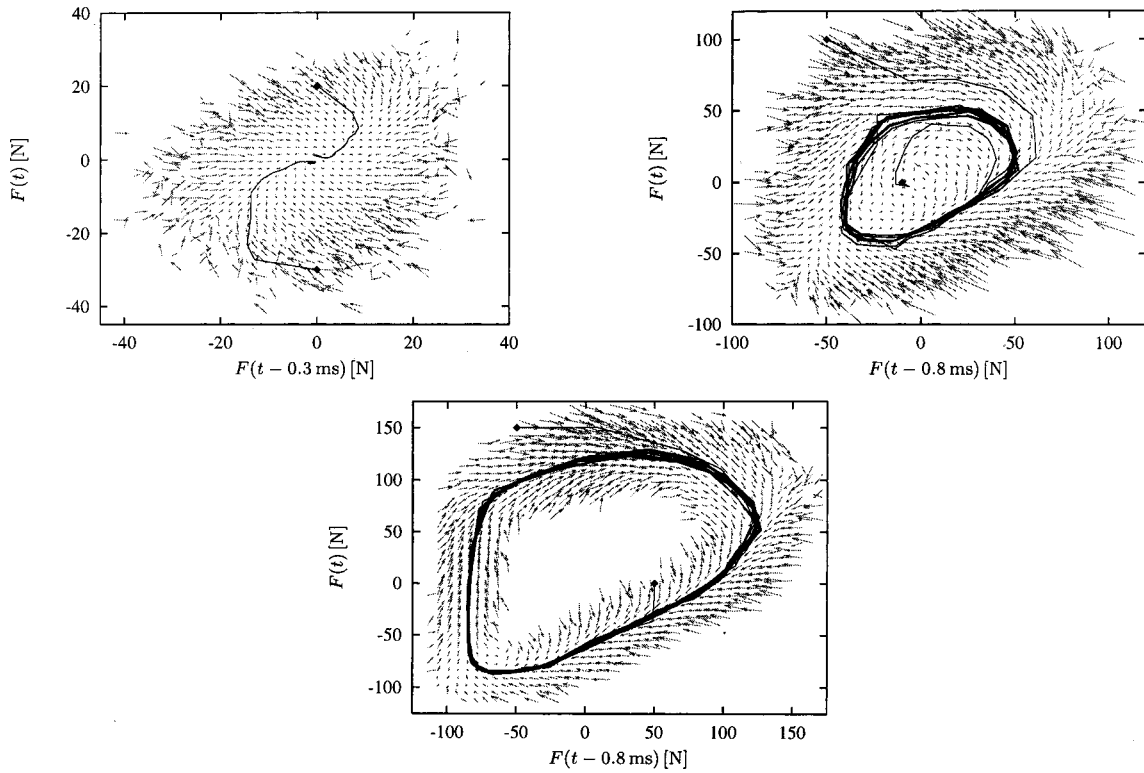


FIG. 12. Two-dimensional projections of drift coefficients for chatter-free (left), weak (right), and strong chatter regimes (bottom). The superimposed trajectories were integrated using the corresponding drift coefficients.

amplitude vibrations of the machine–tool–workpiece assembly may develop. Cutting accompanied by such vibrations is known as chatter. With its detrimental effect on the workpiece, tool, and machine, chatter has been studied intensively in recent decades. Analysis of simple nonlinear models of the cutting process has revealed that the onset of chatter can be described as a subcritical Hopf bifurcation [10,11,9]. Such a description of chatter onset has been confirmed by bifurcation diagrams obtained experimentally [12–14]. However, evidence for such a description based on analysis of measured time series has been lacking, presumably due to the stochastic nature of the process.

We chose turning on a lathe as an example of the cutting process, where a rotating workpiece is cut by a fixed tool. We analyzed the time series recorded during three cutting regimes denoted as (a) chatter-free cutting, (b) cutting accompanied by weak chatter, and (c) cutting accompanied by strong chatter. Drift coefficients (Fig. 12) were estimated in a three-dimensional phase space reconstructed from the scalar time series using the delay coordinates [15]. The trajectories, which are shown superimposed on the fields, were integrated according to Eq. (11). In the case of the chatter-free regime (the top left panel), the field arrows point towards the center of the phase space. This indicates the existence of a stable fixed point at (0,0,0). Both trajectories which start at the edge of the phase portrait end up close to the assumed stable fixed point. In chatter regimes, a stable nonsymmetric limit cycle is present. In the weak chatter regime (the top right panel), the field arrows inside the limit cycle point out towards the cycle, which indicates that an unstable fixed point might be located in the center of the phase space. This is also shown by the path of the trajectory starting in the center of the phase

space. The unstable fixed point cannot be observed in the case of strong chatter (bottom panel), because the process trajectory does not visit the center region of the phase space.

Closer examination of drift coefficients in the chatter regimes reveals interesting changes to the local dissipation in the phase space. The average inclination of the arrows towards the limit cycle is much greater in the lower right portion of the limit cycle than in the upper left portion. The two portions of the limit cycle correspond to the tool motion towards and away from the workpiece, respectively. Different average inclinations presumably result from the dependence of damping on the relative direction of the tool motion with respect to the workpiece.

To check the stability of the observed fixed point quantitatively, the drift coefficients were approximated using third order polynomials. Eigenvalues  $\lambda_i$  of the Jacobian matrix evaluated at the fixed point (0,0,0) are listed in Table I. The real part of the pair of the largest  $\lambda_i$  is negative in chatter-free cutting and positive in both chatter regimes. This confirms that the fixed point is stable during chatter-free cutting and unstable during chatter. Such dependence of the real part of  $\lambda_{1,2}$  is typical of the Hopf bifurcation from a stable fixed point to a stable limit cycle [16].

TABLE I. Stability coefficients of the fixed point (0,0,0), calculated from the equations which approximate  $\mathbf{D}^{(1)}$ .

Cutting regime	$\lambda_1$	$\lambda_2$	$\lambda_3$
Chatter-free	$-2.19 + i3.58$	$-2.19 - i3.58$	-2.95
Weak chatter	$0.11 + i1.57$	$0.11 - i1.57$	-7.62
Strong chatter	$0.48 + i1.86$	$0.48 - i1.86$	0

## V. DISCUSSION AND CONCLUSIONS

Dynamics noise often represents a serious obstacle to analysis of process dynamics. However, for stochastic processes that obey the Fokker–Planck equation, the laws of deterministic dynamics, and the form and strength of the fluctuations can be determined by estimating the drift and diffusion coefficients of the Fokker–Planck equation directly from a time series [3,4]. The estimates of the coefficients are independent of the time step applied for the estimation of the conditional probability distribution, provided that the time step is sufficiently short. Numerical study has revealed that drift coefficient estimates converge to a limit value at time steps one order of magnitude longer than estimates of diffusion coefficient. The time step, which is necessary for the estimates to converge, depends on the properties of the process. We found the necessary time step to be shorter than the time step required for the integration of the corresponding differential equations. When analyzing experimental data, the convergence of the estimates with decreasing time step should be established. Such a convergence test may also serve as a criterion for selection of an appropriate sampling time. A lack of convergence of the estimated coefficients with decreasing time step indicates non-Markovian properties of the process [7].

Since drift and diffusion coefficients correspond to the deterministic and random parts of the process dynamics, respectively, their separate estimation from data is equivalent to decomposition of the process dynamics into a deterministic and a random component. This decomposition served as a basis for the applications of stochastic data analysis presented in this paper. (a) The drift coefficient plotted as a vector field represents the deterministic dynamics of the process. Closer examination of the field can reveal additional information on the local stability properties of the process in the phase space. (b) Drift and diffusion coefficients can be employed to reconstruct the process dynamics governed by the Langevin equation. When only the drift coefficient is used to solve the truncated Langevin equation, a deterministic solution is obtained. This solution represents the trajectory of the process which would be observed in the absence of random fluctuations. Although remotely similar, such a deterministic solution should not be mistaken for filtering of dynamic noise, since the process would evolve differently under the same deterministic laws if the random fluctuations were present. (c) If both drift and diffusion coefficients are used for the integration of the Langevin equation, a representative stochastic trajectory of the process can be obtained. Stochastic trajectories can be applied as surrogate process trajectories, since they possess the same deterministic and random properties as the original process. (d) We have used the representative trajectories to estimate the mean first passage time in the case where the original trajectory contained only a few passages of interest.

Finally, experimental data sets acquired in three typical regimes of metal cutting were analyzed. Based on estimated drift coefficients, it was shown that cutting dynamics in the chatter-free regime could be described as random fluctuations around a stable fixed point, while in the two chatter regimes the fluctuations occur around a stable limit cycle. The drift coefficients were approximated by third order poly-

nomials, and the stability of the fixed point was assessed quantitatively. It was found that the transition from a chatter-free to a chatter regime corresponds to the Hopf bifurcation from a stable fixed point to a stable limit cycle. Such a description of the transition is in accordance with the analytical and qualitative experimental results.

Time series from metal cutting have often been analyzed using the methods of nonlinear time series analysis [17–21]. The dynamics of cutting with chatter were mostly described as low dimensional, while descriptions of chatter-free cutting dynamics ranged from linearly correlated random to low-dimensional chaotic. Such differences in descriptions can be attributed either to different experimental setups or to incautious use of the analysis methods. However, most researchers have reported a substantial level of noise in their data. Based on our experience [20], we suspect that different descriptions of the cutting dynamics might also have resulted due to dynamic noise in the measured time series. We have shown in this paper that dynamic noise can significantly broaden a limit cycle attractor or dramatically distort a chaotic attractor (see left panels of Figs. 6 and 7). Disregarding the effect of dynamic noise in these two cases, one might be led to search for a complicated structure in the noisy limit cycle attractor, and to overlook the underlying structure of the noisy chaotic attractor.

Only dynamic noise was considered in our study, while the influence of measurement noise has been neglected. However, by evaluating drift and diffusion coefficients the influence of measurement noise can be estimated for systems, where the dynamic noise level exceeds the measurement noise level [22].

In summary, we have proposed applications for analysis of time series from stochastic processes governed by a Langevin equation. Since the measured time series are very likely to be stochastic, the applications could complement other nonlinear time series analysis techniques, especially in the cases where dynamic noise in the process cannot be neglected.

## ACKNOWLEDGMENTS

The authors thank Tomáš Klinc for making them aware of the Cholesky decomposition [8, p. 96]. J.G. and I.G. gratefully acknowledge the support of the Volkswagen Foundation, EU COST Action P4, and the Ministry of Science and Technology of Slovenia.

## APPENDIX: SYNTHETIC DATA SETS

In the following, the uncorrelated noise  $\Gamma(t)$  is Gaussian distributed with zero mean and variance equal to one.

### 1. Pitchfork bifurcation

The dynamics of a stochastic process exhibiting the pitchfork bifurcation is governed by the following Langevin equation:

$$\dot{X}(t) = \epsilon X(t) - X(t)^3 + g\Gamma(t). \quad (\text{A1})$$

We chose  $\epsilon = 0.1$  and  $g = 0.05$ .

## 2. van der Pol oscillator

The dynamics of the stochastic van der Pol oscillator are governed by

$$\dot{X}_1 = X_2, \quad (\text{A2a})$$

$$\dot{X}_2 = (\epsilon - X_1^2)X_2 - X_1 + g\Gamma(t). \quad (\text{A2b})$$

We chose  $\epsilon=2$  and  $g=3$ .

## 3. Lorenz system

The stochastic Lorenz system is governed by the following system of equations:

$$\dot{X}_1 = \sigma(X_2 - X_1) + \sum_j g_{1j}\Gamma_j(t), \quad (\text{A3a})$$

$$\dot{X}_2 = X_1(r - X_3) - X_2 + \sum_j q_{2j}\Gamma_j(t), \quad (\text{A3b})$$

$$\dot{X}_3 = X_1X_2 - bX_3 + \sum_j g_{3j}\Gamma_j(t), \quad (\text{A3c})$$

where the parameters  $\sigma=10$ ,  $r=28$ , and  $b=8/3$  were chosen so as to assure chaotic regime of the deterministic process. The matrix  $\mathbf{g}$  was

$$\mathbf{g} = \begin{bmatrix} 4 & 5 & 3 \\ 5 & 5 & 6 \\ 3 & 6 & 10 \end{bmatrix}. \quad (\text{A4})$$

- [1] H. Haken, *Advanced Synergetics*, 3rd ed. (Springer-Verlag, Berlin, 1993).
- [2] H. Kantz and T. Schreiber, Nonlinear Time Series Analysis, Vol. 7 of *Cambridge Nonlinear Science Series* (Cambridge University Press, Cambridge, England, 1997).
- [3] R. Friedrich and J. Peinke, *Physica D* **102**, 147 (1997).
- [4] S. Siegert, R. Friedrich, and J. Peinke, *Phys. Lett. A* **243**, 275 (1998).
- [5] K. Itô, *Nagoya Math. J.* **1**, 35 (1950).
- [6] H. Risken, *The Fokker-Planck Equation* (Springer-Verlag, Berlin, 1989).
- [7] J. Gradišek, S. Siegert, R. Friedrich, and I. Grabec (in preparation).
- [8] W. H. Press, S. A. Teukolsky, W. T. Vetterling, and B. P. Flannery, *Numerical Recipes in C, The Art of Scientific Computing*, 2nd ed. (Cambridge University Press, Cambridge, England, 1994).
- [9] J. Gradišek, Ph.D. thesis Dr/227, Faculty of Mechanical Engineering, University of Ljubljana, Ljubljana, Slovenia, 1999 (unpublished) (in Slovene).
- [10] G. Stépán and T. Kalmár-Nagy, in Proceedings of the 16th ASME Biennial Conference on Mechanical Vibration and Noise, 1997 ASME Design and Technical Conferences, Sacramento, California, 1997, pp. 1–11.
- [11] A. H. Nayfeh, C.-M. Chin, and J. R. Pratt, *ASME J. Manuf. Sci. Eng.* **119**, 485 (1997).
- [12] C. J. Hooke and S. A. Tobias, in *Proceedings of the 4th International Machine Tools Design and Research Conference* (Pergamon, Manchester, 1963), pp. 97–109.
- [13] N. H. Hanna and S. A. Tobias, *ASME J. Eng. Ind.* **96**, 247 (1974).
- [14] J. R. Pratt, M. A. Davies, C. J. Evans, and M. D. Kennedy, *Ann. CIRP* **48**, 39 (1999).
- [15] N. H. Packard, J. P. Crutchfield, J. D. Farmer, and R. S. Shaw, *Phys. Rev. Lett.* **45**, 712 (1980).
- [16] S. H. Strogatz, *Nonlinear Dynamics and Chaos* (Addison-Wesley, Reading, PA, 1994).
- [17] E. Govekar and I. Grabec, in *Progress in Acoustic Emission* (The Japanese Society for NDI, 1994), Vol. VII, pp. 613–618.
- [18] S. T. S. Bukkapatnam, A. Lakhtakia, and S. R. T. Kumara, *Phys. Rev. E* **52**, 2375 (1995).
- [19] B. S. Berger, I. Minis, Y. H. Chen, A. Chavali, and M. Rokni, *J. Sound Vib.* **184**, 936 (1995).
- [20] J. Gradišek, E. Govekar, and I. Grabec, *Mech. Syst. Signal Process.* **12**, 839 (1998).
- [21] M. A. Johnson, Ph.D. thesis, Cornell University, Ithaca, New York, 1996 (unpublished).
- [22] J. Peinke (private communication).

# Analysis of data sets of stochastic systems

S. Siegert<sup>a,1</sup>, R. Friedrich<sup>a</sup>, J. Peinke<sup>b,2</sup>

<sup>a</sup> Institut für Theoretische Physik, Universität Stuttgart, 70550 Stuttgart, Germany

<sup>b</sup> Experimentalphysik II, Universität Bayreuth, 95447 Bayreuth, Germany

Received 26 March 1998; accepted for publication 6 April 1998

Communicated by J. Flouquet

---

## Abstract

This paper deals with the analysis of data sets of stochastic systems which can be described by a Langevin equation. By the method presented in this paper drift and diffusion terms of the corresponding Fokker–Planck equation can be extracted from the noisy data sets, and deterministic laws and fluctuating forces of the dynamics can be identified. The method is validated by the application to simulated one- and two-dimensional noisy data sets. © 1998 Published by Elsevier Science B.V.

PACS: 02.50.Fz; 02.50.Ey; 02.50.Ga

---

## 1. Introduction

In biological, economical, physical or technical systems noisy data sets occur very frequently. For describing and/or influencing these complex systems, it is necessary to know the deterministic laws and the strength of the fluctuations controlling the dynamics. Especially in the dynamics of order parameters close to instability points fluctuations play an important role [1–3]. This paper discusses a general method which allows one to determine drift and diffusion coefficients of the Fokker–Planck equation for stationary continuous complex systems with Markov properties. So a complete description of the stochastic process is found. This problem has also been addressed in Refs. [4,5], but in a different way.

## 2. Basic relations

### 2.1. Langevin equation and Markovian property

The dynamics of a continuous Markovian system is governed by a Langevin equation (1) for a set of  $n$  variables  $\{q_k(t)\}$ ,  $k = 1, \dots, n$  [6],

$$\begin{aligned} \frac{d}{dt} q_i(t) &= h_i(\{q_k(t)\}, t) \\ &+ \sum_j g_{ij}(\{q_k(t)\}, t) \Gamma_j(t), \quad k = 1, \dots, n. \end{aligned} \quad (1)$$

The fluctuating Langevin forces  $\Gamma_j(t)$  are considered to be  $\delta$ -correlated noise functions with vanishing mean as expressed as

$$\langle \Gamma_i(t) \rangle = 0 \quad \forall i, \quad (2)$$

$$\langle \Gamma_i(t) \Gamma_j(t') \rangle = Q \delta_{ij} \delta(t - t') \quad \forall i, j. \quad (3)$$

<sup>1</sup> E-mail: silke@theo3.physik.uni-stuttgart.de.

<sup>2</sup> E-mail: joachim.peinke@uni-bayreuth.de.

The condition of the Markovian property demands that the dynamics of the process depends only on the present state of the system and not on its history. With definition (4) for conditional probability density distributions  $p$ , the condition for the validity of the Markovian property can be expressed by Eq. (5) [7,8],

$$\begin{aligned} p(q_n, t_n | q_{n-1}, t_{n-1}; \dots; q_1, t_1) \\ \equiv \frac{w(q_n, t_n; \dots; q_1, t_1)}{w(q_{n-1}, t_{n-1}; \dots; q_1, t_1)}. \end{aligned} \quad (4)$$

$\int w(q_n, t_n; \dots; q_1, t_1) \prod_i dq_i$  is the probability to find the system in  $q_i \dots q_i + dq_i$  at time  $t_i$  for all  $i$ ,

$$\begin{aligned} p(q_n, t_n | q_{n-1}, t_{n-1}; \dots; q_1, t_1) \\ = p(q_n, t_n | q_{n-1}, t_{n-1}), \quad t_n > t_{n-1} > \dots > t_1, \end{aligned} \quad (5)$$

where  $t_{n-1}$  is the next earlier time before  $t_n$ .

This condition can be validated by analysing the data sets numerically, as has been shown in Ref. [9]. In case that the Markovian property does not fit, the dimension of the state vector can be increased by including a further observable. This can always be achieved by introducing delay coordinates. Thus by introducing new random variables, non-Markovian processes may be reduced to Markovian systems [8].

## 2.2. Fokker–Planck equation

Usually a formal general solution of the stochastic differential Langevin equation (1) cannot be given. Therefore a Fokker–Planck equation (6) is set up by which the probability density distribution  $w(\{q_k(t), t\})$  of the stochastic variables can be calculated [10],

$$\begin{aligned} \frac{\partial}{\partial t} w(\{q_k(t), t\}) \\ = - \sum_{i=1}^n \frac{\partial}{\partial q_i} (D_i^{(1)}(\{q_k(t)\}, t) w(\{q_k(t)\}, t)) \\ + \frac{1}{2} \sum_{ij=1}^n \frac{\partial^2}{\partial q_i \partial q_j} (D_{ij}^{(2)}(\{q_k(t)\}, t) w(\{q_k(t)\}, t)), \\ k = 1, \dots, n. \end{aligned} \quad (6)$$

The coefficients  $D_i^{(1)}$  are called drift coefficients, the terms  $D_{ij}^{(2)}$  diffusion coefficients. They are defined as [8]

$$\begin{aligned} D_i^{(1)}(\{q_k(t)\}, t) &= \lim_{\tau \rightarrow 0} \frac{1}{\tau} \langle \tilde{q}_i(t + \tau) - q_i \rangle|_{\{\tilde{q}_k(t)\}=\{q_k\}} \\ &= \lim_{\tau \rightarrow 0} \frac{1}{\tau} \int_{-\infty}^{+\infty} (\tilde{q}_i(t + \tau) - q_i) \\ &\quad \times p(\{\tilde{q}_k\}, t + \tau | \{q_k\}, t) \prod_k d\tilde{q}_k, \end{aligned} \quad (7)$$

$$\begin{aligned} D_{ij}^{(2)}(\{q_k(t)\}, t) &= \lim_{\tau \rightarrow 0} \frac{1}{\tau} \langle (\tilde{q}_i(t + \tau) - q_i)(\tilde{q}_j(t + \tau) - q_j) \rangle|_{\{\tilde{q}_k(t)\}=\{q_k\}} \\ &= \lim_{\tau \rightarrow 0} \frac{1}{\tau} \int_{-\infty}^{+\infty} (\tilde{q}_i(t + \tau) - q_i)(\tilde{q}_j(t + \tau) - q_j) \\ &\quad \times p(\{\tilde{q}_k\}, t + \tau | \{q_k\}, t) \prod_k d\tilde{q}_k, \quad k = 1, \dots, n, \end{aligned} \quad (8)$$

where  $\{\tilde{q}_k(t + \tau)\}$  with  $\tau > 0$  is a solution of (1) which at time  $t$  has the sharp value  $\{\tilde{q}_k(t)\} = \{q_k\}$ .

In Ref. [11] an application of Eqs. (7) and (8) together with the definitions of conditional probability density distributions (4) to the statistical properties of a turbulent cascade is discussed.

The relations between the sets of coefficients of the Langevin equation and the Fokker–Planck equation in consideration of the Stratonovich definitions are [8]

$$\begin{aligned} D_i^{(1)}(\{q_k(t)\}, t) &= h_i(\{q_k(t)\}, t) \\ &+ \frac{Q}{2} \sum_{l,j} g_{lj}(\{q_k(t)\}, t) \frac{\partial}{\partial q_l} g_{jl}(\{q_k(t)\}, t), \end{aligned} \quad (9)$$

$$\begin{aligned} D_{ij}^{(2)}(\{q_k(t)\}, t) \\ = Q \sum_l g_{il}(\{q_k(t)\}, t) g_{jl}(\{q_k(t)\}, t), \\ k = 1, \dots, n. \end{aligned} \quad (10)$$

## 3. Analysis of stochastic data sets

A continuous Markovian system in the presence of white noise is governed by a Langevin equation (1) and by the corresponding Fokker–Planck

equation (6). A complete analysis of such a complex system, therefore, should yield the quantities  $h_i$  and  $g_{ij}$  of the Langevin equation (1) and the drift and diffusion coefficients  $D_i^{(1)}$  and  $D_{ij}^{(2)}$  of the Fokker-Planck equation (6). According to (9) and (10), both sets of terms are correlated with each other.

For the class of stationary continuous Markovian systems with white dynamical noise under consideration, where the validity of the Markovian property may have been achieved by the introduction of delay coordinates, it is always possible to determine drift and diffusion terms directly from the data sets by using Eqs. (4), (7) and (8). Because of stationarity,  $D_i^{(1)}$  and  $D_{ij}^{(2)}$  have no explicit time dependence. The needed conditional probability density distribution can be determined numerically from the data set according to (4) by calculating histograms.

This general algorithm has apparently not been recognized in the literature up to now. The numerical method is completely general; no ansatz for the coefficients is needed. If analytical formulas for the evolution equations of a process are needed, the numerical results obtained may be approximated by analytical functions.

#### 4. Applications of the presented algorithm

In the following the algorithm will be applied to various one- and two-dimensional synthetically determined data sets.

##### 4.1. First example

The first example deals with the case of one-dimensional systems, following the Langevin equation

$$\dot{q}(t) = \epsilon q(t) - q(t)^3 + \Gamma(t), \quad (11)$$

which is valid for systems exhibiting noisy pitchfork bifurcations. Fig. 1 presents a part of the calculated noisy time series.

Fig. 2 shows drift and diffusion terms for this time series, calculated by determining the conditional probability density distribution for the variable  $q$  and using Eqs. (7) and (8).

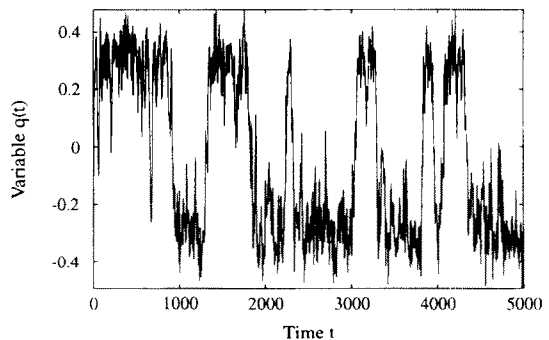


Fig. 1. Variable  $q$  versus time  $t$ . The time series is calculated according to the Langevin equation  $\dot{q}(t) = 0.1q(t) - q^3(t) + 0.05F(t)$ , where  $F(t)$  is a Gaussian distributed fluctuation force.

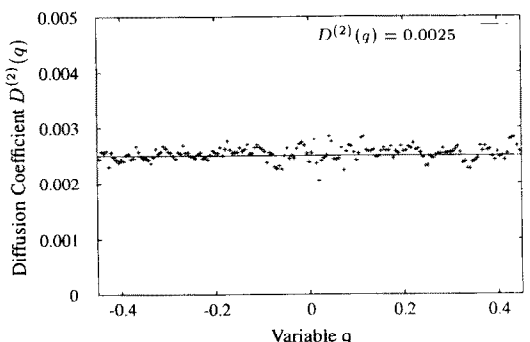
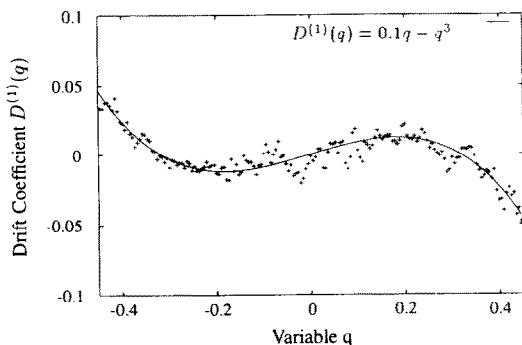
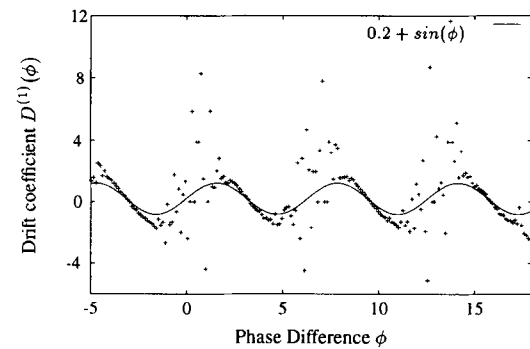
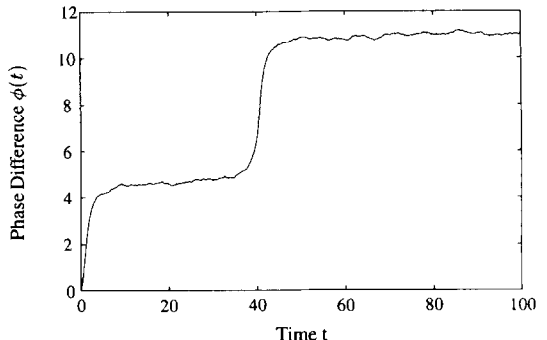
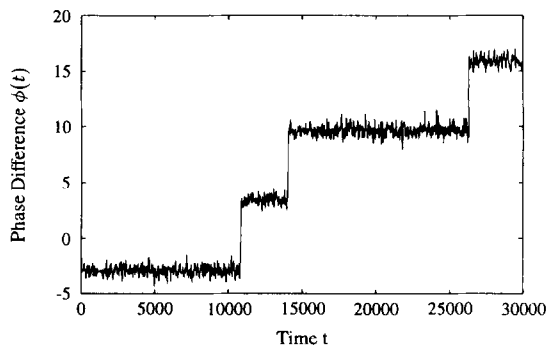


Fig. 2. Drift and diffusion coefficient  $D^{(1)}$  and  $D^{(2)}$  versus variable  $q$ . According to the algorithm discussed, the conditional probability distribution of the noisy time series shown in Fig. 1 has been determined and drift and diffusion terms have been calculated. The dots exhibit the numerically determined values, the solid line shows the theoretical functions for the coefficients according to Eqs. (9) and (10).



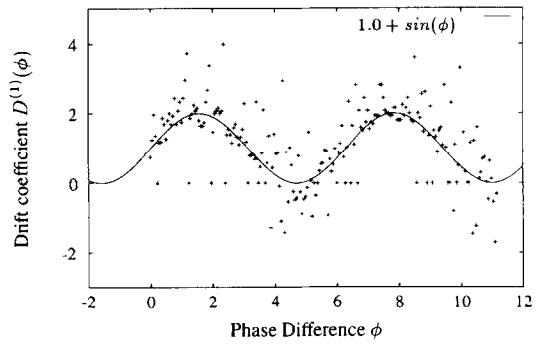
#### 4.2. Second example

The second example is concerned with one-dimensional systems following the Langevin equation,

$$\dot{\phi} = \omega + \sin(\phi) + \Gamma(t). \quad (12)$$

This type of equation describes the dynamics of a phase difference  $\phi = \phi_1 - \phi_2$ , where  $\phi_1, \phi_2$  are the phases of two coupled nonlinear oscillators. For two different sets of parameters the noisy time series and calculated drift coefficients are shown in Figs. 3 and 4. Because of the singularities of the time series there is only a small probability for the corresponding variable values. These rapid changes of the phase are responsible for the strong noise of the drift coefficient.

Since the Langevin equation (12) is valid for a wide class of biological systems applications of the algorithm for many different fields are expected.



#### 4.3. Third example

After these two examples of one-dimensional systems the case of two variables will be discussed. In the following examples the method presented will be applied on vectors with two components. The third example is based on the differential equation system of a Hopf bifurcation:

$$\frac{d}{dt}q_1 = \epsilon q_1 - \gamma q_2 + (q_1^2 + q_2^2)(\mu q_1 - \omega q_2), \quad (13)$$

$$\frac{d}{dt}q_2 = \gamma q_1 - \epsilon q_2 + (q_1^2 + q_2^2)(\omega q_1 + \mu q_2). \quad (14)$$

Fig. 5 shows the phase diagram of the  $q_1$  and  $q_2$ . The parameters

$$\epsilon = 0.05, \quad \gamma = 1, \quad \mu = -5, \quad \omega = 7.5 \quad (15)$$

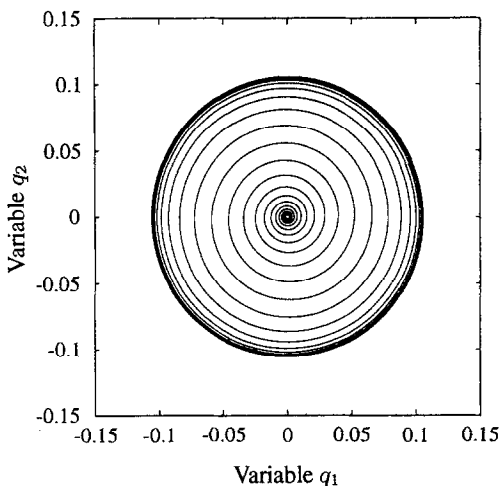


Fig. 5. Variable  $q_2$  versus variable  $q_1$ . The phase diagram shows the dynamics of a Hopf bifurcation:  $\dot{q}_1 = 0.05q_1 - q_2 + (q_1^2 + q_2^2)(-5q_1 - 7.5q_2)$ ,  $\dot{q}_2 = q_1 - 0.05q_2 + (q_1^2 + q_2^2) \times (7.5q_1 - 5q_2)$ .

are chosen in such a way that the behaviour of the variables becomes supercritical, i.e. the focus  $(0,0)$  is unstable and the trajectory moves towards a stable limit cycle [12]. This system of differential equations is very important for describing time-spatial signals whose dynamics are determined by two order parameters.

Gaussian distributed white noise weighted by a factor 0.2 has been added to the system described by Eqs. (13) and (14). Afterwards the method presented has been applied. Fig. 6 shows the two numerically determined drift coefficients  $D_{q_1}^{(1)}(\mathbf{q})$  and  $D_{q_2}^{(1)}(\mathbf{q})$ . The hatched surface belongs to the calculated terms, the dashed one to the expected surface. The differences at the borders are caused by too few variable values in these regions. These values are taken only from a few stochastic realizations, so that the algorithm cannot work with great accuracy. In the main field a good conformance between calculated and expected surfaces can be seen.

#### 4.4. Fourth example

The fourth example deals with the case of a codimension II system. The dynamics of such a system is determined by the differential equations

$$\frac{d}{dt}q_1 = q_2 + F_1(t), \quad (16)$$

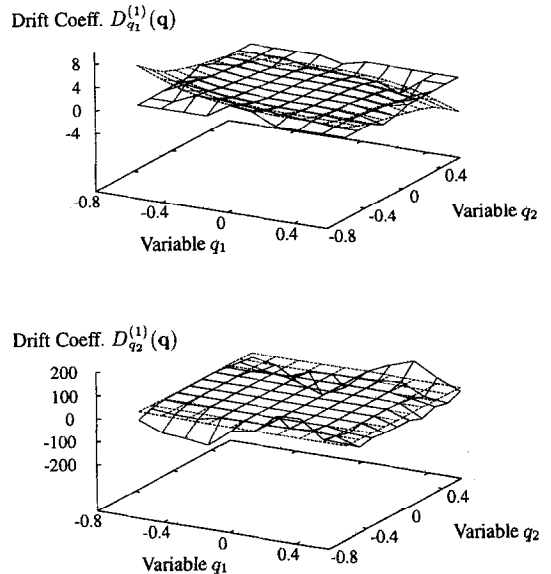


Fig. 6. Drift coefficients  $D_{q_1}^{(1)}$  and  $D_{q_2}^{(1)}$  versus variables  $q_1$  and  $q_2$ . The hatched surfaces belong to the calculated data, the dashed surfaces are plotted according to the expected surfaces:  $D_{q_1}^{(1)}(\mathbf{q}) = 0.05q_1 - q_2 + (q_1^2 + q_2^2)(-5q_1 - 7.5q_2)$ ,  $D_{q_2}^{(1)}(\mathbf{q}) = q_1 - 0.05q_2 + (q_1^2 + q_2^2)(7.5q_1 - 5q_2)$ .

$$\frac{d}{dt}q_2 = \epsilon q_1 + \gamma q_2 + \mu q_1^3 + \omega q_1^2 q_2 + F_2(t). \quad (17)$$

The parameters have been chosen as

$$\epsilon = 0.01, \quad \gamma = 0.03, \quad \mu = -1, \quad \omega = -1. \quad (18)$$

The fluctuation force  $F(t)$  has been taken as a Gaussian distributed noise weighted by a factor 0.05.

Fig. 7 shows the phase diagram for this system without a fluctuating force  $F(t)$ . The trajectory is repelled from the unstable focus and moves towards a limit cycle.

Fig. 8 illustrates the drift terms  $D_{q_1}^{(1)}(\mathbf{q})$  and  $D_{q_2}^{(1)}(\mathbf{q})$ , calculated by the method presented, together with the expected terms for the noisy system (16)–(18). In Fig. 9 one of the calculated diffusion coefficients,  $D_{q_1 q_2}^{(2)}(\mathbf{q})$ , and its theoretical function is shown.

#### 4.5. Summary and outlook

By the discussed method noisy data sets that obey a Fokker–Planck equation can be analysed and described. By a numerical determination of the conditional probability distributions drift and diffusion coef-

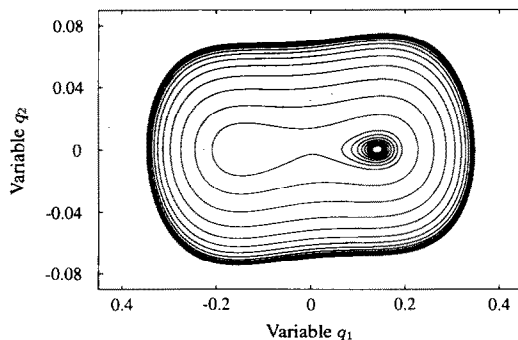


Fig. 7. Variable  $q_2$  versus variable  $q_1$ . The phase diagram shows the dynamics of a co-dimension II instability:  $\dot{q}_1 = q_2$ ,  $\dot{q}_2 = 0.02q_1 + 0.03q_2 - q_1^3 - q_1^2q_2$ .

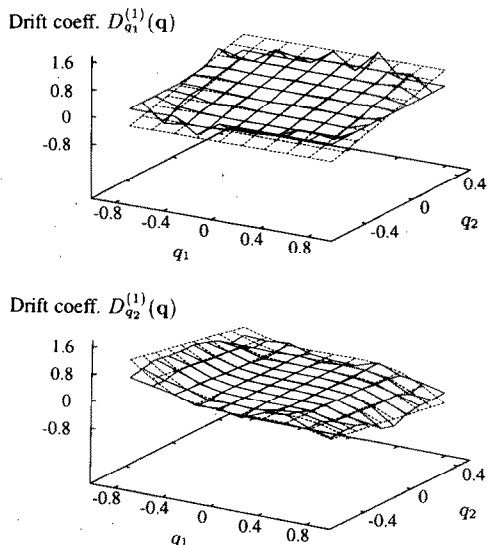


Fig. 8. Drift coefficients  $D_{q_1}^{(1)}(q)$  and  $D_{q_2}^{(1)}(q)$  versus variables  $q_1$  and  $q_2$ : The hatched surfaces belong to the calculated data, the dashed surfaces are drawn according to the expected surfaces:  $D_{q_1}^{(1)}(q) = q_2$ ,  $D_{q_2}^{(1)}(q) = 0.02q_1 + 0.03q_2 - q_1^3 - q_1^2q_2$ .

ficients can be calculated. Consequently the deterministic laws and the weight of the fluctuating forces underlying the dynamics of the system can be extracted.

The algorithm has been illustrated on various one- and two-dimensional systems, whose noisy time series have been simulated and afterwards analysed. A good conformance between determined and expected drift and diffusion coefficients can be seen.

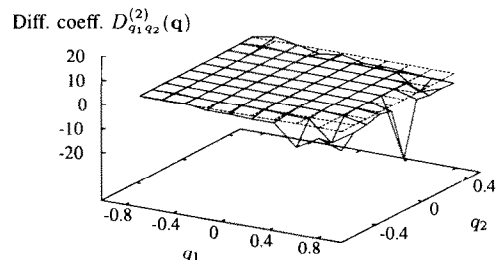


Fig. 9. Diffusion coefficient  $D_{q_1q_2}^{(2)}$  versus variables  $q_1$  and  $q_2$ . As a representative for the diffusion coefficients,  $D_{q_1q_2}^{(2)}$  has been calculated and drawn as a hatched surface. The dashed surface belongs to the expected diffusion coefficient  $D_{q_1q_2}^{(2)} = 0.0025$ .

In biological, physical, technical and economical systems noisy data sets referring to a Fokker–Planck equation occur very frequently. The presented method offers the possibility of analysing these systems and describing them in a mathematical way without the need of any form of ansatz or assumption. Therefore, there seems to be a broad field of a possible use of this algorithm.

## References

- [1] H. Haken, Synergetik (Springer, Berlin, 1990).
- [2] H. Haken, Advanced Synergetics (Springer, Berlin, 1983).
- [3] H. Haken, Information and Self-Organization (Springer, Berlin, 1988).
- [4] L.M. Borland, Ein Verfahren zur Bestimmung der Dynamik stochastischer Prozesse, Ph.D. thesis, Institut für Theoretische Physik und Synergetik der Universität Stuttgart (1993).
- [5] Y.L. Klimontovich, Int. J. Bif. and Chaos 3 (1993) 119.
- [6] N.G. van Kampen, Stochastic Processes in Physics and Chemistry (North-Holland, Amsterdam, 1981).
- [7] J. Honerkamp, Stochastische Dynamische Systeme (VCH Verlagsgesellschaft, Weinheim, 1990).
- [8] H. Risken, The Fokker–Planck Equation (Springer, Berlin, 1989).
- [9] R. Friedrich, J. Zeller, J. Peinke, Europhys. Lett. 41 (1998) 153.
- [10] Z. Schuss, Theory and Applications of Stochastic Differential Equations (Wiley, New York, 1980).
- [11] R. Friedrich, J. Peinke, Physica D 102 (1997) 147.
- [12] C. Uhl, Analyse raumzeitlicher Daten strukturbildender Systeme, Ph.D. thesis, Universität Stuttgart (1995).